

INTERACTIONS BETWEEN ELECTROMAGNETIC
ION CYCLOTRON WAVES AND PROTONS IN
THE MAGNETOSPHERE: SCATHA RESULTS

Except where reference is made to the work of others, the work described in this dissertation is my own or was done in collaboration with my advisory committee.
This dissertation does not include proprietary or classified information.

Son Thanh Nguyen

Certificate of Approval:

Yu Lin
Professor
Physics

J. D. Perez, Chair
Professor
Physics

Michael Pindzola
Professor
Physics

Edward Thomas, Jr.
Associate Professor
Physics

Allen Landers
Assistant Professor
Physics

George T. Flowers
Interim Dean
Graduate School

INTERACTIONS BETWEEN ELECTROMAGNETIC
ION CYCLOTRON WAVES AND PROTONS IN
THE MAGNETOSPHERE: SCATHA RESULTS

Son Thanh Nguyen

A Dissertation

Submitted to

the Graduate Faculty of

Auburn University

in Partial Fulfillment of the

Requirements for the

Degree of

Doctor of Philosophy

Auburn, Alabama

May 10, 2007

INTERACTIONS BETWEEN ELECTROMAGNETIC
ION CYCLOTRON WAVES AND PROTONS IN
THE MAGNETOSPHERE: SCATHA RESULTS

Son Thanh Nguyen

Permission is granted to Auburn University to make copies of this dissertation at its discretion, upon request of individuals or institutions and at their expense. The author reserves all publication rights.

Signature of Author

Date of Graduation

VITA

Son Thanh Nguyen, son of Bay Minh Nguyen and Nam Thi Pham, was born on January 25, 1956, in Tien Giang Province, Vietnam. He graduated from Auburn University with a Master of Science degree in Physics in August 2005. He also earned a Master of Science degree in Physics from the University of Newcastle, Australia in August 1998 and a Bachelor of Science degree in Physics from the Hochiminh National University, Vietnam in August 1979. He worked as a Physics lecturer at the Pre-University School in Hochiminh City, Vietnam from 1980 to 1995, and then went to the University of Newcastle, Australia to study. After graduating he was back to Vietnam and continued to work at the Pre-University School until July 2002. He joined the Department of Physics, Auburn University in August 2002 to pursue a degree of Doctor of Philosophy.

DISSERTATION ABSTRACT
INTERACTIONS BETWEEN ELECTROMAGNETIC
ION CYCLOTRON WAVES AND PROTONS IN
THE MAGNETOSPHERE: SCATHA RESULTS

Son Thanh Nguyen

Doctor of Philosophy, May 10, 2007
(M.S., Auburn University, 2005)
(M.S., The University of Newcastle, 1997)
(B.S., The Hochiminh National University, 1979)

168 Typed Pages

Directed by Joe D. Perez

Electromagnetic ion cyclotron (EMIC) waves and their role in governing proton populations in the ring current and radiation belt regions are of importance in understanding the dynamics of the Earth's magnetosphere. The availability of SCATHA magnetic field and proton spectra data allowed us to study the electromagnetic proton cyclotron instability as a generation mechanism for EMIC waves and the relationship between EMIC waves and protons in the equatorial region of the magnetosphere. To identify EMIC waves and obtain wave power spectra from the SCATHA magnetic field data, we employed the fast Fourier transform and spectral analysis techniques.

First, we studied the conditions under which the electromagnetic proton cyclotron instability acts as a generation mechanism for EMIC waves in the Earth's magnetosphere. The results are consistent with those of previous studies and/or with theoretical expectations. Especially, the results show an inverse correlation between proton temperature anisotropy and proton parallel beta, that the observed proton temperature anisotropies are above the electromagnetic proton cyclotron instability thresholds, and that the observed waves actually get energy from energetic and anisotropic proton populations.

Second, we studied the relationship between EMIC waves and protons in the region, and found that there were 20 short time intervals showing correlations between EMIC waves and proton perpendicular differential fluxes. They indicate that under suitable conditions, i.e., the proton distributions are non-gyrotropic or exhibit gyrophase bunching, EMIC waves indeed pitch angle scatter protons either toward or away from the local magnetic field. To explain the observations, we also established a model that is based on resonant interactions between EMIC waves and protons. In this model individual protons interact resonantly with the whole or a portion of the spectrum of the existing EMIC waves and are then pitch angle scattered with respect to the local ambient magnetic field. Calculations based on this model are in agreement with the observations and suggest that the EMIC waves are responsible for the changes in the proton distribution by pitch angle scattering protons with respect to the local ambient magnetic field.

ACKNOWLEDGEMENTS

The author would like to acknowledge the advice, guidance, continued support, and encouragement received from his advisor, Dr. J. D. Perez. Without his, this dissertation would have not been possible. He wishes to express his gratitude to Dr. Y. Lin, Dr. M. Pindzola, Dr. Ed. Thomas, and Dr. A. Landers for their servings as advisory committee members. His sincere appreciations go to all professors in the Department of Physics, Auburn University, who taught him during his time at Auburn University, and to Dr. An-Ban Chen for his help and encouragement. Thanks are also due to Dr. Joseph F. Fennell, Space Science Laboratory, the Aerospace Corporation for providing him with SCATHA data, to Dr. X. Y. Wang, the Department of Physics, Auburn University, and Dr. T. M. Loto'aniu, the Department of Physics, University of Alberta for their help in IDL programming, and to others in the Department of Physics, Auburn University, for their help in one way or another.

Finally, he wishes to thank his wife Na T. Tran, his children, his parents, his brothers and sister for their encouragement throughout his study in America.

Style manual or journal used AGU Style

Computer software used Microsoft Word 2003

TABLE OF CONTENTS

LIST OF TABLES	xiii
LIST OF FIGURES	xiv
1. INTRODUCTION	1
1.1 The Earth's magnetosphere	1
1.2 Proton populations in the magnetosphere	4
1.3 EMIC waves in the equatorial region of the magnetosphere	10
1.4 Interactions between EMIC waves and protons	16
1.5 Outline of the current dissertation	19
2. INSTRUMENTATION AND SPECTRAL ANALYSIS TECHNIQUES	21
2.1 Introduction	21
2.2 The SCATHA satellite	21
2.3 Spectral analysis techniques	26
2.3.1 Fast Fourier transform	26
2.3.2 Spectral analysis	28
2.3.2.1 Auto-power	29
2.3.2.2 Cross-power	29
2.3.2.3 Problems associated with the fast Fourier transform	30
2.3.3 Polarization analysis	33

2.3.4	Frequency-time analysis (dynamic analysis)	40
2.4	SCATHA data processing procedures	41
2.4.1	Introduction	41
2.4.2	Data processing procedures	42
2.5	Summary	46
3.	ELECTROMAGNETIC PROTON CYCLOTRON INSTABILITY AS A GENERATION MECHANISM FOR EMIC WAVES IN THE EARTH'S MAGNETOSPHERE	47
3.1	Introduction	47
3.2	Data preparation and event selection	48
3.3	Methodology	50
3.3.1	Electromagnetic proton cyclotron instability	50
3.3.2	Estimation of proton temperature anisotropy	51
3.3.3	Estimation of proton parallel temperature	54
3.4	Example	55
3.5	Results and discussions	59
3.5.1	Inverse relation between proton temperature anisotropy and proton parallel beta	59
3.5.2	Dependence of proton temperature anisotropy on proton perpendicular temperature	67
3.5.3	Dependence of proton perpendicular temperature on wave normalized frequency	71
3.6	Conclusions	74

4. OBSERVATIONS OF PROTON SCATTERINGS BY EMIC WAVES IN THE MAGNETOSPHERE	76
4.1 Introduction	76
4.2 Data preparation	76
4.3 Observational results	77
4.4 Examples	82
4.4.1 Scattering of protons away from the local magnetic field	82
4.4.2 Scattering of protons toward the local magnetic field	89
4.4.3 Scattering of protons toward and away from the local magnetic field	93
4.5 Summary	98
5. A THEORETICAL MODEL OF SCATTERING OF PROTONS BY EMIC WAVES	99
5.1 Introduction	99
5.2 Cyclotron resonance between EMIC wave and proton	99
5.3 Theoretical model of scattering of protons by EMIC waves	100
5.4 Pitch angle scattering of protons by EMIC waves	105
5.5 Explanations for examples in Chapter 4	108
5.5.1 Explanations for scattering of protons away from the local magnetic field	108
5.5.2 Explanations for scattering of protons toward the local magnetic field	114

5.5.3 Explanations for scattering of protons toward and away from the local magnetic field	117
5.5.3.1 Scattering toward the local magnetic field in the energy bands centered at 36, 71, and 133 keV	117
5.5.3.2 Scattering away from the local magnetic field in the energy band centered at 15.6 keV	118
5.6 Discussions	122
5.7 Conclusions	125
6. SUMMARY AND CONCLUSIONS	127
REFERENCES	127
APPENDIX	145

LIST OF TABLES

<p>3.1 Summary of the relationship between A_p and $\beta_{\parallel p}$ through the coefficients S_p and α of the relation $A_p = S_p \beta_{\parallel p}^\alpha$ and the correlation coefficients R for different MLT sectors</p>	64
<p>3.2 Summary of the relationship between A_p and $\beta_{\parallel p}$ through the coefficients S_p and α of the relation $A_p = S_p \beta_{\parallel p}^\alpha$ and the correlation coefficients R for different L ranges</p>	64
<p>3.3 Summary of the relationship between A_p and T_\perp through the coefficients a and b of the relation $A_p = a T_\perp^b$ and the correlation coefficients R for different MLT sectors</p>	69
<p>3.4 Summary of the relationship between A_p and T_\perp through the coefficients a and b of the relation $A_p = a T_\perp^b$ and the correlation coefficients R for different L ranges</p>	69
<p>4.1 List of 20 time intervals during which correlations between EMIC waves and proton perpendicular differential fluxes were observed</p>	81

LIST OF FIGURES

1.1	Three-dimensional view of the Earth's magnetosphere	2
2.1	The SCATHA satellite and its instruments	23
2.2	The block diagram of the SCATHA magnetic data processing	45
3.1	From top to bottom, the first panel shows the plots of wave percent polarization versus frequency in the FAC (solid pink line) and GSM (dashed brown line) coordinate systems for the 2-minute interval beginning at 23:24 UT, day 048; the second shows those of ellipticity. The third shows the wave spectra for the same event; the solid pink line is P_{tran} in FAC; the dot-dashed black line is P_{para} in FAC; and the dashed brown line is P_{tran} in GSM. The fourth shows the plots of the calculated convective growth rate S (dashed brown line) and P_{tran} in FAC (solid pink line) versus frequency for the same event	58
3.2	The upper panel shows a scatter plot of proton temperature anisotropy versus proton parallel beta with the data binned by MLT values and color-coded; the four dotted lines are the fitting curves for four different MLT sectors. The lower panel shows the same plot as the upper panel, but the data are binned by L values; the three dotted lines are the fitting curves for three different L ranges	65
3.3	A scatter plot of proton temperature anisotropy versus proton parallel beta with the data binned by maximum normalized temporal growth rate values, γ_m/Ω_p ,	

and color-coded. The long-dashed blue line depicts the relation given by *Gary et al.* [1994a] for $\gamma_m/\Omega_p=10^{-4}$; the short-dashed red line depicts that for $\gamma_m/\Omega_p=10^{-3}$; and the dot-dashed green line for $\gamma_m/\Omega_p=10^{-2}$ 66

3.4 The upper panel shows a scatter plot of proton temperature anisotropy versus proton perpendicular temperature with the data binned by MLT values and color-coded; the four dotted lines are the fitting curves for four different MLT sectors. The lower panel shows the same scatter plot as the upper panel, but the data are binned by L values; the three dotted lines are the fitting curves for three different L ranges70

3.5 The upper panel shows a scatter plot of proton perpendicular temperature versus wave peak normalized frequency with the data binned by MLT values and color-coded. The lower panel shows the same scatter plot as the upper panel, but the data are binned by L values73

4.1 The first, second, third, and fourth panels from the top show the plots of j_{perp} (solid black lines) and j_{para} (dashed red lines), centered at 133.0, 71.0, 36.0, and 15.6 keV, versus universal time for two hours beginning at 13:00 UT, day 045; the fifth panel shows the plot of magnetic field strength versus UT; the sixth and the seventh show the dynamic displays of wave ellipticity and transverse power for the same time interval. The white solid line on the seventh panel indicates the local He^+ gyrofrequency86

4.2 From top to bottom, the first, second, and third panels show the plots of wave percent polarization, ellipticity, and powers versus frequency for 2-minute interval beginning at 14:35 UT, day 045; the fourth shows the plot of wave

magnetic amplitude versus frequency for the same event	87
4.3 The upper and lower panels show the plots of the observed j_{perp} and j_{para} versus proton energy for one-minute interval at three different instants. The dashed lines are the plots at the event occurrence instant (14:37 UT, day 045); the dotted lines are those at 14:31 UT, six minutes before the event occurs; and the dot-dashed lines are those at 14:43 UT, six minutes after the event	88
4.4 From top to bottom, the first, second, and third panels show the plots of j_{perp} (solid black lines) and j_{para} (dashed red lines), centered at 133, 71, and 36 keV, versus UT for 2 hours beginning at 06:00 UT, day 073; the fourth shows the plot of B_0 versus UT; the fifth and the sixth show the dynamic displays of wave ellipticity and transverse power for the same time interval	91
4.5 The same format as Figure 4.2 for 2-minute interval from 07:32 UT, day 073	92
4.6 The same format as Figure 4.1 for two hours beginning at 11:00 UT, day 051	95
4.7 The same format as Figure 4.2 for 2-minute interval from 12:23 UT, day 051	96
4.8 The upper and lower panels show the plots of the observed j_{perp} and j_{para} versus proton energy for one-minute interval at three different instants. The dashed lines are the plots at the event occurrence instant (12:24 UT, day 051); the dotted lines are those at 12:19 UT, five minutes before the event occurs; and the dot-dashed lines are those at 12:29 UT, five minutes after the event	97
5.1 From top to bottom, the first, second, third, and fourth panels show the plots of proton energy, pitch angle, perpendicular velocity, and parallel velocity versus interacting time for the event at 14:36 UT, day 045, and the energy band centered at 36 keV; the fifth shows the plot of wave frequency versus interacting time.	

Initial pitch angle of the proton is 40°	112
5.2 From top to bottom, the first and second panels show the plots of proton energy and pitch angle versus interacting time for 15 different values of initial pitch angle α_0 from 72° to 10° for the event at 14:36 UT, day 045; the third shows the plots of proton energy versus pitch angle for the same values of α_0 . The color code is the same for the three panels	113
5.3 From top to bottom, the first and second panels show the plots of proton energy and pitch angle versus interacting time for 15 different values of initial pitch angle α_0 from 86° to 80.1° for the event at 07:33 UT, day 073; the third shows the plots of proton energy versus pitch angle for the same values of α_0 . The color code is the same for the three panels	116
5.4 From top to bottom, the first and second panels show the plots of proton energy and pitch angle versus interacting time for 11 different values of initial pitch angle α_0 from 88.22° to 86° for the event at 12:24 UT, day 051; the third shows the plots of proton energy versus pitch angle for the same values of α_0 . The color code is the same for the three panels	120
5.5 From top to bottom, the first and second panels show the plots of proton energy and pitch angle versus interacting time for 7 different values of initial pitch angle α_0 from 35° to 5° for the event at 12:24 UT, day 051; the third shows the plots of proton energy versus pitch angle for the same values of α_0 . The color code is the same for the three panels	121

CHAPTER 1

INTRODUCTION

In this chapter we will give an overview on the Earth's magnetosphere, its proton populations, EMIC waves in its equatorial region and their interactions with protons, and the outline of the current dissertation.

1.1 The Earth's magnetosphere

The upper atmosphere of the Sun is so hot that materials there can escape the Sun's gravitational attraction, forming a steady streaming outflow called the solar wind. Owing to its high temperature and the constant illumination by the Sun, the solar wind is a fully ionized plasma, containing mainly protons, helium ions, and electrons. A weak magnetic field (about 7 nT near the Earth's orbit) is embedded in the solar wind plasma and called the interplanetary magnetic field (IMF) [e.g., *Hundhausen*, 1995].

When the solar wind encounters a magnetized object, such as the Earth with its geomagnetic field, it will confine the magnetic field into a limited region around the object. This leads to the formation of the Earth's magnetosphere, which is an elongated cavity, fairly blunt in the sunward direction, and nearly cylindrical for a long distance in the anti-sunward direction. Figure 1.1 shows a three-dimensional view of the Earth's magnetosphere [after *Stern and Ness*, 1982].

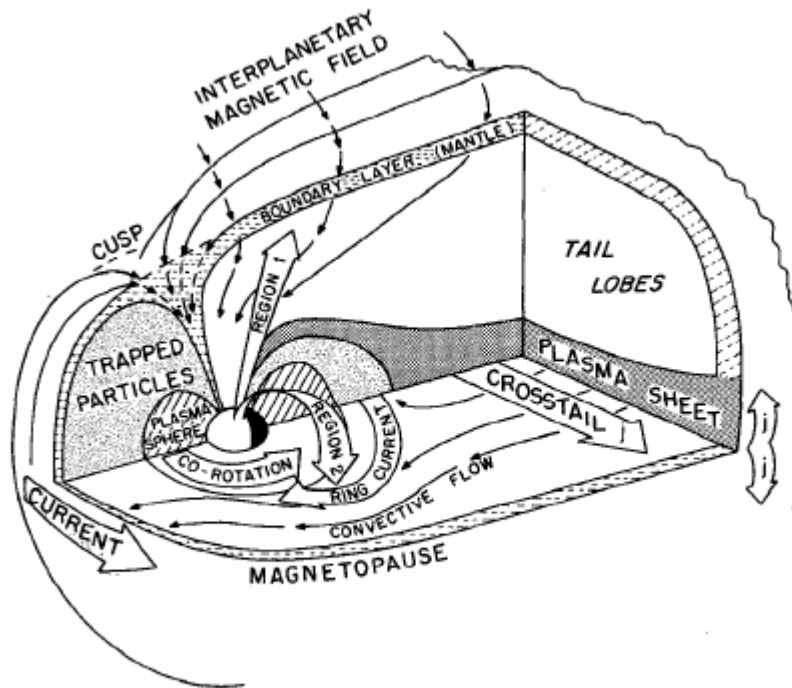


Figure 1.1 A three-dimensional view of the Earth's magnetosphere [after *Stern and Ness, 1982*].

The boundary of the magnetosphere is called the magnetopause that separates the region occupied by the Earth's magnetic field from the solar wind and the interplanetary magnetic field. The location of the magnetopause is determined by the balance between the pressure of the geomagnetic field, combined with the thermal pressure of the magnetospheric plasma, and the combined pressure of the solar wind and the IMF. Owing to the variability of the solar wind and the dynamics of the solar wind-magnetosphere interaction, the magnetosphere is never in a truly steady state, and in fact it is a dynamic and constantly changing structure.

There are two models of magnetospheres, the open one and the closed one, corresponding to different processes of transporting mass, momentum, and energy across the boundary [e.g., *Dungey*, 1961; *Axford*, 1964]. According to the open magnetosphere model [e.g., *Dungey*, 1961], the polar cap field lines extend out into the solar wind and connect with the IMF, providing access for the solar wind charged particles into the Earth's magnetosphere. The plasma sheet plays the role of a storage region for these particles. When the IMF connects to the Earth's magnetic field, it produces open field lines with only one foot on the Earth. Under the influence of the solar wind, the magnetic field lines in the northern and southern hemispheres are stretched into the magnetotail, forming the northern and southern tail lobes. These field lines reaching down the magnetotail have opposite directions on the northern and southern sides of the equatorial plane. As a result, a current sheet exists to separate the northern and southern tail lobes. The open field lines in the current sheet region reconnect to form closed field lines that convect back to the Earth.

The closed magnetosphere is the one in which the geomagnetic field lines close on themselves and form a closed system, and there is no merging with the IMF. In the closed model of the magnetosphere, all magnetic field lines have two ends on the Earth, and the magnetopause is a closed boundary that isolates the Earth's magnetic field from the solar wind and the IMF. According to *Axford and Hines* [1961], however, in this model 'viscous' interactions may occur, allowing plasma inside and near the flanks of the magnetosphere to be weakly coupled to the solar wind flow, possibly by waves that propagate across the boundary.

1.2 Proton populations in the magnetosphere

Protons within the Earth's magnetosphere belong to different populations with different energies and densities. The energies of these protons extend from thermal values (order of eV) to several hundred MeV. The primary sources of these protons, except those having energies in the MeV range, are the solar wind and the ionosphere. In terms of energies, proton populations may be divided into cold ones with energies of a few eV or less and hot ones with much higher energies.

Cold proton populations

Cold protons can be found in the ionosphere that is an ionized region of the Earth's upper atmosphere. Its lower boundary is located at 50 to 70 km in altitude whereas its higher boundary is not well-defined, but is typically at ~500 km in altitude. Although the ionosphere is not usually considered as part of the magnetosphere, it plays a role of a cold proton source of other regions in the magnetosphere.

Another region containing cold protons is the plasmasphere. This is the region defined by the magnetic field lines corotating with the Earth, located at the central core of the magnetosphere, above the ionosphere, and extending to $L \sim 4-6$. The plasmasphere's outside boundary is called the plasmapause. Within the plasmasphere cold protons are trapped on the corotating field lines and can reach high densities (10^2 to 10^4 cm^{-3}).

Outside the plasmapause, protons do not corotate with the Earth, but are connected to the magnetopause. The corresponding flux tubes expand to large volumes and may be connected to the solar wind plasma. As a result, equilibrium cannot be reached. This region constitutes the plasma trough whose cold proton density is of several cm^{-3} [e.g., *Decreau et al.*, 1982]. In this region, in situ observations have also found rather

dense, cold plasma structures that have been identified as detached plasma regions and plasma tails/plumes [e.g., *Chappell*, 1974; *Carpenter et al.*, 1993; *Moldin et al.*, 1996, 2003]. These structures are observed mainly in the noon-dusk quadrant, and their source is believed to be the erosion/drainage of the main plasmasphere owing to the effects of the convection electric field [e.g., *Moldin et al.*, 1996]. Cold protons can also be found in the polar wind that is formed by the cold plasma leaving the ionosphere.

Hot proton populations

There are many energetic proton populations inside the magnetosphere, which are far from thermal equilibrium. They have free energies associated with their non-equilibrium state, available for the excitations of waves.

Hot protons can be found in several boundary layers of the magnetosphere, including the polar cusps (or clefts), entry layers, plasma mantle, and low-latitude boundary layer. There are two cusps or clefts (one in each hemisphere). These are narrow, funnel-shaped regions, elongated in longitude, and extending down from the high latitude magnetosphere into the polar ionosphere at 70° - 80° geomagnetic latitudes. In each hemisphere there also exists an entry layer near the polar cusp region where the magnetic field is so weak that the magnetosheath particles can enter the ionosphere. As a result, the plasma in the cusps has much the same properties as the magnetosheath plasma, and the cusps are thus regarded as extensions of the magnetosheath plasma down to low altitudes, allowing a direct access of particles from the entry layers to the ionosphere and vice versa. The plasma mantle is a high-latitude boundary layer, extending anti-sunward from the cusp to the distant tail. It contains magnetosheath-like plasma with protons having

energies from several hundreds of eV to about 1 keV. The low-latitude boundary layer extends tailward from near the subsolar point. It also contains magnetosheath-like plasma.

The tail lobes are regions of low-density (less than 0.1 cm^{-3}) plasma outside the plasma sheet boundary layer and also contain hot protons. Their plasma source is the solar wind. The plasma sheet is a region around the neutral sheet, consisting of hot particles with nearly symmetric velocity distributions. The thickness of the plasma sheet is typically in the range of $4\text{-}6 R_E$. The plasma sheet ion population is a mixture of particles of solar wind (in quiet times) and ionospheric (in active times) origins [e.g., *Wolf*, 1995]. The plasma sheet also contains hot protons. The plasma sheet proton energy ranges from 1 to 20 keV, with an average of 5 keV, and the proton number density ranges from 0.1 to 3 cm^{-3} , with an average of 0.5 cm^{-3} .

Hot protons are also found in the ring current (RC) and the radiation belts. The ring current is composed of energetic (up to hundreds of keV) particles in primarily closed, Earth-encircling trajectories, in which ions gradient/curvature-drift westward and electrons eastward, and generally occupies the spatial region that extends from about $L=3$ to $L=7$, thus overlaps much of the outer plasmasphere and trough region [e.g., *Horwitz and Moore*, 2000]. Therefore, the outer plasmasphere and trough region may be considered in general as part of the ring current region. Protons are generally the dominant part of the ring current over O^+ and He^+ ions. Protons in the ring current come from either the ionosphere or the solar wind. The ionospheric ions could access to the RC region by either direct injection from the ionosphere upward along the magnetic field line or earthward injection from the plasma sheet. The radiation belts are the regions lying well inside

the magnetosphere where electrons and energetic ions including protons are long-term magnetically trapped. The energies of these protons extend up to several hundreds of MeV, making them the most penetrating of all particles in the magnetosphere. The extremely large energies, much larger than any electrical potential energy in the magnetosphere, suggest an energy source other than electric and magnetic fields associated with the Earth [e.g., *Walt*, 1994]. One source candidate of MeV protons is the cosmic ray albedo neutron decay (CRAND) process. This process is the one in which a neutron, which is produced in the Earth's atmosphere by collisions of cosmic rays with oxygen and nitrogen nuclei, decays into a proton, an electron, and an anti-neutrino. If the decay occurs while the neutron is moving through the trapping region, the resulting electron and proton can become magnetically trapped. The CRAND process dominates in the innermost region of the magnetosphere. Finally, the very high energy protons can directly penetrate the magnetosphere, owing to their very large Larmor radii [e.g., *Vacaresse et al.*, 1999]. It is found that the average energy of protons in the radiation belts increases with decreasing L value.

Precipitating protons are observed in the auroral region [e.g., *Cornwall et al.*, 1971; *Spasojevic et al.*, 2004]. It is believed that these protons are initially from the ring current or the radiation belts, later pitch angle scattered possibly by EMIC waves, then falling into the loss cone, and eventually being removed from trapping. When encountering the auroral ionosphere, those protons can produce detached subauroral proton arcs [e.g., *Spasojevic et al.*, 2004; *Fuselier et al.*, 2004].

Now we can see that in the outer plasmasphere and plasma trough region there are two distinct proton plasma populations: one cold and one hot. These regions are capable of supporting the generation/amplification of EMIC waves, as shown in Chapter 3.

Processes relating to proton populations

The mechanisms controlling the source, diffusion, and loss of particles in the magnetosphere are different in different energy ranges, and the boundaries between these different regimes are themselves moving with the level of magnetic activity. For example, regarding radial transport, electric field fluctuations dominate for low-energy particles and essentially explain the build up of the ring current whereas high-energy particles are mainly sensitive to major changes in the magnetic field.

Cold, plasmaspheric protons can be lost owing to the drift to the magnetopause. Energetic ring current protons can be lost owing to the drift to the magnetopause, charge exchange, and precipitation. The principal processes affecting trapped protons below 500 keV in the radiation belts are believed to be magnetic storm injection, charge exchange with neutrals, Coulomb collision, radial or L shell diffusion, and pitch angle scattering. The Earth's magnetic field can be drastically modified during very active periods. The outer L shells can then be opened to interplanetary space, and trapped protons on those shells can be lost through the magnetopause.

Plasmaspheric protons are subject to the radial transport owing to \mathbf{ExB} drift. Ring current protons are subject to the radial transport owing to \mathbf{ExB} drift and gradient/curvature drift. Radial diffusion of protons across L shells occurs frequently, even in magnetically quiet periods, as a result of acceleration and/or injection. It is well established that during the active periods, plasmas are injected earthward from the plasma

sheet from the nightside region. Particle acceleration and heating are known to accompany this process.

There is also a process called the pitch angle scattering. In this process the pitch angles of protons gyrating about the local magnetic field are changed. For those protons that are pitch angle scattered toward the local magnetic field, their pitch angles α are reduced. If their α fall into the loss cone, those protons are then removed from trapping. The loss cone is defined as a cone in the velocity space of the particles that are gyrating about the local ambient magnetic field line and mirroring between two mirror points such that those within this cone will strike the Earth's atmosphere and thereby be removed from trapping. Related to pitch angles of protons, there is another process called the shell splitting. This process causes the proton distributions to become more anisotropic as they drift from the nightside around the duskside to the dayside, and protons with small pitch angles prefer drifting to lower L shells while those with large pitch angles tend to drift to higher L shells [e.g., *Sibeck et al.*, 1987].

Another process also worth mentioning is the one called plasmasphere refilling, by which plasma containing protons and other particles is supplied to the plasmaspheric flux tube in the first place. If an empty flux tube is connected to the dense ionosphere, ionospheric plasma will flow up and accumulate in this flux tube until the plasma back pressure is sufficiently high to shut down further upward flow. This process occurs when the magnetic activity or the magnetospheric convection intensity decreases from high to low degree, making the boundary between the closed and open flux tube trajectories move outward. As a consequence, flux tubes that were previously on open trajectories

now reside on closed ones. Such flux tubes can retain the plasma injected and accumulated from the ionospheric field-aligned flows [e.g., *Horwitz and Moore, 2000*].

1.3 EMIC waves in the equatorial region of the magnetosphere

Wave observations

The Earth's magnetosphere with a highly structured configuration can sustain the generation and propagation of electromagnetic ion cyclotron (EMIC) waves. EMIC waves, with frequencies from ~ 0.1 to 5.0 Hz, have been observed in the equatorial region of the magnetosphere by numerous geostationary and elliptically orbiting spacecraft, such as ATS-1, ATS-6, DE-1, ISEE-1 and -2, AMPTE/CCE, and CRRES. EMIC waves have been observed on the ground as geomagnetic pulsations. Because the frequency range (~ 0.1 to 5.0 Hz) of EMIC waves is the same as that of the Pc 1-2 pulsations, these waves are alternatively called Pc 1-2 waves or sometimes simply Pc 1-2 pulsations.

The studies of *Bossen et al. [1976]* (ATS-1), *Kaye and Kivelson [1979]* (OGO-5), *Fraser [1985]* (ATS-6), *Ishida et al. [1987]* (ATS-6), and *Anderson et al. [1990]* (AMPTE/CCE) showed that EMIC waves occurred in the equatorial region over a wide range of L values, from $L \sim 3$ to the region near the magnetopause. *Anderson et al. [1992a]*, using data from the AMPTE/CCE satellite which covered the region from $L=3.5$ to 9 and magnetic latitudes between -16° and 16° , found that EMIC waves were more common at high L ($L > 7$) than at low L ($L < 6$) and occurred mainly from 03:00 to 18:00 MLT. A study by *Fraser and Nguyen [2001]*, using data from the CRRES satellite which covered the radial region of $L=3.5-8$ and magnetic latitudes between -30° and 30° ,

showed that EMIC waves occurred both inside and outside the plasmopause in the afternoon sector with a clear peak around 14:00 to 16:00 MLT and also in the morning sector with a minor peak around 05:00 to 07:00 MLT.

EMIC waves observed at lower L values are often associated with magnetic activities, such as recovery phases of magnetic storms and/or losses of the ring current ions [e.g., *Kintner and Gurnett, 1977*]. On the other hand, those observed at higher L values are more likely to be associated with sunward plasma convections [e.g., *Kaye and Kivelson, 1979*] or with plasma sheet ions [e.g., *Anderson et al., 1992b*].

Wave source region

One of the problems attracting much attention in EMIC wave studies is the location of EMIC wave generation region. The early theoretical studies of EMIC wave generation by *Cornwall et al. [1970, 1971]*, based on a pure proton model of magnetospheric plasma, showed that for wave growth to become significant, relatively high plasma number densities ($\geq 100 \text{ cm}^{-3}$) are required. They predicted that the onset of wave growth may be correlated with the plasmopause gradient density. As a result, the plasmopause should be the preferential region for EMIC waves to be generated because of the enhanced cold plasma density at this boundary. The study by *Fraser and Nguyen [2001]* as mentioned earlier in this section, however, showed that the plasmopause is indeed a region of EMIC wave generation and propagation, but not necessarily the preferential region, and that EMIC waves were observed not only inside but also outside the plasmopause.

Liemohn et al. [1967] analyzed middle latitude data and measured the wave dispersion to determine the magnetic field lines on which the waves were propagating. Their

results showed that the waves were propagating on magnetic field lines with equatorial intercepts between 4 and 9 R_E . Their results were in agreement with those of *Fraser* [1968] that showed that the wave generation region crosses the equatorial plane at positions between 4.5 and 9.5 R_E .

Criswell [1969], using the cyclotron resonance theory, showed that EMIC waves are generated in the magnetospheric regions where wave amplifications have maximum values. For the waves with $f=0.2-5$ Hz, the region is inside the plasmasphere, and for those with $f=0.3-1$ Hz, the plasmatrough is a possible candidate. Their results are to some extent in agreement with those of *Popecki et al.* [1993]. *Popecki et al.* [1993] used data obtained from three high-latitude stations, located at South Pole (-75° MLAT), Sondre Stromfjord ($+74^\circ$ MLAT), and Siple (-61° MLAT), to examine the source regions of EMIC waves. Their results revealed that for EMIC waves with frequencies above 0.4 Hz, the source region was the plasmopause region whereas for those with frequencies in the range 0.1-0.4 Hz, the source region was between the plasmopause and the magnetopause. *Mauk* [1982] also noted that there is a tendency for ion cyclotron waves to be generated in the regions of minimum magnetic field strength along the field lines. This again suggests the equator as the preferred source region.

Erlandson et al. [1990], using data from the Viking satellite (59° to 72° MLAT), found that the observed EMIC waves propagated nearly parallel to the ambient magnetic field lines and the field-aligned Poynting vector components were almost northward, away from the equator and downward toward the ionosphere. They suggested that the wave source was on approximately the same field lines as Viking, and presumably near

the equator. *Fraser et al.* [1992] performed a calculation of the Poynting vector, using data from the ISEE-1 satellite, and found that there was a tendency for the wave propagation to be nearly parallel or anti-parallel to the ambient magnetic field. *Labelle and Treumann* [1992] calculated the field-aligned Poynting vector component, using AMPTE/IRM data, and found that the wave propagation direction was away from the equator and the source region was located between 1.7° and 6.8° MLAT, north of the equator.

Wave frequency

In addition to measuring the wave frequency, f , it is often more beneficial to use the normalized frequency, X , defined as the ratio of f to the local proton cyclotron frequency, F_{CH} , when considering in situ satellite data. *Mauk and McPherron* [1980] and *Fraser* [1985] observed that at synchronous orbit X generally are between 0.05 and 0.6, corresponding to f from 0.1 to 1 Hz, over a magnetic latitude range of $\pm 10^\circ$. The observation by *Kaye and Kivelson* [1979], using data from the highly elliptic satellite (OGO-5, $L=7-14$, MLAT= -30° to 30°), showed that the frequencies of observed EMIC waves fell in the range from 0.09 to 0.63 Hz. *Bossen et al.* [1976], using data from ATS-1, found that wave frequencies were typically 10-20% of the equatorial proton cyclotron frequency, F_{Cheq} , and most waves observed had frequencies from 0.17 to 0.32 Hz.

Recently, *Anderson et al.* [1992a, b] using 7500 hours of data from the AMPTE/CCE satellite, which covered an L range from 3.5 to 9 at magnetic latitudes between $\pm 16^\circ$, provided detailed variations in X . From their results, X was shown to be dependent on L value and magnetic local time. Their results showed that the events with

$X < 0.25$ were observed mainly between 12:00-18:00 MLT while those with $X > 0.25$ were seen between 10:00-16:00 MLT, and at the same local time X tended to increase with L value. In the magnetic latitude range of $\pm 16^\circ$, their results showed that X decreased with absolute value of magnetic latitude, $|MLAT|$. Their results, however, showed no significant variation of f with $|MLAT|$.

Wave power

McPherron et al. [1972] showed that the power of EMIC waves observed by the ATS-1 synchronous satellite was much greater than that of their counterparts at the ground conjugate station. *Perraut et al.* [1978] found that the waves observed by GEOS-1 had an average amplitude between 0.3 and 1 nT. EMIC waves at high L values (7-14) near the equator, which were observed by the OGO-5 satellite, had large amplitudes, ranging from 2 to 8 nT [e.g., *Kaye and Kivelson*, 1979].

Recently, *Anderson et al.* [1992a, b] studied the wave power distribution over the L range from 3.5 to 9 and MLAT between $\pm 16^\circ$. According to their results, the average power spectral density of the observed waves was between 1 and 10 nT^2/Hz , corresponding to an average peak to peak amplitude from 1.0 to 3.5 nT. These results showed that the wave power tended to increase with local time from morning to afternoon for $L=5-9$; for the afternoon events, the typical peak to peak wave amplitude was about 2.5 nT whereas that for the morning events, it was only 1.6 nT.

Wave polarization

In the magnetosphere, the polarization plane of EMIC waves is found to be mainly perpendicular to the ambient magnetic field, indicating the transverse nature of

these waves [e.g., *Perraut et al.*, 1978; *Kaye and Kivelson*, 1979]. It is expected that EMIC waves are generated in the left-hand (LH) mode in the equatorial $L=4-8$ region of the magnetosphere by the electromagnetic proton cyclotron instability. Observations of EMIC waves by ATS-6, OGO-5, and GEOS-2 near the equator were consistent with this understanding, and the observed waves were mainly left-hand polarized [e.g., *Perraut et al.*, 1978; *Kaye and Kivelson*, 1979; *Mauk and McPherron*, 1980; *Perraut*, 1982; *Fraser*, 1985].

Waves observed off the equator, however, can be LH, RH (right-hand), or linearly polarized, depending on frequency. Waves with $X < 0.25$ are still mainly LH polarized, but some waves with frequencies between 0.1-0.2 Hz are often linearly polarized, possibly due to the presence of oxygen ions in the magnetospheric plasma [e.g., *Fraser*, 1985]. On the other hand, waves with $X > 0.25$ can be left-hand, linearly, or right-hand polarized [e.g., *Mauk and McPherron*, 1980; *Perraut*, 1982; *Fraser*, 1985].

Young et al. [1981] suggested that as the wave frequency passes through a crossover frequency introduced by the presence of ions heavier than protons, the wave polarization sense reverses, and the wave is linearly polarized at that frequency. When an EMIC wave propagates away from the equatorial region, at a frequency greater than an equatorial crossover frequency, into regions where the magnetic field strength is gradually increasing, the wave frequency will be eventually matched by the local crossover frequency, and the wave polarization changes from LH through linear to RH. Consequently, waves with $X > 0.25$ would be expected to be LH, RH, or linearly polarized, depending on the local crossover frequency at the location of the satellite when it is off the equator.

Anderson et al. [1992b] again contributed comprehensive results on the wave polarization in the $L=3.5-9$ region at magnetic latitudes between $\pm 16^\circ$. According to their results, there was a clear polarization distinction between morning (AM) events and afternoon (PM) events. While the PM events were significantly LH polarized, the AM events were significantly linearly polarized. Especially, the AM events for $L > 7$ showed a unique linear polarization, requiring a more extensive explanation because this contradicts the conventional theories of wave generation and propagation in a multi-component plasma. Their results also showed that the AM events were predominantly linear at all latitudes covered (0 to $\pm 16^\circ$ MLAT). This provided a challenge for theoretical work because these events had higher normalized frequencies ($X=0.4-0.5$) when compared to X of the waves observed in the other local time sectors. This finding cannot be explained by a change of polarization from LH to RH through linear mode when a crossover frequency is encountered during the propagation of waves from low to high magnetic field strengths. The authors suggested that the AM waves may be generated with linear polarization and the linear characteristic of wave polarization might not be a propagation effect. Not surprisingly, their results showed that the PM waves were uniformly LH polarized at all $|\text{MLAT}|$ below 10° , and became more linearly polarized at $|\text{MLAT}|$ above 10° , again supporting the conventional theory of EMIC wave generation.

1.4 Interactions between EMIC waves and protons

The interactions between EMIC waves and protons are of great interest in the studies on the dynamics of the magnetosphere and have been intensively investigated by

many authors. First, the results show that energetic (ten to several hundred keV) protons with an anisotropic ($T_{\perp} > T_{\parallel}$) population are believed to be the source of free energy for EMIC waves, and it is expected that EMIC waves with frequency below F_{CH} , the local proton cyclotron frequency, are generated and amplified favorably in the equatorial region at the energy expense of such protons through the electromagnetic proton cyclotron instability [e.g., *Cornwall*, 1965; *Kennel and Petschek*, 1966; *Watanabe*, 1966; *Criswell*, 1969; *Gary et al.*, 1994a], where T_{\perp} and T_{\parallel} are proton temperatures perpendicular and parallel to the ambient magnetic field \mathbf{B}_0 , respectively. Our study covers the electromagnetic proton cyclotron instability, as shown in Chapter 3.

Second, EMIC waves have capability of pitch angle scattering trapped protons of the ring current or radiation belts. It means that the pitch angles of the interacting protons can be altered during the time of interaction with EMIC waves. If owing to interactions with EMIC waves, the pitch angles of the interacting protons fall into the loss cone, these protons will later be lost when encountering the Earth's atmosphere. Such protons constitute the precipitation populations of protons observed in the auroral regions. *Fuselier et al.* [2004] and *Spasojevic et al.* [2004] investigated the existence of dayside subauroral proton arcs and found those features are caused by proton precipitations possibly as a result of pitch angle scatterings by EMIC waves that occur in the equatorial region. Similarly, *Frey et al.* [2004] found that the IMAGE spacecraft occasionally observed subauroral morning proton spots (SAMPS), and they interpreted those spots as the result of the interactions between EMIC waves and protons in the equatorial region of the magnetosphere. The process of scattering ring current protons into the loss cone occurs on time

scales of several hours and makes a significant contribution to the loss of protons from the trapped population [e.g., *Cornwall et al.*, 1970; *Lyons and Thorne*, 1972]. In their simulation studies, *Jordanova et al.* [1997] and *Kozyra et al.* [1997] considered the diffusive pitch angle scatterings of protons in the ring current by EMIC waves and found that it would take many hours to have significant losses of the proton populations. Via pitch angle scatterings, EMIC waves play a role in transferring energy from the ring current protons to ionospheric electrons. These electrons in turn could generate stable auroral red (SAR) arc spectra [e.g., *Cornwall et al.*, 1971; *Thorne and Horne*, 1992]. Our study also covers pitch angle scatterings of protons by EMIC waves, as presented in Chapter 4 and Chapter 5.

Erlandson and Ukhorskiy [2001] using wave and particle data from the DE-1 satellite showed a simultaneous occurrence of EMIC waves and enhanced proton fluxes in the loss cone for $3.5 < L < 5$, demonstrating that EMIC waves indeed scatter protons into the loss cone. *Yahnina et al.* [2000] using data from the low-altitude NOAA satellite and from the Sodankylä Geophysical Observatory, Finland also discovered a direct relationship between proton precipitation and ground Pc1 pulsations.

To complete the review of the interactions between EMIC waves and protons, it is worth mentioning a different approach employed by *Guglielmi et al.* [1999]. Their study is based on the ponderomotive forces exerted by EMIC wave fields on the interacting ions including protons and suggests that the ponderomotive effects play a role in formation of structure and dynamics of the equatorial region of the magnetosphere.

1.5 Outline of the current dissertation

The aim of the current study is (1) to examine the conditions under which the electromagnetic proton cyclotron instability acts as a generation mechanism for the EMIC waves observed by the SCATHA satellite in the magnetosphere, (2) to present in situ observations of proton pitch angle scatterings by EMIC waves in the magnetosphere, and (3) to propose a theoretical model for explaining these observations. The dissertation is organized as follows.

Chapter 2 describes the SCATHA satellite, its experiments, and spectral analysis techniques employed in the current study. The fast Fourier transform is used to obtain power spectral densities and to generate power spectrograms and dynamic displays of polarization ellipticity of EMIC waves. The procedures of processing SCATHA data using spectral analysis techniques are also presented in this chapter.

The electromagnetic proton cyclotron instability as a generation mechanism for EMIC waves observed by SCATHA is the focus in Chapter 3. This chapter describes how SCATHA data are prepared and how wave events are selected. It is also devoted to the methodology of investigating the instability and to the implementation of this investigation. A typical example is given in this chapter. The chapter concludes with the results and the main conclusions drawn from this investigation.

Chapter 4 gives details on the observations of proton scatterings by EMIC waves in the Earth's magnetosphere. It starts with data preparation and then shows observational results. Three examples will be given to depict three cases of proton scattering by EMIC waves.

Chapter 5 proposes a theoretical model for pitch angle scattering of protons by EMIC waves. Resonant cyclotron interactions between EMIC waves and protons will be introduced in detail. The chapter also shows how the pitch angle scattering of protons by EMIC waves takes place and gives explanations for the examples shown in Chapter 4.

Chapter 6 summarizes the main results and gives the conclusions drawn from the current study.

CHAPTER 2

INSTRUMENTATION AND SPECTRAL ANALYSIS TECHNIQUES

2.1 Introduction

The data used in our study are from the experiments onboard the SCATHA (P78-2) satellite. Therefore, in this chapter we will give descriptions of the satellite and its experiments. To identify EMIC waves from the SCATHA magnetic field data, we employ spectral analysis techniques. The calculations of spectra and polarization parameters of EMIC waves are performed by using the fast Fourier transform (FFT). The fast Fourier transform is an efficient and rapid method to obtain power spectral density estimates, and the FFT algorithm was popularized by *Cooley and Tukey* [1965], although some of the principles of this algorithm were first mentioned as early as 1903 [e.g., *Otnes and Enochson*, 1972].

In this study, the SCATHA magnetic field data employed take the form of vector measurements (x , y , and z components), which are evenly spaced in time. The time series of these data are analyzed in the frequency domain.

2.2 The SCATHA satellite

SCATHA stands for Spacecraft Charging At High Altitude. The SCATHA spacecraft was launched on January 30, 1979 into a near-synchronous orbit with a perigee of

5.3 R_E , an apogee of 7.8 R_E , and an inclination to the geographical, equatorial plane of 7.8° . The primary mission of SCATHA was to obtain information on the processes and effects of spacecraft charging. Its specific objectives included (1) obtaining environmental and engineering data to allow the creation of design criteria, materials, techniques, tests, and analytical methods to control charging of spacecraft surfaces and (2) collecting scientific data about plasma wave interactions, substorms, and the energetic ring current [Fennell, 1982].

The satellite's orbit period was ~ 23.6 hours, resulting in an eastward drift in longitude at a rate of $\sim 5.3^\circ$ per day and radial coverage at all MLTs. The spacecraft was spin stabilized with a spin period of one minute, and the spin axis was in the orbital plane and maintained approximately perpendicular to the sun-earth line. This allowed those experiments with view axes approximately perpendicular to the spin axis to scan a large range of angles relative to the local magnetic field, \mathbf{B}_o , and also allowed those sensors on the end of the spacecraft with fields of view parallel to the spin axis to be viewing nominally perpendicular to \mathbf{B}_o [Fennell, 1982].

The satellite was cylindrical and about 1.75 m in length and diameter. On orbit five experiment booms were deployed, including SC1, SC2, SC6, SC10, and SC11. The other experiments were SC3, SC4, SC5, SC7, SC8, SC9, and ML12. Most instruments were contained in the cylinder's belly band, an area around the middle of the cylinder while solar cells covered most of the remaining part of its side [see Figure 2.1]. The shorthand notations SC1, SC8, etc., were designated for each of the instruments on board SCATHA and have no special significance other than for accounting purposes [Craven *et*

al., 1985]. The twelve experiments had a total mass of 87 kg and consumed 110 W. There were three 3-m booms, a 2-m boom, and a 4-m boom, all for deployment of experiments. In addition, there was a 101.7-m tip-to-tip electric field antenna.

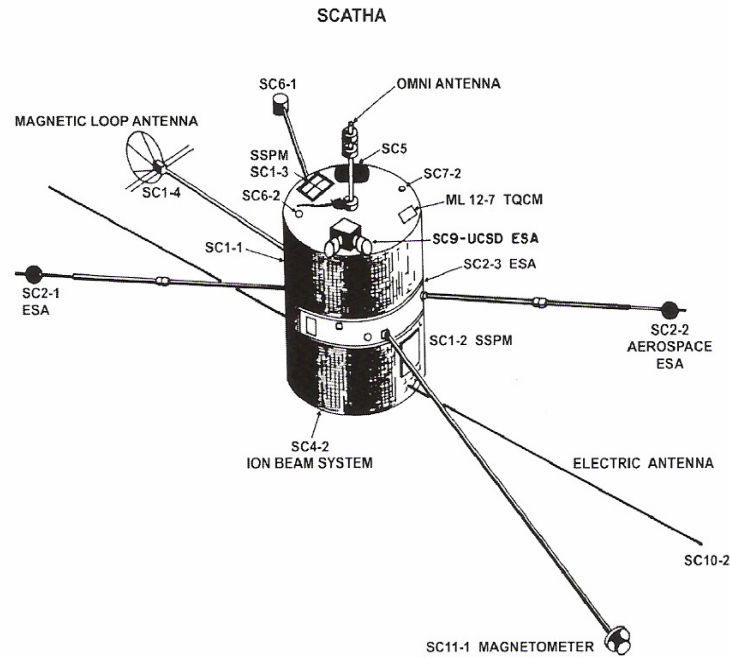


Figure 2.1 The SCATHA satellite and its instruments [after *Olsen and Norwood, 1997*]

The satellite's mission lasted nearly 12 full years and returned comprehensive particle and field measurements of the near-equatorial and near-synchronous space environment [*Spence et al.*, 1997]. Through a recovery effort at the Aerospace Corporation, these data have recently been made available. According to *Fennell et al.* [1997], the recovery effort produced High Resolution (HR) and Summary data sets that consist of data from the experiments: (a) SC1-8 experiment for measurements of VLF (very low frequency) magnetic and electric wave fields, (b) SC2 experiment for measurements of suprathermal plasma and energetic protons, (c) SC3 experiment for measurements of high

energy electrons, (d) SC10 experiment for measurements of electric field, and (f) SC11 experiment for measurements of magnetic field.

The HR data sets consist of the highest time resolution measurements from these experiments. These measurements have been converted to physical units and written onto magneto-optical disks in CDF format [Fennell *et al.*, 1997]. The HR data sets have been further processed to get Summary data at ~1-minute intervals. In this study we employed 59 days (year 1986) of HR magnetic field measurements from the SC11 experiment and summary data of proton spectra from the SC2 experiment.

The SC11 experiment

The Magnetic Field Monitor (SC11) experiment obtained triaxial measurements of the geomagnetic field. A triaxial fluxgate magnetometer was used, and the sensors were located at the end of a 4-m boom that was extended perpendicular to the satellite spin axis [Fennell, 1982], see Figure 2.1. The sensor axes were aligned accurately with the corresponding axes of the spacecraft. The magnetic field vectors were measured four times per second, resulting in a sampling interval of 0.25 second. Field resolution was approximately 0.3 nT with a dynamic range of approximately ± 500 nT per axis. Sensor response was from DC (direct current) to 70 Hz. A stringent magnetics control program was implemented onboard SCATHA to reduce absolute errors in the magnetic field measurements [Fennell, 1982].

The SC2 experiment

The SC2 experiment was designed to obtain the electron and ion distribution functions over a limited range of energy. It also measured the floating potential of the

graphite-coated spherical probes relative to the spacecraft background. It employed plasma sensors that consisted of three miniature analyzers. These sensors measured the fluxes of electron and ion distribution functions over a range of energy from several tens of eV to about 20 keV. Two of these analyzers (SC2-1 and SC2-2) were contained in the boom-mounted spherical probes, and the third (SC2-3) was mounted behind the center band of the satellite, see Figure 2.1. The fields of view of these analyzers were parallel to each other and to those of the energetic ion sensors. Plasma data obtained by the SC2-3 sensor, which was mounted on the satellite body, were included in the summary data [Fennell *et al.*, 1997].

The energetic proton (SC2-6) and ion plus background (SC2-3B) sensors provided measurements of protons, alphas, carbon, nitrogen, and oxygen ions (the CNO group) with emphasis on the pitch angle coverage with good resolution [Fennell *et al.*, 1997]. The experiment recorded the temporal, spatial, and directional variations in positive ion fluxes. The proton measurements covered the energy range from 17 keV to 3.3 MeV. The solid-state particle detection technique was used in the experiment to obtain instantaneous energy spectra for each one-second interval ($\sim 6^\circ$ angular sampling resolution). The proton detection system (SC2-6) employed a proton telescope that consisted of front and rear solid-state detectors behind a collimator-magnet assembly. After entering the collimator, particles passed through a uniform magnetic field that prevented electrons from being detected and contaminating the proton measurements. The uniform magnetic field had no influences on the proton trajectories. The detector in front was energy analyzed whereas the detector at rear eliminated penetrating particles from the analysis and

provided necessary background information. The proton analysis gave differential flux measurements in six energy windows, from 0.017 to 0.717 MeV, and two integral flux channels. The geometric factor of the proton telescope was $2 \times 10^{-3} \text{ cm}^2 \text{ sr}$. The temporal resolution was one second for protons, and 250 ms for alphas and the CNO group [Fennell, 1982].

The summary proton data were acquired at ten energy channels, seven from the SC2-3 sensor (centered at 0.154, 0.360, 0.88, 2.06, 3.60, 8.80, and 15.6 keV) and three from the SC2-6 sensor (centered at 36.0, 71.0, and 133.0 keV) [Fennel *et al.*, 1997]. For proton differential fluxes, ‘perpendicular’ refers to those having pitch angles of $90^\circ \pm 20^\circ$ for the SC2-3 measurements and $90^\circ \pm 10^\circ$ for the SC2-6 measurements; ‘parallel’ refers to those having pitch angles of $0^\circ \pm 30^\circ$ or $180^\circ \pm 30^\circ$. There are no measurements of fluxes of protons with pitch angles in between those referred to as ‘perpendicular’ and ‘parallel’.

We also use average energetic (0.15 to 133 keV) proton number density, n_h , and spacecraft ephemeris data, such as magnetic local times (MLT), magnetic latitudes (MLAT), L shell values, and spacecraft geocentric radii (*ERAD*). These data were included in the summary data. Further details are provided by Fennel *et al.* [1997]. n_h are needed for calculating EMIC wave convective growth rates, as shown in Chapter 3.

2.3 Spectral analysis techniques

2.3.1 Fast Fourier transform

The fast Fourier transform (FFT) algorithm can be employed to compute a Discrete Fourier transform (DFT). The DFT can be used to characterize the magnitude and

phase of a signal. Consider a finite sequence of N signal data points that are sampled at intervals of Δt , $x(j)=x(j\Delta t)$, where $j=0, 1, 2, \dots, N-1$, and Δt is the sampling interval. The DFT of $x(j)$, denoted as $X(n)$, has the form

$$X(n) = \sum_{j=0}^{N-1} x(j) \exp\left(-\frac{i2\pi nj}{N}\right) \quad (2.1)$$

for $n=0, \dots, N-1$, where $i=(-1)^{1/2}$. The inverse DFT is defined by

$$x(j) = \frac{1}{N} \sum_{n=0}^{N-1} X(n) \exp\left(\frac{i2\pi nj}{N}\right) \quad (2.2)$$

Equations (2.1) and (2.2) make up the Fourier transform pair. The value n in $X(n)$ is related to the frequency by

$$f(n) = \frac{n}{N\Delta t} \quad (2.3)$$

where N is the number of elements of the sequence considered and $N\Delta t$ the total length of the sample. Using Equation (2.1) implies that the analysis is undertaken in the frequency domain, and the sampling interval in the frequency domain is given by

$$\Delta f = \frac{1}{N\Delta t} \quad (2.4)$$

Δf defines the frequency resolution, and Δt the time resolution. It is seen from Equation (2.4) that the product of Δf and Δt is a constant for a given value of N . It indicates that increasing the frequency resolution reduces the time resolution and vice versa.

Because Equations (2.1) and (2.2) are of the same form, a single FFT algorithm can be used to perform both transformations, and we can pass between the time series $x(j)$ and its DFT $X(n)$ and back without losing information. The reason for using the FFT is its capability of time saving, owing to the efficiency of the FFT algorithm. The number of mathematical computations required is proportional to $N \log_2 N$ instead of N^2 for the direct implementation of the DFT if N is a highly composite number such as a power of 2.

The DFT yields frequency and amplitude information. If $x(j)$ is a sequence in the time domain, the sequence $X(n)$ can be regarded as the complex amplitude spectrum of the time sequence. At each frequency, the complex components are the amplitudes of a sine wave and a cosine wave, and their sum gives a sine wave that has amplitude of $\{X(n)X^*(n)\}^{1/2}$ and phase of $\tan^{-1} \{ \text{Im} (X(n))/\text{Re} (X(n)) \}$. The asterisk * denotes the complex conjugate.

2.3.2 Spectral analysis

The power spectrum of a signal, which is represented by a discrete time series $x(j)$ in the time domain, gives information on which frequencies contain the signal's power in

the form of a distribution of power values as a function of frequency. In the frequency domain, it is the square of $X(n)$, the DFT of the series $x(j)$.

2.3.2.1 Auto-power

Estimates of auto-power spectral density or the auto-power spectrum, $P_{xx}(n)$, of a time series $x(j)=x(j\Delta t)$, where $j=0, 1, 2, \dots, N-1$, is defined as

$$P_{xx}(n)=A|X(n)|^2=AX(n)X^*(n) \quad (2.5)$$

where $n=0, 1, 2, \dots, N-1$; $X(n)$ is defined in Equation (2.1), and $X^*(n)$ is its complex conjugate. A is the normalized factor that is equal to $2\Delta t/N$ [Otnes and Enochson, 1972].

For real data series, the estimates obtained from Equation (2.5) are symmetrical about $N/2$, and the number of independent frequencies is thus an integer equal to $N/2+1$. For $N/2+1 < n \leq N-1$, $P_{xx}(n)$ can be regarded as the power spectral density estimates for negative frequencies [e.g., Koreda *et al.*, 1977]. Equations (2.1) and (2.5) show that power spectral density estimates can be achieved by using the Fourier transform.

2.3.2.2 Cross-power

Estimates of cross-power spectral density or the cross-power spectrum, $P_{xy}(n)$, between two time series $x(j)$ and $y(j)$ is similarly defined as follows

$$P_{xy}(n)=AX(n)Y^*(n) \quad (2.6)$$

where $Y(n)$ is the Fourier transform of the time series $y(j)$ and $Y^*(n)$ its complex conjugate.

2.3.2.3 Problems associated with the fast Fourier transform

The power spectrum, obtained from a finite length of data using the FFT, is distorted, and considerable effort must be spent minimizing this effect. There are two potential problems associated with the power spectrum calculation using the FFT, namely aliasing and leakage. These problems exist inherently in the Fourier transformation and can give rise to spectrum distortion; consequently they should be well understood.

Aliasing

Consider a sinusoidal signal (wave), which is sampled at a uniform interval of time, Δt . If Δt is not chosen appropriately, high frequency components of the time series can fold back into the lower frequencies leading to distortion of the spectrum. In practice, it is impossible to distinguish without ambiguity frequencies above a certain value, called the folding frequency or Nyquist frequency, F_{NYQ} . The relationship between the Nyquist frequency and the sampling interval, Δt , is given by

$$F_{\text{NYQ}} = \frac{1}{2\Delta t} \quad (2.7)$$

Equation (2.7) shows that the sampling interval should be large enough to sample the highest frequency at least twice during each period [e.g., *Cooley et al.*, 1969]. In other words, it is necessary to have at least two samples per cycle to detect any frequency

component. The frequency interval, $0 \leq f \leq F_{\text{NYQ}}$, is called the principal interval. No power spectral density estimates can be obtained at frequencies above the Nyquist frequency.

To eliminate aliasing one can choose an appropriate sampling interval and low-pass filter the time series to filter out frequencies higher than F_{NYQ} before the Fourier transformation is performed. The sampling interval should be carefully chosen so that the spectrum of the time series is not aliased, and harmonics with frequencies higher than F_{NYQ} must be attenuated by a high-cut filter before the spectrum estimation is carried out. Alternatively, all powers above the Nyquist are removed before digitizing; this is done by applying an anti-alias filter to the analogue signal [e.g., *Gubbins*, 2004].

Leakage and windowing

It is implicit that a rectangular window exists for a finite sequence of N sampled points. The truncation of the time series can be considered as a multiplication of an infinitely long record by that window. The existence of this window leads to another problem, called leakage, because the Fourier transform of this window is a function of the form $\sin(x)/x$, which has a main peak and subsidiary peaks of decreasing amplitudes at nearby frequencies. These subsidiary peaks are called side-lobes, and their appearance gives rise to the leakage. Leakage is a problem because it can not only change the peaks in the power spectrum but also obscure the structure of the true spectrum. If leakage exists, the true spectrum of the time series is distorted because the main peak is altered by leakage to other frequencies. In other words, the effect of leakage is to smear the power spectral density (*PSD*). Since leakage is an inherent problem in the Fourier transformation of time series, it cannot be prevented but can be reduced. The procedure of reducing

leakage involves reducing or suppressing the heights of the side-lobes. To do this a technique, called windowing, is employed. Owing to the fact that the implicit rectangular window, as mentioned earlier, is the source of leakage, the obvious alternative is to modify the window shape. Before transforming, the time series $x(j)$ is therefore multiplied by a data window, $W(t)$, of width $T=N\Delta t$, which is no longer constant but maximum at the center ($t=1/(2T)$), symmetrical about $t=1/(2T)$, and tapers away toward the ends ($t=0, T$) [e.g., *Buckley*, 1971]. The applied window will effectively taper the data at the ends of the time series to the mean and reduce the heights of the side-lobes.

There are several windows that can be used for this purpose, such as Parzen, Hamming, and Hanning. No window is completely optimum. In this study the Hamming window is employed and is described as follows

$$W(t)=0.54+0.46\cos (2\pi t/T) \quad (2.8)$$

where t is time. The Hamming window is chosen due to its capability of minimizing the heights of the main side-lobes. If the Hamming window is applied to the time series $x(j)$ before the Fourier transformation, the modified auto-power spectral density will be

$$P_{xx}(n)=(A/U)|C(n)|^2 \quad (2.9)$$

where $C(n)$ is the DFT of $c(j)$, defined similarly by Equation (2.1), and $c(j)$ is the multiplication of the time series, $x(j)$, and the discrete form, $W(j)$, of the Hamming window $W(t)$, and

$$U = \frac{1}{N} \sum_{j=0}^{N-1} W(j)^2 \quad (2.10)$$

A similar process is also applied to obtain the modified cross-power spectral density [e.g., *Buckley, 1971*].

2.3.3 Polarization analysis

The interpretation of EMIC waves requires certain knowledge of the polarization of these waves. The contents of this section on wave polarization are based on the studies by *Fowler et al.* [1967], *Rankin and Kurtz* [1970], *Means* [1972], *Kanasewich* [1973], and *Koreda et al.* [1977]. The fundamental assumption is that EMIC waves are quasi-monochromatic.

Consider a wave propagating in the z direction with two perpendicular field components

$$h_x(t) = a_x \exp\{i(2\pi ft + \phi_1)\} \quad (2.11)$$

$$h_y(t) = a_y \exp\{i(2\pi ft + \phi_2)\}$$

In a right-handed Cartesian coordinate system, Equations (2.11) represent an elliptically polarized wave propagating in the direction perpendicular to the plane containing the h_x and h_y components. According to *Fowler et al.* [1967], the polarization of any wave can be characterized in terms of the covariance matrix elements of the wave field. The two-dimensional covariance matrix of the wave described by Equations (2.11) is defined as follows

$$J = \begin{bmatrix} \langle h_x(t)h_x^*(t) \rangle & \langle h_x(t)h_y^*(t) \rangle \\ \langle h_y(t)h_x^*(t) \rangle & \langle h_y(t)h_y^*(t) \rangle \end{bmatrix} \quad (2.12)$$

where the angle brackets represent the time average.

According to *Means* [1972], the covariance matrix is defined in terms of the two functions $h_x(t)$ and $h_y(t)$ that are analytic representations of a measured signal, and, as such, are complex. This fact complicates the generation of the analytic representation of the covariance matrix in the time domain. In the frequency domain, however, the analytic representations of a real signal are easily obtained by multiplying their Fourier transforms by the Heaviside step function

$$\begin{aligned} S(f) &= 0, & f < 0 \\ S(f) &= 1, & f \geq 0 \end{aligned} \quad (2.13)$$

and doubling the resultant values. Then by applying the Parseval's theorem

$$\int_{-\infty}^{\infty} g(t)h^*(t)dt = \int_{-\infty}^{\infty} G(f)H^*(f)df \quad (2.14)$$

where $G(f)$ and $H(f)$ are the Fourier transforms of $g(t)$ and $h(t)$, respectively, we can extend the definition of the covariance matrix to the frequency domain. The resulting matrix is

$$J = \begin{bmatrix} \{H_x(f)H_x^*(f)\} & \{H_x(f)H_y^*(f)\} \\ \{H_y(f)H_x^*(f)\} & \{H_y(f)H_y^*(f)\} \end{bmatrix} \quad (2.15)$$

where the braces represent the average over all the positive frequencies, and the functions $H_x(f)$ and $H_y(f)$ are the Fourier transforms of $h_x(t)$ and $h_y(t)$, respectively.

Equation (2.15) indicates that the covariance matrix elements are the average auto-power and cross-power spectral density estimates of the wave of interest. If the wave is monochromatic, the amplitudes (a_x and a_y) and phases (ϕ_1 and ϕ_2) are invariant with time. As a result, the wave field is totally polarized, and the covariance matrix J is equal to matrix P whose elements are the averaged P_{xx} , P_{xy} , P_{yx} , and P_{yy} , as defined earlier in Section 2.3.2.

For a totally polarized wave described by Equations (2.11), the locus of the end point of the field vector is an ellipse, called the polarization ellipse, which is contained in a rectangle of sides of $2a_x$ and $2a_y$. The ellipticity, ε , of the wave is defined as the ratio of

the minor axis to the major axis of the polarization ellipse. *Rankin and Kurtz* [1970] showed that

$$\varepsilon = \tan \beta \quad (2.16)$$

where

$$\sin \beta = 2 \operatorname{Im} (P_{xy}) / (P_{xx} + P_{yy}) \quad (2.17)$$

The angle of polarization, θ , between the major axis of the polarization ellipse and x-axis of the Cartesian coordinate system can also be obtained by

$$\tan 2\theta = 2 \operatorname{Re} (P_{xy}) / (P_{xx} - P_{yy}) \quad (2.18)$$

In general, the amplitudes (a_x and a_y) and phases (ϕ_1 and ϕ_2) are functions of time. For a quasi-monochromatic wave, the complex amplitudes (a_x and a_y) remain substantially constant only during a time interval, $\Delta\tau$, which is called the coherence time. Generally, a quasi-monochromatic signal may be considered as the sum of a totally polarized signal (monochromatic), whose polarization is characterized by the elements of covariance matrix P , and a completely unpolarized signal, whose polarization is characterized by the elements of covariance matrix U . Consequently, the covariance matrix of a quasi-monochromatic signal is now

$$J=P+U \quad (2.19)$$

For the totally polarized portion, there is a total coherence between the two signal components. On the other hand, there is no coherence between two components of the completely unpolarized portion. Due to the Hermitian property of the matrices J and P , the elements of U satisfy the following: $U_{xy}=U_{yx}=0$ and $U_{xx}=U_{yy}=D \geq 0$. Therefore

$$U = \begin{bmatrix} D & 0 \\ 0 & D \end{bmatrix} \quad (2.20)$$

From Equations (2.19) and (2.20), we have

$$\begin{aligned} J_{xx} &= P_{xx} + D \\ J_{xy} &= P_{xy} \\ J_{yx} &= P_{yx} = P_{xy}^* \\ J_{yy} &= P_{yy} + D \end{aligned} \quad (2.21)$$

By solving for D from Equations (2.21), we obtain

$$D = 1/2(J_{xx} + J_{yy}) \pm 1/2[(J_{xx} + J_{yy})^2 - 4\text{Det } |J|]^{1/2} \quad (2.22)$$

where $\text{Det } |J|$ is the determinant of the covariance matrix J . Because P_{xx} and P_{yy} are positive, only the negative sign before the radical is accepted [e.g., *Fowler et al.*, 1967]. Substituting for D in Equations (2.21) leads to

$$P_{xx}+P_{yy}=[(J_{xx}+J_{yy})^2-4\text{Det } |J|]^{1/2} \quad (2.23)$$

$$P_{xx}-P_{yy}=J_{xx}-J_{yy}$$

The polarization parameters can now be obtained as follows

a. Ellipticity

Similar to the case of monochromatic wave, for the case of quasi-monochromatic wave, we also have

$$\varepsilon = \tan \beta \quad (2.24)$$

From Equations (2.17), (2.21), (2.22), and (2.23), the value of β is given by

$$\sin \beta = 2\text{Im } (J_{xy}) / [(J_{xx}+J_{yy})^2-4\text{Det } |J|]^{1/2} \quad (2.25)$$

The sense of polarization is given by the sign of β , $\beta > 0$ for clockwise rotation when looking into the propagating wave (right-hand polarized), and $\beta < 0$ for counter-clockwise rotation (left-hand polarized).

b. Angle of polarization

By using Equations (2.18), (2.21), and (2.23), we obtain

$$\tan 2\theta = 2\operatorname{Re}(J_{xy}) / (J_{xx} - J_{yy}) \quad (2.26)$$

c. Degree of polarization

The degree of polarization of a quasi-monochromatic wave, denoted by R , is defined as the ratio of the polarized power to the total power. By definition we have

$$R = \operatorname{TR} |P| / \operatorname{TR} |J| = (P_{xx} + P_{yy}) / (J_{xx} + J_{yy}) \quad (2.27)$$

where $\operatorname{TR} |P|$ and $\operatorname{TR} |J|$ are the traces of the covariance matrices P and J , respectively.

From Equations (2.21), (2.22), (2.23), and (2.27), we find that

$$R = [1 - 4\operatorname{Det} |J| / (J_{xx} + J_{yy})^2]^{1/2} \quad (2.28)$$

d. Coherency

Coherency between the x and y components, denoted by C_{xy} , is given by

$$C_{xy} = |J_{xy}| / [J_{xx} J_{yy}]^{1/2} = [J_{xy} J_{yx} / J_{xx} J_{yy}]^{1/2} \quad (2.29)$$

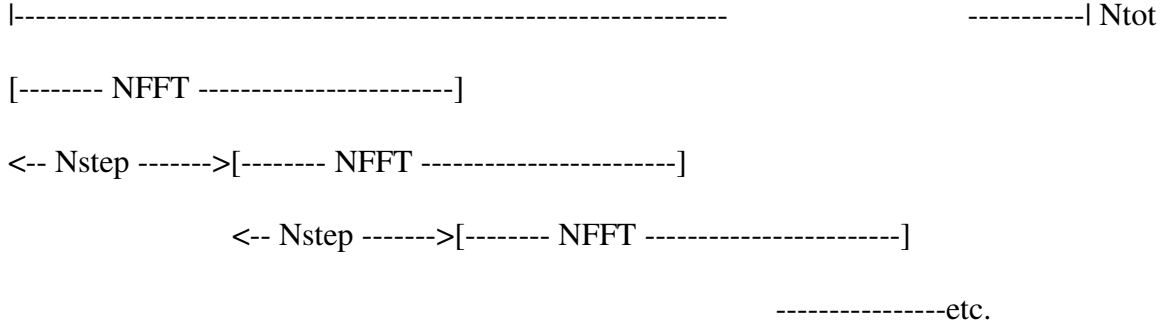
$C_{xy} = 1$ for a totally polarized signal, and $C_{xy} = 0$ for a completely unpolarized signal.

We now see that the elements of the covariance matrix and consequently the polarization parameters of a wave propagating in the z direction can be formulated and evaluated in terms of auto-power and cross-power spectral density estimates obtained from the measurements of x and y components.

2.3.4 Frequency-time analysis (dynamic analysis)

Dynamic spectral analysis, employing a representation of data in the frequency domain with time, has become popular in the field of time series analysis. In the current study, this technique is used to generate dynamic power spectra (or spectrograms) and dynamic displays of polarization ellipticity of EMIC waves identified from the SCATHA magnetic field component measurements.

The basic idea for this technique is to use a two-dimensional display to represent a three-dimensional quantity such as the wave power spectral density as a function of frequency and time. It is performed by sliding an FFT window along the time series record in steps of one minute or less and plotting successive spectra along a horizontal time axis. Thus, time is plotted on the abscissa and frequency on the ordinate. The third variable, which can be the wave power spectral density or polarization parameter at a certain frequency and time, will be represented by intensity modulation using a suitable color or grey scale palette. A diagram illustrating this technique is shown below



where N_{tot} is the total number of data points of the record, $NFFT$ the FFT length, and $Nstep$ the number of data points equivalent to a step of one minute or less. The number of FFT blocks ($Nblock$) calculated for a data record of the length N_{tot} , is given below

$$Nblock = (N_{tot} - NFFT) / Nstep \quad (2.30)$$

The product, $\Delta t Nstep$, where Δt is the sampling interval, gives the temporal resolution of the spectrogram. Before plotting, time-averaging is performed spectrum by spectrum using a certain number of adjacent blocks to reduce the variance and increase the statistical reliability.

2.4 SCATHA data processing procedures

2.4.1 Introduction

This study employed magnetic field data from the SCATHA satellite. To analyze the data, the procedures shown in the block diagram in Figure 2.2 were implemented. The aim of the SCATHA data analysis is to obtain dynamic power spectra and ellipticity of

EMIC waves from the three-component measurements of magnetic field, which will then be used to identify EMIC waves and to find their relationship with the concurrently observed proton spectra. The spectral analysis techniques, described in Sections 2.3 and 2.4, were adopted to generate those dynamic displays.

2.4.2 Data processing procedures

SCATHA data acquisition

We obtain 59 days of high resolution (HR) and summary SCATHA data contained in CDF (Common Data Format) files from Dr. Fennell (Space Science Laboratory, the Aerospace Corporation). From these files we extracted the three-component measurements of magnetic field in the GSM coordinate system, in the form of time series with a sampling interval of 0.25 second. By Equation (2.7), the Nyquist frequency is 2 Hz. The frequency range from 0 to 2 Hz is expected to capture the majority of EMIC wave events, as data from 700 CRRES orbits showed that less than 5% of the total number of EMIC wave events observed had frequencies above 2 Hz and no EMIC waves with frequencies above 4 Hz were found [e.g., *Fraser and Nguyen, 2001*]. Note that the CRRES satellite covered the radial region of $L=3.5-8$ and MLAT between -30° and 30° , compatible with that covered by SCATHA.

Data conditioning

The HR magnetic field time series were first subjected to procedures that remove data gaps and spikes, if any. The value of the first data point of a gap was set to be equal to the nearest previous true value, and this process continued to the end of the gap. The information in the gap under consideration is still not valid, but the information on both

sides of the gap remains valid, and on dynamic displays the gap corresponds to a blank chunk that contains no wave power. This gap removal process can handle as many data points as required. A detrending procedure, using a least-square second order polynomial, was also included to separate the variation part from the background geomagnetic field.

Coordinate conversion

The magnetic field data extracted from the CDF files are represented in the GSM coordinate system. Descriptions of the GSM coordinate system are given in the Appendix. Because EMIC wave properties are organized by the local ambient geomagnetic field \mathbf{B}_0 , a transformation from the GSM coordinate system to a field-aligned coordinate (FAC) system was then carried out prior to the Fast Fourier transformation and spectral analysis. The instantaneous magnetic measurements were resolved into three components of a right-handed system: one parallel to \mathbf{B}_0 , the others perpendicular to \mathbf{B}_0 .

Mean removal and windowing

Before performing the fast Fourier transformation, the mean of every subset of data was also removed and the Hamming window applied to reduce leakage, as discussed in Section 2.3.

Fast Fourier transformation

The three-component magnetic data sampled at 4 Hz were analyzed day by day. To obtain dynamic power spectra and polarization displays, the FFT was used, as discussed in Section 2.3. The FFT length N was chosen to be 240. Consequently, the frequency resolution is $\Delta f = 1/(N\Delta t) = 1/60 = 0.0167$ Hz. To perform dynamic spectral analysis, the 24-hour time series of magnetic field components were broken into 60-second (240

data point) overlapping segments. The portion of overlap was set at $2/3$, equivalent to a sliding step of 80 data points or 20 seconds ($Nstep=80$). The number of FFT blocks ($Nblock$) performed each day is given by Equation (2.30) with $NFFT=240$, $Nstep=80$, and the number of data points for each magnetic field component per day equal to $Ntot=24 \times 3600 \times (1/\Delta t)=345600$. As a result, the number of blocks to be displayed per day is 4318.

Smoothing

To increase the reliability of the results, time-averaging was also performed before plotting.

Dynamic power spectra and ellipticity displays

For each day, we generated dynamic power spectra of transverse and parallel magnetic components in the FAC coordinate system and displays of dynamic polarization ellipticity of EMIC waves in the frequency range from 0 to 2 Hz. The calculation of power spectral density was based on Equation (2.9), and the calculation of polarization parameters on Equations (2.24), (2.25), and (2.28). The obtained dynamic power spectra and ellipticity displays were used to identify the wave occurrences. We also produced plots of wave powers, ellipticity, and degree of polarization versus frequency for two-minute intervals of data. These plots were used to obtain values of PSD , wave peak frequency, ellipticity, and degree of polarization at any given time.

The block diagram of the processing of SCATHA magnetic data is shown in Figure 2.2.

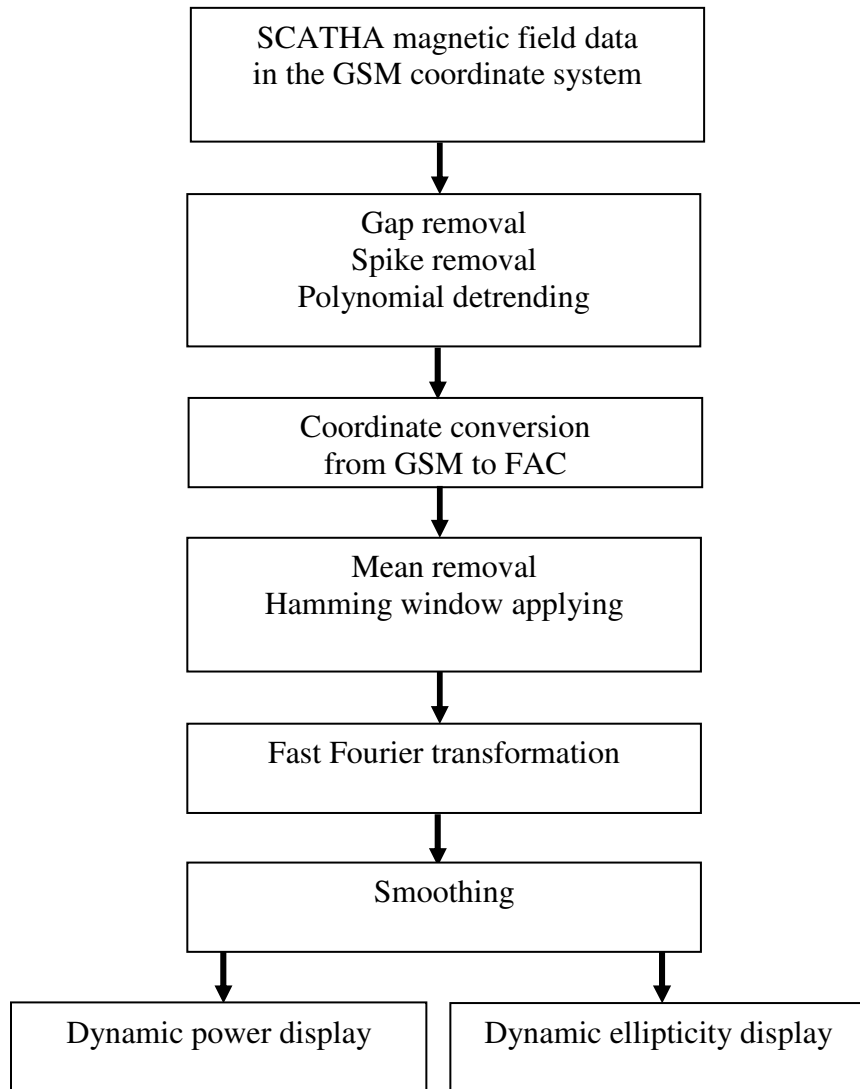


Figure 2.2 The block diagram of the SCATHA magnetic data processing.

2.5 Summary

The SCATHA magnetic field data in the form of time series with the sampling interval of 0.25 second are suitable for investigating EMIC waves in the equatorial region of the magnetosphere. Moreover, the availability of SCATHA proton spectra data makes possible the finding of the relationship between EMIC waves and protons in this region.

The fast Fourier transform is a very advanced and rapid technique for calculating wave power spectral density and polarization parameters from the measured magnetic field time series. For a finite sequence of N data points, the number of mathematical computations required for the DFT is proportional to $N\log_2 N$ instead of N^2 . There are two inherent problems associated with the FFT, namely aliasing and leakage. Solutions to both problems are also discussed. Because EMIC wave properties are organized by the local ambient geomagnetic field \mathbf{B}_0 , a coordinate conversion of the magnetic data from the GSM system to the FAC system is carried out prior to the fast Fourier transformation.

The wave power spectra obtained by employing the spectral analysis techniques will be used to study the electromagnetic proton cyclotron instability as a generation mechanism for EMIC waves, as described in Chapter 3. The dynamic spectral analysis technique is employed due to its capability of representing three-dimensional parameters on two-dimensional displays. In the current study, this technique is used to generate dynamic displays of wave power and polarization ellipticity. These displays will then be used to identify EMIC waves and to find their relationship with proton spectra, and the results will be presented in Chapters 4 and 5 along with discussions of these results.

CHAPTER 3

ELECTROMAGNETIC PROTON CYCLOTRON INSTABILITY

AS A GENERATION MECHANISM FOR EMIC WAVES

IN THE EARTH'S MAGNETOSPHERE

3.1 Introduction

As mentioned in Section 1.3, energetic (ten to several hundred keV) protons with an anisotropic ($T_{\perp} > T_{\parallel}$) population are believed to be the source of free energy for EMIC waves, and it is expected that EMIC waves with frequency below F_{CH} are generated and amplified favorably in the equatorial region of the magnetosphere at the energy expense of such protons through the electromagnetic proton cyclotron instability. Therefore, in this chapter, we will investigate the conditions under which the electromagnetic proton cyclotron instability acts as a generation mechanism for the EMIC waves observed by SCATHA in the Earth's magnetosphere.

Theoretical and experimental studies on electromagnetic proton cyclotron instability have been carried out by many authors, e.g., *Gary et al.* [1994a], *Gary and Lee* [1994], *Anderson et al.* [1994, 1996], and *Samsonov et al.* [2001, 2006]. These studies showed that there is an inverse correlation between proton temperature anisotropy A_p and proton parallel beta $\beta_{\parallel p}$ for this instability. $\beta_{\parallel p}$ is defined as

$$\beta_{\parallel p} = \frac{2\mu_0 n_p k_B T_{\parallel}}{B_0^2} \quad (3.1)$$

where n_p is the total proton number density, k_B the Boltzmann constant, and B_0 the magnetic field strength.

Several experimental studies of the local proton cyclotron instability in the magnetosphere have been conducted [e.g., *Mauk and McPherron*, 1980; *Anderson et al.*, 1996]. *Mauk and McPherron* [1980] used data from the ATS-6 geostationary satellite to show a good matching of predicted and measured frequencies, which is strong evidence that the linear, proton cyclotron instability mechanism is responsible for the observed EMIC waves. The study by *Anderson et al.* [1996], using data from the AMPTE/CCE satellite, showed that the occurrence of EMIC waves in the magnetosphere is consistent with the predictions of the local linear instability theory of proton cyclotron waves, proving the predictive capability of the linear theory. The study by *Anderson et al.* [1996], however, covered only dawn and noon wave events with $L > 7$. Using data from the SCATHA satellite, we extend the range of observations to all local time sectors with L values from 5.6 to 8.1 and MLAT from -13.7° to 15.6° .

3.2 Data preparation and event selection

Following the techniques described in Sections 2.3 and 2.4, the three-component magnetic data sampled at 4 Hz ($\Delta t = 0.25$ sec), obtained by SCATHA, were first detrended using polynomial curve fitting, and data gaps and spikes were removed. A transformation

from the GSM coordinate system to the field-aligned coordinate system was then carried out. A Hamming window was applied to the time series, and the mean was removed prior to Fourier transformation and spectral analysis. The FFT length was chosen to be $N=240$, resulting in a frequency resolution of 0.017 Hz by Equation (2.4). Wave spectra were obtained for transverse ($[\delta B_x^2 + \delta B_y^2]^{1/2}$) and parallel components with respect to the local ambient magnetic field \mathbf{B}_0 over the frequency range from 0 to 2 Hz.

Wave power spectral density, ellipticity, and degree of polarization values are extracted at 2-minute intervals with 0.25-second resolution to give quantitative measures of the power spectral density transverse to \mathbf{B}_0 , P_{tran} , and power spectral density parallel to \mathbf{B}_0 , P_{para} . These values were generated for both FAC system and GSM coordinate system. In the GSM coordinate system, we consider B_z as the ‘parallel’ component, and the ‘transverse component’ means the component perpendicular to B_z . In fact, in the equatorial region of interest in this study, the local z direction in the GSM coordinate system makes a small angle with respect to that of the local magnetic field line.

The P_{tran} spectra obtained in the FAC system show spin effects at 1 Hz and 2 Hz, but those in the GSM coordinate system do not. For any particular 2-minute interval, we found that, in the neighborhood of the peak, the dependences of P_{tran} on frequency in both coordinate systems are almost the same, and the magnitudes of P_{tran} in the two coordinate systems are different from one another by a nearly constant factor, whose value depends on the 2-minute interval considered. Therefore, for frequency and ellipticity in the neighborhood of the peak we used P_{tran} in the GSM coordinate system in place of P_{tran} in the FAC system without losing any information.

To allow quantitative analysis of a rather large quantity of data, each power spectrum of 480 points, corresponding to two minutes of data, was scanned automatically for peaks in the wave spectrum. To identify EMIC wave candidates, the following criteria were used: (1) The peak spectral power of transverse component P_{tran} must be at least one order of magnitude greater than the corresponding power background. (2) The peak frequency is above the Pc 3 range, i.e., ≥ 0.1 Hz. The Nyquist frequency in this study is 2 Hz so the range of peak frequency is from 0.1 to 2 Hz. This covers the range of Pc 2 waves (0.1-0.2 Hz) and part of the range of Pc 1 waves (0.2–5 Hz). As mentioned in section 2.4.2, this frequency range is expected to capture the majority of EMIC wave events. (3) In the neighborhood of the peak, the magnitude of P_{tran} must be significantly greater than that of P_{para} in the FAC system. Visual inspection of spectra, i.e., the corresponding plots of P_{tran} and P_{para} versus frequency in both coordinate systems for each 2-minute interval, was also performed to make sure only true EMIC waves were identified. In the 59 days of data examined, there were 1181 wave events defined as a two-minute interval during which EMIC waves occur with at least one peak in the transverse power as a function of frequency.

In order to focus upon events that were not influenced by the presence of He^+ ions, we excluded those with two peaks in the spectrum, one above and one below the local He^+ cyclotron frequency. This criterion eliminated 61 events. We then included only events for which SCATHA data provided the hot proton number density n_h needed for the calculation of the wave convective growth rate S . This resulted in the analysis of 520 events.

3.3 Methodology

3.3.1 Electromagnetic proton cyclotron instability

Due to various reasons, such as the presence of the lost cone in the trapped proton distributions, the pitch angle diffusion process, and perpendicular energizations of particles under inward, convective injection processes as a result of the $\mathbf{E} \times \mathbf{B}$ drift, the condition $T_{\perp} > T_{\parallel}$ is often observed in the magnetosphere and can give rise to electromagnetic proton cyclotron instability. Standard theories of waves in magnetized plasmas [e.g., *Swanson, 2003*] show that EMIC waves are generated when the proton perpendicular temperature T_{\perp} is greater than the proton parallel temperature T_{\parallel} . As pointed out by *Gary et al. [1976]*, when $T_{\perp} > T_{\parallel}$, electromagnetic proton cyclotron instability is not the only instability that may arise. But for a pure proton plasma, the fastest growing mode is the electromagnetic proton cyclotron instability that has maximum growth at $\mathbf{k} \times \mathbf{B}_0 = 0$, i.e., parallel propagation, and with left-hand circular polarization in that direction of propagation [*Gary, 1993*]. Therefore we will use the results from theoretical treatments of EMIC waves in the magnetosphere to analyze the events found in the SCATHA data.

3.3.2 Estimation of proton temperature anisotropy

For each of the selected events, we obtain the frequencies f_{peak} , f_{Max} , and f_{Min} . The peak frequency f_{peak} corresponds to the maximum value of P_{tran} ; f_{Max} and f_{Min} are the frequencies on either side of the peak frequency at which P_{tran} reduces to the power background. We always have $f_{\text{Min}} < f_{\text{peak}} < f_{\text{Max}}$ for any event. The experiments on board SCATHA also give us the local magnetic field strength B_0 from which we calculate X_{peak}

and X_{Max} , where $X_{\text{peak}}=f_{\text{peak}}/F_{\text{CH}}$ and $X_{\text{Max}}=f_{\text{Max}}/F_{\text{CH}}$, and $F_{\text{CH}}=qB_0/(2\pi m_p)$ is the local proton cyclotron frequency. The hot proton number density n_h is also given in the summary data. Using the available values of MLT, MLAT, L , and $ERAD$ (distance from the Earth's center to the location of interest), we estimate the value of the local electron number density, n , from empirical models. *Sheeley et al.* [2001] give an empirical formula for the total cold electron number density at the magnetic equator valid for $3 \leq L \leq 7$, using data from CRRES. For $L > 7$, we employ a decay rate of $L^{-4.0}$ [e.g., *Chappell*, 1974; *Sheeley et al.*, 2001]. The values of n at off-equator locations are estimated using the empirical model of field dependence of magnetospheric electron number density established by *Denton et al.* [2002]. Thus from the SCATHA data, we obtain the parameters needed for the calculations of linear convective growth rates of EMIC waves.

As pointed out by *Kozyra et al.* [1984], the effective amplification of waves in the Earth's magnetosphere depends on the time spent by the waves traveling through the growth region, which is of finite extent. Thus, the relevant quantity is the wave convective growth rate S rather than the temporal growth rate γ . S is the ratio of γ and the wave group velocity v_g .

In this investigation to calculate the linear convective growth rates S we use the formula established by *Gomberoff and Neira* [1983] for parallel propagation of EMIC waves in a pure proton plasma (ignoring the presence of ions heavier than proton such as He^+ , He^{++} , O^+) with the assumption that the distribution of energetic proton population is bi-Maxwellian. The formula is

$$S = \frac{\gamma}{v_g} = \frac{\sqrt{\pi}}{2\alpha_{\parallel}} [A_p(1-X)-X] \exp\left\{ \frac{-(1-X)^2}{\beta_{\parallel h} X^2} \left(\frac{1+\delta}{1-X} \right) \right\} / \left[X^2 \left(\frac{1+\delta}{1-X} \right) \right] \quad (3.2)$$

where $\beta_{\parallel h} = 2\mu_0 n_h k_B T_{\parallel} / B_0^2$, n_h is the hot proton number density, $\delta = n_{pc} / n_h$ the relative (cold to hot) proton number density, n_{pc} the cold proton number density, $\alpha_{\parallel} = (2k_B T_{\parallel} / m_p)^{1/2}$ the proton parallel thermal velocity, and m_p the mass of proton. A_p is the temperature anisotropy of the hot proton population, defined as

$$A_p = \frac{T_{\perp}}{T_{\parallel}} - 1 \quad (3.3)$$

For EMIC waves, $0 < \omega < \Omega_p$, where $\omega = 2\pi f$ and $\Omega_p = 2\pi F_{CH} = qB_0 / m_p$, we are interested in $0 < X < 1$, and from Equation (3.2), we see that if other parameters are kept constant, the sign of S depends upon the difference

$$\Delta = A_p - \frac{X}{1-X} \quad (3.4)$$

First we see that we only get growth ($S > 0$) when $X < 1$. We also see that the growth stops ($S = 0$) when $\Delta = 0$, so we identify the corresponding normalized frequency as X_{Max} , at which the EMIC emissions end, i.e.,

$$A_p - \frac{X_{\text{Max}}}{1 - X_{\text{Max}}} = 0 \quad (3.5)$$

As a result, we can determine A_p from the observed X_{Max} .

3.3.3 Estimation of proton parallel temperature

As mentioned earlier, with the availability of MLT, MLAT, L , and $ERAD$ values, the local total electron number density n was estimated by using the empirical models of *Chappell* [1974], *Sheeley et al.* [2001], and *Denton et al.* [2002]. The proton number density n_h was also included in the SCATHA Summary data, as noted in Section 2.2. Having obtained n and n_h , we deduce the cold proton number density n_{pc} by using the charge quasi-neutrality condition.

From Equation (3.2) we can see that given B_o , n , n_h , and A_p , the value of wave convective growth rate S is a function of X or frequency f with the proton parallel temperature T_{\parallel} as yet to be determined. Assuming that the peak frequency in the observed emission spectrum corresponds to the calculated peak in the convective growth rate allows the determination of T_{\parallel} . With A_p and T_{\parallel} available, the proton perpendicular temperature T_{\perp} is also obtained from Equation (3.3).

For examining polarization properties of the observed waves, for each event we also calculated ϵ_{peak} and ϵ_{ave} , where ϵ_{peak} is the value of ellipticity at the peak frequency, and ϵ_{ave} is the ellipticity weighted by transverse spectral power,

$$\text{i.e., } \epsilon_{\text{ave}} = \frac{\sum_{f_{\text{Min}}}^{f_{\text{Max}}} \epsilon P_{\text{tran}}}{\sum_{f_{\text{Min}}}^{f_{\text{Max}}} P_{\text{tran}}}, \text{ averaged over the frequency range from } f_{\text{Min}} \text{ to } f_{\text{Max}}.$$

For each event, we varied T_{\parallel} with a resolution of 0.1 keV to match the calculated peak frequency with the observed one. T_{\perp} was calculated using Equation (3.3), and β_{lp} was also calculated using Equation (3.1) with $n_p=n$.

From the observed spectrum for each event, we also calculated the ratio of $P_{\text{tran_Min}}/P_{\text{tran_peak}}$, where $P_{\text{tran_Min}}$ and $P_{\text{tran_peak}}$ are the values of P_{tran} in the GSM coordinate system at $f=f_{\text{Min}}$ and $f=f_{\text{peak}}$, respectively. For a comparison of the frequency spread of the calculated S about the peak frequency with that of the observed P_{tran} , we also calculated the ‘minimum’ frequency of S , f_{Min_S} , at which the corresponding value of the convective wave growth rate, S_{Min} , satisfies $S_{\text{Min}}/S_{\text{peak}}=P_{\text{tran_Min}}/P_{\text{tran_peak}}$, where $S_{\text{peak}}=S_{\text{Max}}$ is the value of S at f_{peak} , i.e., the maximum value of S . The observed frequency range from f_{Min} to f_{Max} about f_{peak} can be considered as the spread of P_{tran} , and that from the calculated f_{Min_S} to f_{Max_S} is considered as the spread of S about its peak frequency. From $X_{\text{Max}}=f_{\text{Max}}/F_{\text{CH}}$, Equation (3.2), and Equation (3.5), we made f_{Max_S} equal to f_{Max} . We found that the difference between the observed f_{Min} and the calculated f_{Min_S} was significant for only 2% of 520 events considered. The matching of the observed and the calculated features of the EMIC emission spectra supports the validity of the methodology and procedures employed in this investigation.

3.4 Example

We now consider in detail a typical 2-minute EMIC wave event, centered at 23:25 UT and occurring at 19.00 MLT, $L=6.12$, 6.43° MLAT, day 048, 1986. From top to bottom, the first panel of Figure 3.1 shows the plots of the wave percent polarization versus

frequency in the FAC (solid pink line) and GSM (dashed brown line) coordinate systems for this event; the second shows the wave ellipticity. The third shows the wave spectra for the same event; the solid pink line is P_{tran} in the FAC system; the dot-dashed black line is P_{para} also in the FAC system; and the dashed brown line is P_{tran} in the GSM coordinate system. The fourth panel shows the plots of the calculated wave convective growth rate S (dashed brown line) and P_{tran} in the FAC system (solid pink line) versus frequency for the same event.

From the first and second panels, we see (follow the vertical blue line from the top) that in the neighborhood of the peak frequency, the values of percent polarization and ellipticity in the FAC (the solid pink lines) and GSM (the dashed brown lines) coordinate systems are almost equal. From the third panel, we also see that in the neighborhood of the peak frequency, the dependences of P_{tran} on frequency in the two coordinate systems are nearly the same (the solid pink line and the dashed brown line), and the magnitudes of P_{tran} in the two system are different from one another by a nearly constant factor. From this panel, the spin effects in the FAC system at 1 Hz and 2 Hz are clearly seen in P_{tran} (the solid pink line) and P_{para} (the dot-dashed black line), but no spin effects are seen in P_{tran} (the dashed brown line) in the GSM coordinate system. Thus we use P_{tran} in the GSM coordinate system multiplied by the appropriate factor in place of P_{tran} in the FAC system. Also from the third panel, we easily see that in the neighborhood of the peak frequency, the value of P_{tran} (the solid pink line) is approximately an order of magnitude greater than that of P_{para} (the dot-dashed black line) in the FAC system, confirming the transverse nature of the EMIC waves in this event.

For this event we found that $f_{\text{peak}}=0.28$ Hz, $f_{\text{Max}}=0.35$ Hz, $f_{\text{Min}}=0.17$ Hz, the local magnetic field strength $B_0=101$ nT, the measured proton hot density $n_h=0.22$ cm⁻³ (from the SCATHA Summary data), and the total electron number density is taken to be $n=13$ cm⁻³ from the models. The peak ellipticity and averaged ellipticity for this event are $\epsilon_{\text{peak}}= -0.45$ and $\epsilon_{\text{ave}}= -0.48$, respectively, thus the observed waves are typically left-hand polarized.

Following the procedures outlined in Section 3.2 and Section 3.3, we obtained $A_p=0.3$, $T_{\parallel}=13.9$ keV, $T_{\perp}=18.0$ keV, and $\beta_{\parallel p}=7.1$. We found $f_{\text{Min}_S}=0.16$ Hz, and the difference between f_{Min} and f_{Min_S} is only 0.01 Hz. The calculated convective growth rate as a function of frequency for this event (the dashed brown line in the fourth panel) is compared to P_{tran} in the FAC system (the solid pink line in the same panel) for $T_{\parallel}=13.9$ keV in the neighborhood of the peak frequency. We see the excellent agreement among the minimum, peak, and maximum frequencies, but the observed spectrum is somewhat narrower than the calculated spectrum.

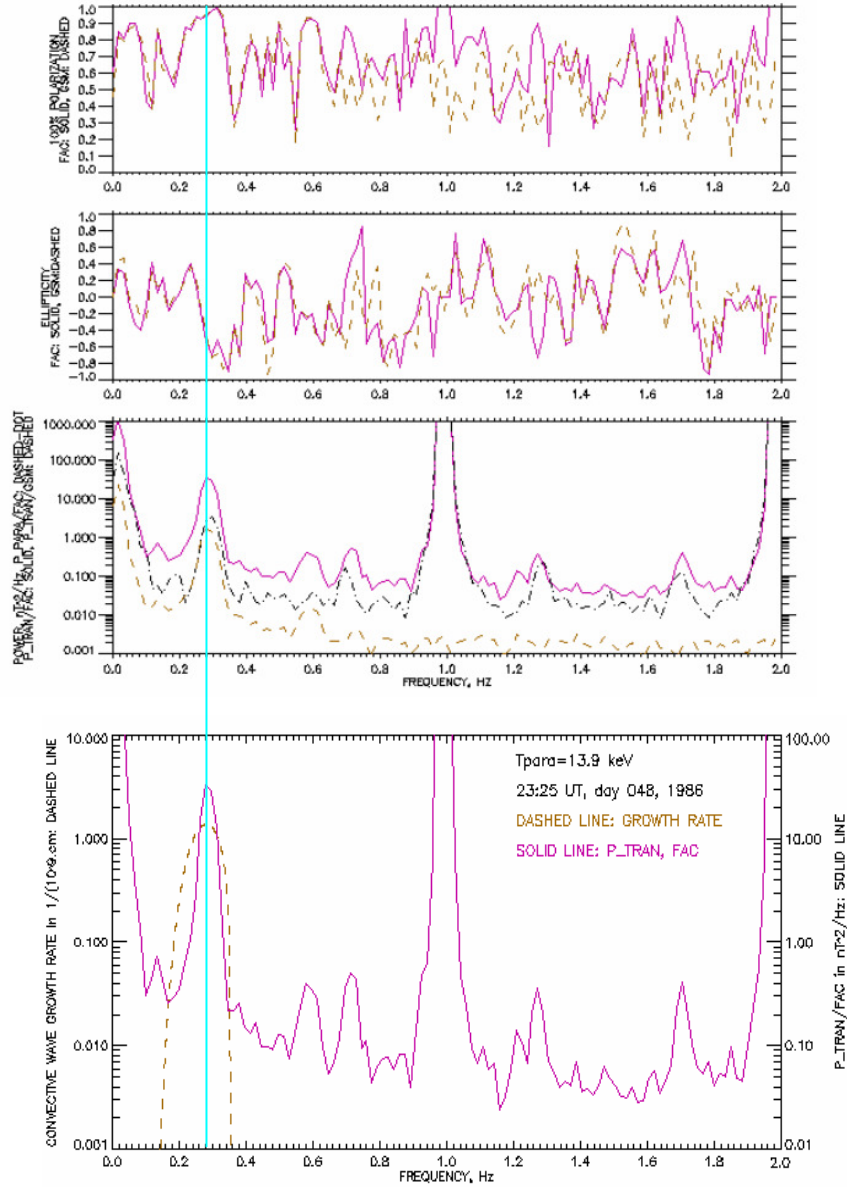


Figure 3.1 From top to bottom, the first panel shows the plots of wave percent polarization versus frequency in the FAC (solid pink line) and GSM (dashed brown line) coordinate systems for the 2-minute interval beginning at 23:24 UT, day 048; the second shows those of ellipticity. The third shows the wave spectra for the same event; the solid pink line is P_{tran} in FAC; the dot-dashed black line is P_{para} in FAC; and the dashed brown line is P_{tran} in GSM. The fourth shows the plots of the calculated convective growth rate S (dashed brown line) and P_{tran} in FAC (solid pink line) versus frequency for the same event.

3.5 Results and discussions

The 520 events are binned by MLT, ϵ_{ave} , and L values. The result of binning by MLT values shows that 71 events occurred between 03 and 09 MLT, the dawn sector; 299 between 09 and 15 MLT, the noon sector; 121 between 15 and 21 MLT, the evening sector; and 29 from 21 MLT through midnight to 03 MLT, the midnight sector. The number of events occurring in the noon sector is greater than those in the other local time sectors, in agreement with the result of *Anderson et al.* [1992a] study using APMTE/CCE data that covered nearly the same MLAT range as ours, as shown in their Figure 8. The result of binning by ϵ_{ave} values shows that 311 events occurred with ϵ_{ave} between -1 and -0.1, treated as left-hand polarized; 135 with ϵ_{ave} between -0.1 and 0.1, linearly polarized; and 74 with ϵ_{ave} between 0.1 and 1, right-hand polarized. This result is consistent with that of *Anderson et al.* [1992b] (see the bottom panel of Figure 6 in their paper) and that of *Fraser and Nguyen* [2001] (see Figure 10 in their paper). Binning the data by L values shows that 35 events occurred in the region of L between 5.6 and 6; 196 in that of L between 6 and 7; and 289 with L between 7 and 8.1. The number of events occurring in the region of L between 7 and 8.1 is greater than that in the region between 5.6 and 7, consistent with the finding of *Anderson et al.* [1992a] that EMIC waves were more common at high L ($L > 7$) than at low L ($L < 6$), as mentioned in Section 1.3.

3.5.1 Inverse correlation between proton temperature anisotropy and proton parallel beta

In a simulation study, *Gary et al.* [1994a] showed that, in the framework of the linear instability theory, the threshold value of the proton temperature anisotropy is related to the proton parallel beta by the expression

$$A_p = S_p \beta_{\parallel p}^{\alpha_p} \quad (3.6)$$

where S_p is of order unity, but varies as a function of temporal growth rate, and $\alpha_p \cong -0.40$ ($\alpha_p < 0$) independent of temporal growth rate for $0.05 \leq \beta_{\parallel p} \leq 5.0$. Experimentally, *Anderson and Fuselier* [1993] and *Anderson et al.* [1994] using the AMPTE/CCE satellite data for the subsolar magnetosheath region found the same functional form of the relation between A_p and $\beta_{\parallel p}$ as Equation (6) with $S_p = 0.85$ and $\alpha_p = -0.48$, showing that the observed anisotropy values were higher than the thresholds. In the dawn sector of the magnetosphere, *Anderson et al.* [1996] studied EMIC waves with $L > 7$ using data from the AMPTE/CCE satellite and found that the values of A_p were also above the threshold values as expected. They found the same empirical relationship applied in this region as in the magnetosheath for active times with S_p the same and only a slight change in α_p from -0.48 to -0.52 . In the noon sector of the magnetosphere, however, the *Anderson et al.* [1996] data showed $S_p = 0.2$, much smaller than that in the dawn sector. They attributed the lower limit for the noon events to the presence of unmeasured cold plasma. It is to be recalled that in this analysis we use an estimate of the cold plasma number density based

on empirical models and a measured value of the hot proton density obtained from the SCATHA data. *Kennel and Petschek* [1966] pointed out that a sufficient anisotropy is required for EMIC waves to grow and wave particle interactions will then force the particle distribution toward a marginal linear stability state. The anisotropy causing the wave growth is therefore diminished and subsequent wave growths slowed, leading to a final state where the plasma remains close to the ion cyclotron instability threshold curve.

The current investigation shows that Equation (3.6) holds for the SCATHA data and also for different MLT sectors and L ranges with corresponding values of S_p and α_p . A fit to our full data of A_p and β_{lp} yields $S_p=0.70$ and $\alpha_p= -0.34$ with a correlation coefficient $R= -0.63$. The results for binned data are shown in Figure 3.2. The upper panel of this figure shows a scatter plot of A_p versus β_{lp} with the data binned by MLT values and color-coded; the four dotted lines are the fitting curves for four different MLT sectors. From this panel, we see that the events occurring in the dawn sector (blue diamonds) have rather high A_p and mainly low β_{lp} (<3) except for two with $\beta_{lp}>10$. The events in the noon sector (red triangles) have a bigger spread in values of A_p with a concentration at high A_p and span nearly the entire range of β_{lp} with a concentration at low β_{lp} (<4). Those in the evening sector (green squares) concentrate at low values of A_p and high values of β_{lp} . It is interesting to see that the events in the midnight sector (black crosses) are limited to a rather narrow region of low values of both A_p and β_{lp} . A fit to the data for each sector results in different values of S_p , α_p , and R , as shown in Table 2.1. From the table, for the dawn sector with $L>7$, we have $S_p=0.63$ and $\alpha_p= -0.37$; these values are different from those of *Anderson et al.* [1996] ($S_p=0.85$ and $\alpha_p= -0.52$); this difference may

be due to the fact that we used more events (69) than they did (12) and they considered events with the averaged value of maximum normalized temporal growth rate, γ_m/Ω_p , of 2.5×10^{-2} , much greater than the value of 0.62×10^{-2} for the 69 events considered here. Higher γ_m/Ω_p correspond to more energy the waves can get from the interacting proton populations and thus higher A_p are expected.

The lower panel shows the same scatter plot as the upper panel, but the data are binned by L values; the three dotted lines are the fitting curves for three different L ranges. From this panel, we see that the events in the region of L between 7 and 8.1 (red squares) clearly have higher values of A_p than those in the region of L between 5.6 and 7 (brown diamonds and blue triangles). It appears that higher L corresponds to higher A_p . This is consistent with the consequences of the drift shell splitting process, as described in Section 1.2. Similarly, a fit to the data for each L range leads to different sets of S_p , α_p , and R . Table 3.2 summarizes the radial variation of the A_p - β_{lp} relation.

Gary et al. [1994a] denoted γ_m as maximum temporal growth rate, used the linear Vlasov theory, and found that with the value of $T_{\parallel e}/T_{\parallel p}=0.25$, where $T_{\parallel e}$ is the electron parallel temperature, and the normalized Alfvén velocity of $v_A/c=10^{-4}$, $S_p=0.35$ and $\alpha_p=-0.42$ for $\gamma_m/\Omega_p=10^{-4}$; $S_p=0.43$ and $\alpha_p=-0.42$ for $\gamma_m/\Omega_p=10^{-3}$; $S_p=0.65$ and $\alpha_p=-0.40$ for $\gamma_m/\Omega_p=10^{-2}$. *Samsonov et al.* [2001] solved the linear Vlasov dispersion equation as a function of β_{lp} for a pure proton plasma to find the threshold conditions for the electromagnetic cyclotron instability and the mirror instability assuming fixed γ_m/Ω_p for each instability, and found that the relation (3.6) holds for both instabilities. For the electromagnetic cyclotron instability, their results gave the values of S_p and α_p that are almost

equal to those found by *Gary et al.* [1994a], for $0.01 \leq \beta_{lp} \leq 10.0$ and the same three values of γ_m/Ω_p , see Figure 1 in their paper. Recently, *Samsonov et al.* [2006], using magnetosheath data from Cluster, found that for low β_{lp} ($\beta_{lp} < 1.0$) the observed proton temperature anisotropy A_p is in agreement with the proton cyclotron threshold and for higher β_{lp} ($\beta_{lp} \geq 1.0$) the observed A_p is close to both proton cyclotron threshold and mirror threshold, as shown in their Figure 10. To compare our results with those of *Gary et al.* [1994a], we also calculated γ_m , by using $\gamma_m = S_{\text{Max}} v_g$, and γ_m/Ω_p that is the value of γ_m normalized to the local proton cyclotron frequency. Figure 3.3 shows a scatter plot of A_p versus β_{lp} with the data binned by γ_m/Ω_p values and color-coded. The long-dashed blue line depicts the relation found theoretically by *Gary et al.* [1994a] for $\gamma_m/\Omega_p = 10^{-4}$; the short-dashed red line depicts that for $\gamma_m/\Omega_p = 10^{-3}$; and the dot-dashed green line for $\gamma_m/\Omega_p = 10^{-2}$. From this figure, we see that the A_p values found are all above the corresponding thresholds for different ranges of γ_m/Ω_p , and that in general for a given value of β_{lp} , higher γ_m/Ω_p corresponds to higher A_p . This supports the finding that EMIC waves get free energy from energetic protons with an anisotropic distribution; proton populations with higher A_p provide more energy for the waves, leading to higher values of γ_m/Ω_p .

We found that there is no clear dependence on ellipticity; thus we did not show parameters as a function of ellipticity.

The finding that S_p varies with MLT sector and L range is in agreement with the argument by *Gary et al.* [1994b] that this coefficient depends on macroscopic factors, particularly how hard external forces drive the energetic proton temperature anisotropy.

Table 3.1 Summary of the relationship between A_p and β_{lp} through the coefficients S_p and

α_p of the relation $A_p = S_p \beta_{lp}^{\alpha_p}$ and the correlation coefficients R for different MLT ranges.

MLT	S_p	α_p	R	No. of events
03<MLT<09 (Dawn sector)	0.63	-0.37	-0.82	69
09<MLT<15 (Noon sector)	0.75	-0.34	-0.45	299
15<MLT<31 (Evening sector)	0.65	-0.32	-0.89	121
21<MLT<03 (Midnight sector)	0.61	-0.20	-0.73	29
All	0.70	-0.34	-0.63	518

Table 3.2 Summary of the relationship between A_p and β_{lp} through the coefficients S_p

and α_p of the relation $A_p = S_p \beta_{lp}^{\alpha_p}$ and the correlation coefficients R for different L ranges.

L values	S_p	α_p	R	No. of events
$L < 6$	0.63	-0.32	-0.90	35
$6 < L < 7$	0.57	-0.28	-0.81	196
$L > 7$	0.81	-0.27	-0.43	289
All	0.70	-0.34	-0.63	520

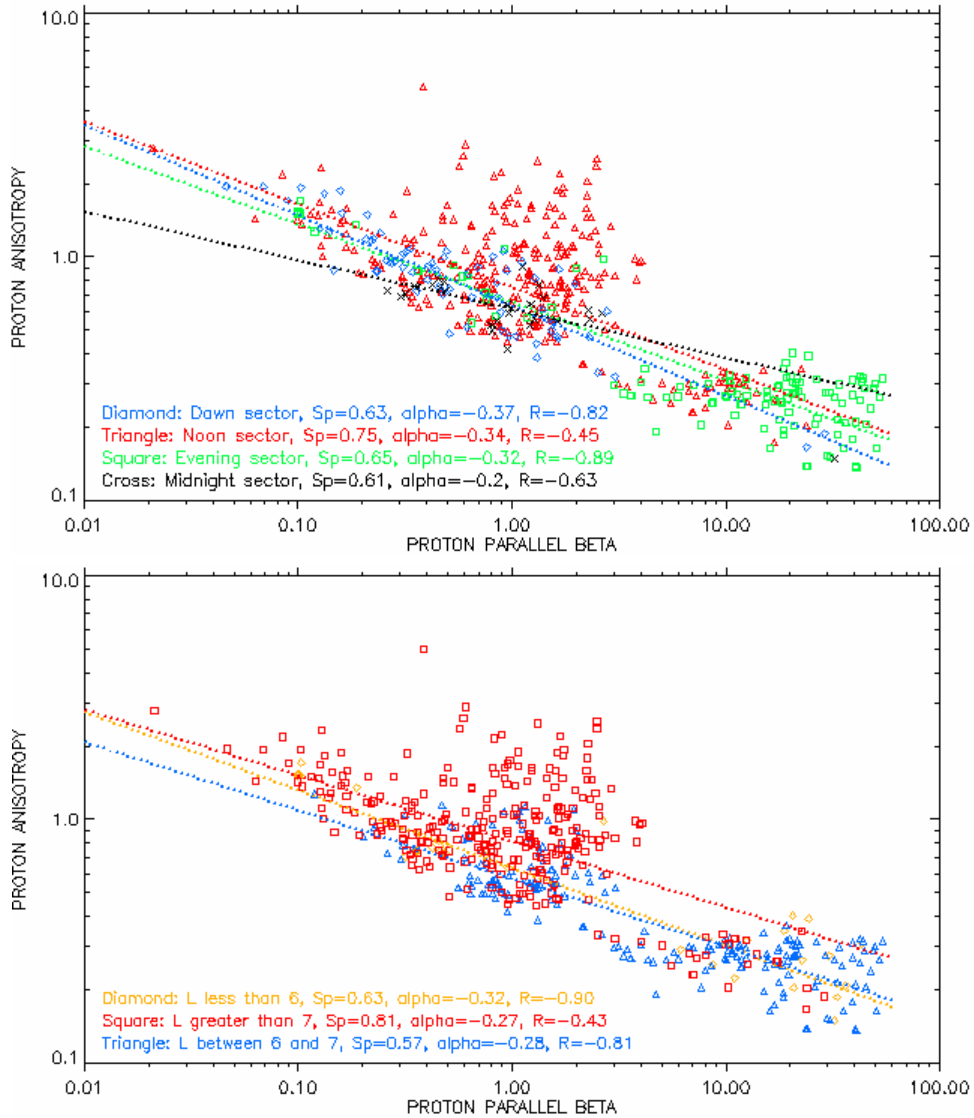


Figure 3.2 The upper panel shows a scatter plot of proton temperature anisotropy versus proton parallel beta with the data binned by MLT values and color-coded; the four dotted lines are the fitting curves for four different MLT sectors. The lower panel shows the same scatter plot as the upper panel, but the data are binned by L values; the three dotted lines are the fitting curves for three different L ranges.

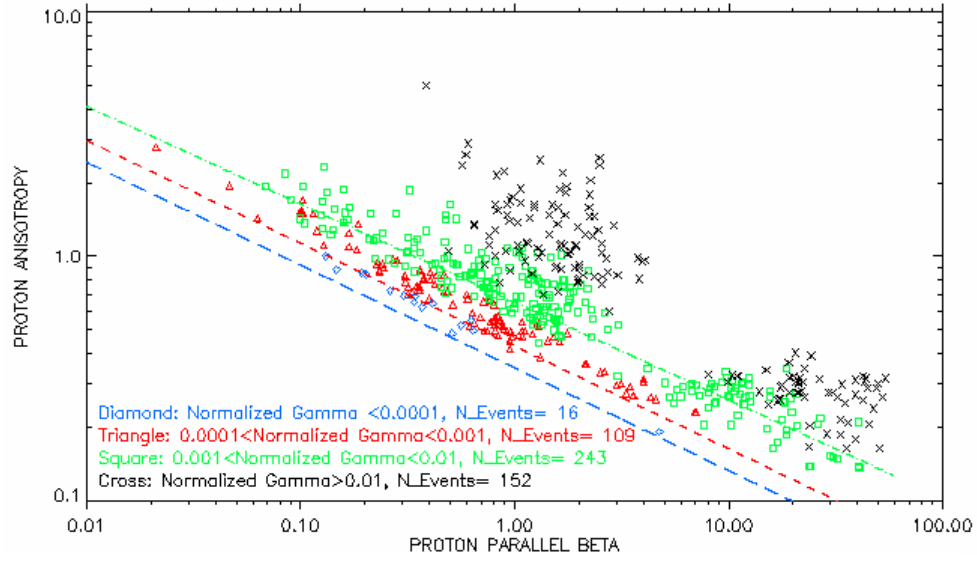


Figure 3.3 A scatter plot of proton temperature anisotropy versus proton parallel beta with the data binned by maximum normalized temporal growth rate values, γ_m/Ω_p , and color-coded. The long-dashed blue line depicts the relation given by *Gary et al.* [1994a] for $\gamma_m/\Omega_p=10^{-4}$; the short-dashed red line depicts that for $\gamma_m/\Omega_p=10^{-3}$; and the dot-dashed green line for $\gamma_m/\Omega_p=10^{-2}$.

3.5.2 Dependence of proton temperature anisotropy on proton perpendicular temperature

Each panel of Figure 3.4 shows a scatter plot of A_p versus T_{\perp} with the same format as Figure 3.2. From either panel, we see that for EMIC waves to be destabilized in general lower T_{\perp} requires higher A_p . This is consistent with a finding that the free energy source of EMIC waves is energetic protons with an anisotropic distribution. Consider two energetic and anisotropic ($T_{\perp} > T_{\parallel}$) proton populations with the same T_{\perp} , and we expect that the one with higher A_p can give more energy to the waves than the other. As a result, given a low value of T_{\perp} the corresponding value of T_{\parallel} must be small enough so that A_p is high enough to give sufficient energy for the waves to grow or to be amplified. From each panel, we also see that A_p and T_{\perp} follow the relation

$$A_p = aT_{\perp}^b \quad (3.7)$$

where a and b are constants. When all 520 events are included, a fit to the data gives $a=1.36$ and $b=-0.34$ with $R=-0.66$.

From the upper panel of Figure 3.4, we see that the events occurring in the dawn sector (blue diamonds) and in the noon sector (red triangles) are more likely to have lower values of T_{\perp} while those in the evening sector (green squares) are more likely to have higher values. Again we see that the events in the midnight sector (black crosses) have a rather narrow range of low values of T_{\perp} from 2 to 20 keV. Table 3.3 summarizes the MLT variation of the A_p - T_{\perp} relation in Equation (3.7).

From the lower panel of Figure 3.4, we see that the events in the region of L between 5.6 and 6 (brown diamonds) are more likely to have high values of T_{\perp} while those in the region of L between 7 and 8.1 (red squares) concentrate at lower values of T_{\perp} and those with of L between 6 and 7 (blue triangles) are fairly evenly distributed over the observed range of T_{\perp} . Table 3.4 summarizes the radial variation of the A_p - T_{\perp} relation.

We again see that the coefficients a and b in Equation (3.7) vary with local time and L value. This is what is expected from the argument presented by Gary *et al.* [1994b], as described in the last paragraph of Section 3.5.1.

Table 3.3 Summary of the relationship between A_p and T_{\perp} through the coefficients a and b of the relation $A_p = aT_{\perp}^b$ and the correlation coefficients R for different MLT sectors.

MLT	a	b	R	No. of events
03<MLT<09 (Dawn sector)	1.82	-0.46	-0.81	71
09<MLT<15 (Noon sector)	1.06	-0.13	-0.35	299
15<MLT<31 (Evening sector)	0.98	-0.31	-0.86	121
21<MLT<03 (Midnight sector)	0.91	-0.17	-0.73	29
All	1.36	-0.34	-0.66	520

Table 3.4 Summary of the relationship between A_p and T_{\perp} through the coefficients a and b of the relation $A_p = aT_{\perp}^b$ and the correlation coefficients R for different L regions.

L values	a	b	R	No. of events
$L < 6$	1.02	-0.30	-0.94	35
$6 < L < 7$	0.86	-0.26	-0.78	196
$L > 7$	1.32	-0.18	-0.43	289
All	1.36	-0.34	-0.66	520

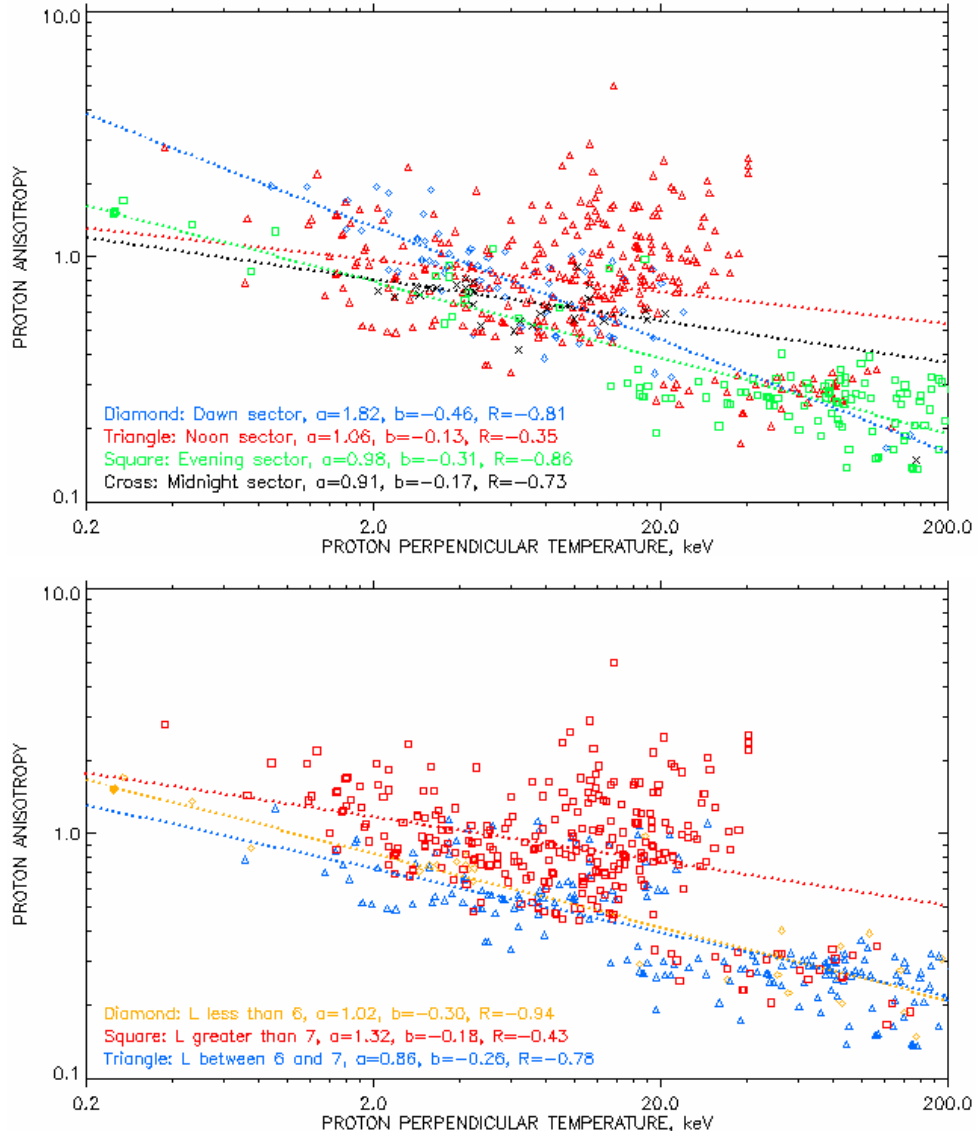


Figure 3.4 The upper panel shows a scatter plot of proton anisotropy versus proton perpendicular temperature with the data binned by MLT values and color-coded; the four dotted lines are the fitting curves for four different MLT sectors. The lower panel shows the same scatter plot as the upper panel, but the data are binned by L values; the three dotted lines are the fitting curves for three different L ranges.

3.5.3 Dependence of proton perpendicular temperature on wave normalized frequency

Each panel of Figure 3.5 shows a scatter plot of proton perpendicular temperature T_{\perp} versus wave peak normalized frequency X ; the data were also binned and color-coded in the same ways as those used in Figure 3.2. From either panel, we see that T_{\perp} decreases strongly with increasing X , approaching very small values when X is near to ~ 0.70 ; this is in agreement with the theoretical finding of *Gendrin et al.* [1971]. They used the kinetic theory, assumed a bi-Maxwellian distribution of hot protons with $T_{\perp} > T_{\parallel}$ and parallel propagation of EMIC waves, and found that for the range of A_p between 0.5 and 3.0 that is comparable with ours, EMIC waves can be amplified when X is between 0.2 and 0.7, see Figure 5 in their paper. Similarly, X for EIMC waves were observed in the range from 0.05 to 0.50 in the study of *Mauk and McPherron* [1980] using data from ATS-6. Because there is no theoretical basis for a functional form, we did not do a fit to the data, and thus there is no fitting curve in each panel of Figure 3.5.

From the upper panel of Figure 3.5, we see that the events in the dawn sector (blue diamonds) occur with X mainly from 0.2 to 0.6; those in the noon sector (red triangles) span nearly the observed range of X , from 0.1 to 0.7, but concentrate in the range between 0.27 and 0.55. It is clear that the events in the evening sector (green squares) concentrate at $X < 0.22$, and we see that those in the midnight sector (black crosses) have X falling in the narrow range between 0.27 and 0.40. The variation of X with MLT is in agreement with that found by *Anderson et al.* [1992b], see the top panel of Figure 8 in their paper.

From the lower panel of Figure 3.5, we see that the events in the region of L between 5.6 and 6 (brown diamonds) occur with $X < 0.58$. The events with L between 6 and 7 (blue triangles) cover mainly the range from ~ 0.10 to 0.46 while those with L between 7 and 8.1 (red squares) cover nearly the observed range X from ~ 0.1 to 0.7 and concentrate at high X . It appears that in general X increases with increasing L . This is consistent with the result of *Fraser and Nguyen* [2001], see Figure 8 in their paper.

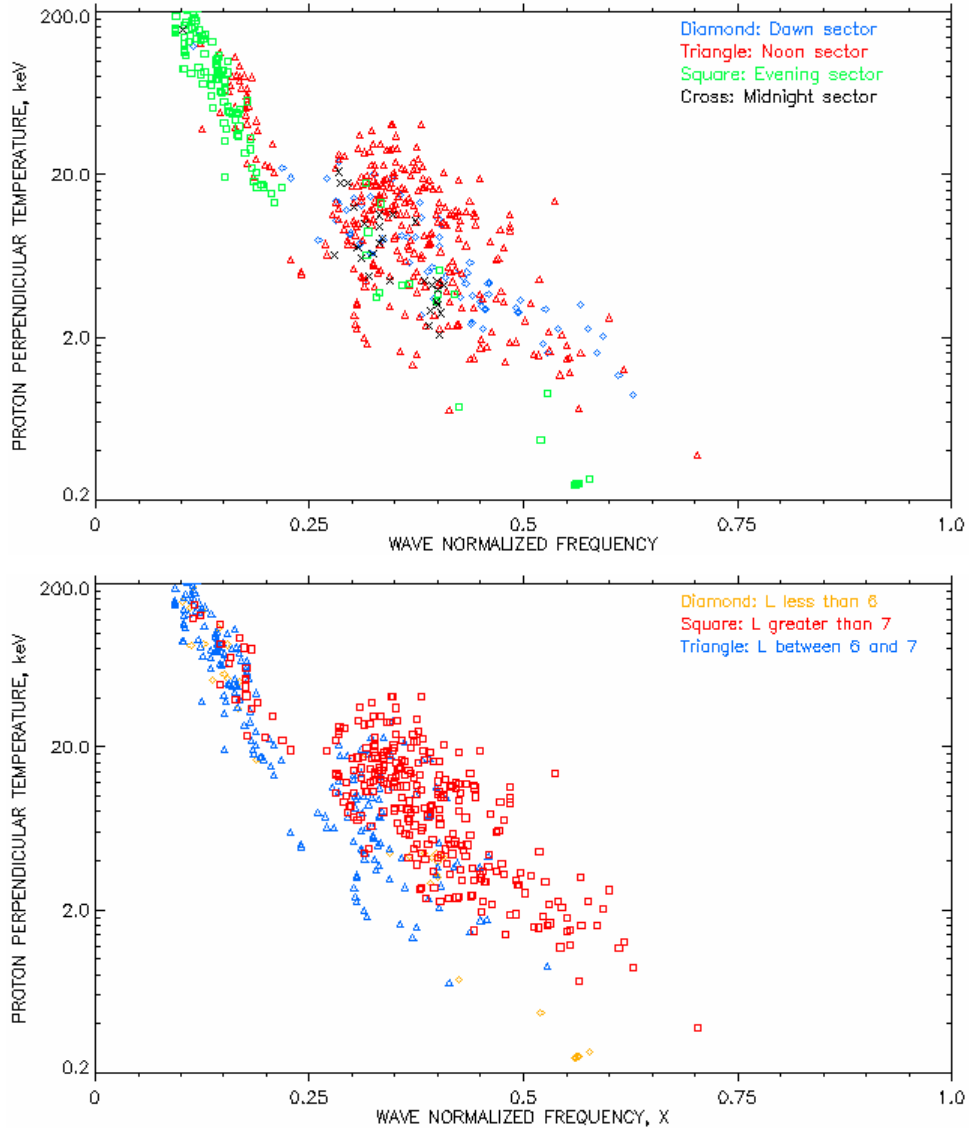


Figure 3.5 The upper panel shows a scatter plot of proton perpendicular temperature versus wave peak normalized frequency with the data binned by MLT values and color-coded. The lower panel shows the same scatter plot as the upper panel, but the data are binned by L values.

3.6 Conclusions

In summary, in this investigation, data from 59 days in 1986 obtained by the SCATHA satellite, have been analyzed to identify the electromagnetic ion cyclotron waves and to find the conditions under which the electromagnetic proton cyclotron instability acts as a generation mechanism for EMIC waves in the Earth's magnetosphere. Following the procedures outlined in Sections 3.2 and 3.3, we selected 520 two-minute interval events for analysis. These events occurred at all local time sectors, with L values from 5.6 to 8.1 and magnetic latitudes between -13.7° and 15.6° . The wave peak frequencies ranged from 0.13 to 1.08 Hz, i.e., ~ 0.1 to 0.7 normalized to the local proton cyclotron frequency. For each event, in the FAC system the values of P_{tran} are significantly greater than those of corresponding P_{para} , consistent with the transverse nature of the EMIC waves.

From this investigation several conclusions can be drawn:

1) There are several findings that are consistent with those of previous studies and/or with theoretical expectations. They include (a) the inverse correlation between proton temperature anisotropy and proton parallel beta and that the observed A_p are above the electromagnetic proton cyclotron instability thresholds, (b) that the observed waves actually get energy from energetic and anisotropic proton populations, and (c) that the peak normalized frequencies of the observed waves are less than 0.7 for the observed range of A_p .

2) Owing to the large number of events and the complete set of data accompanying each, we are able to study predicted theoretical relationships as a function of MLT

and L . We found that the inverse correlation $A_p = S_p \beta_{\parallel p}^{\alpha_p}$ holds not only for all events considered but also for those in different local time sectors and L ranges. More interestingly, we established a similar relation between A_p and T_{\perp} , given by Equation $A_p = a T_{\perp}^b$; this relation again applies for all events and for those in different MLT sectors and L ranges. The finding that the coefficients depend on macroscopic factors such as local time and L value reflects the degree of strength of external forces driving the energetic proton temperature anisotropy. We found the correlation coefficients R are greater than 0.6 for all MLT sectors and L ranges, except for the local noon sector and the region with L from 7 to 8.1.

3) The longitudinal or MLT variations are outstanding. The events in the dawn sector have rather high A_p , mainly low $\beta_{\parallel p}$, rather low T_{\perp} , and X mainly between 0.2 and 0.6. Those in the noon sector have mainly high A_p , mainly low $\beta_{\parallel p}$, low T_{\perp} , and X concentrating in the range between 0.27 and 0.55. Those in the evening sector have lowest A_p , highest $\beta_{\parallel p}$, highest T_{\perp} , and X concentrating at $X < 0.22$. Special results are found in the midnight sector; the events in this sector occur with limited ranges of A_p , $\beta_{\parallel p}$, and T_{\perp} , and with X just between 0.27 and 0.40.

4) The radial variations are also notable. We found that moving outward, or increasing L value, corresponds to increased A_p , in agreement with the drift shell splitting process, and also to lower $\beta_{\parallel p}$ and higher X .

CHAPTER 4

**OBSERVATIONS OF PROTON SCATTERINGS
BY EMIC WAVES IN THE MAGNETOSPHERE**

4.1 Introduction

As mentioned in Section 1.3, EMIC waves have been observed in the equatorial region of the Earth's magnetosphere, and these waves are believed to have the capability of pitch angle scattering trapped protons in the ring current or radiation belts. To our knowledge, however, there have not been in situ observations of proton pitch angle scattering by EMIC waves in the equatorial region of the magnetosphere other than a report by *Erlandson and Ukhorskiy* [2001] of simultaneous occurrences of EMIC waves and enhanced proton fluxes in the loss cone for $3.5 < L < 5$, indicating that EMIC waves indeed scattered protons into the loss cone. Taking advantage of the wealth of SCATHA satellite data, in this chapter we will show that under certain conditions EMIC waves scattered protons either away from or toward the magnetic field line.

4.2 Data preparation

Because there is one day on which we have no data on proton differential fluxes, in this investigation we use 58 days of SCATHA magnetic field and proton spectra data. Employing dynamic spectral analysis techniques described in Sections 2.3 and 2.4, for

each day we produced 24-hour dynamic displays of wave powers and ellipticity in the field-aligned coordinate (FAC) system. Inspection of these displays allows the identification of EMIC wave occurrences on that day. The occurrences of EMIC waves on each day considered are indicated by the enhancements on the corresponding dynamic display of wave transverse power. Then for the days identified with EMIC waves, those dynamic displays for any 2-hour interval during which EMIC waves occurred intermittently were generated, giving more details on the previously identified waves and their ellipticities along with other information such as UT, MLT, MLAT, and L value.

For investigating the relationship between EMIC waves and protons, the plots of proton differential fluxes, perpendicular and parallel to \mathbf{B}_0 , for 8 different energy bands (centered at 0.88, 2.06, 3.60, 8.80, 15.60, 36.00, 71.00, and 133.00 keV), versus universal time were also produced for the same two-hour intervals, just mentioned. Visual inspections of both wave dynamic displays and proton differential flux versus UT plots for these two-hour intervals were then performed to find time intervals during which both strong EMIC emission occurred and increases or decreases in proton differential fluxes were observed.

4.3 Observational results

As mentioned above, based on the 24-hour dynamic displays of wave powers and ellipticity, obtained by using data from the SCATHA satellite and dynamic spectral analysis techniques described in Sections 2.3 and 2.4, we identified 37 out of 58 days on which EMIC waves occurred intermittently. For the observed waves, the transverse

power was much greater than the parallel power, indicating the transverse nature of the EMIC waves.

By matching the plots of proton differential fluxes versus universal time and the dynamic displays of EMIC waves for the same two-hour intervals during which EMIC waves were found, we were able to identify 20 short time intervals showing correlations between EMIC waves and proton perpendicular differential fluxes j_{perp} in the energy bands centered at 15.6, 36.0, 71.0, and 133.0 keV. By correlation we mean that there is a sudden, strong increase (a peak) or strong decrease (a dip or a valley) in proton perpendicular differential flux, occurring simultaneously with the observed EMIC waves. Only events in which (1) the changes in proton perpendicular flux had the same time duration as that of the EMIC wave emissions, and (2) the peaks (or dips) were clearly above (or below) background and/or similar variations in that time frame were recorded. This procedure may have omitted some weak correlations as only those that were unambiguous were included. Each of these 20 intervals lasts only several minutes, and these intervals account for only approximately 3.5% of the total time of wave observation. Therefore they may be indicative of special conditions that require that the proton pitch angle populations are both anisotropic and non-gyrotropic, as explained later in Chapter 5. They were found in the magnetospheric region of L values from 5.6 to 7.5 and magnetic latitudes from -15.6° to 15.4° , mainly near local noon and in the evening sector.

For these 20 intervals, the wave frequencies fell in the range 0.16-1.06 Hz, which corresponded to 0.06-0.56 normalized to the local proton cyclotron frequency. Inspection of all spectra of these waves showed that the peak frequencies were either above or below

the local He^+ gyrofrequency, not both, and these waves had rather broad bands. This means that for these cases He^+ ions did not make a major contribution. Nineteen out of these 20 intervals had $\varepsilon < 0.0$, and only one had ε near 0.0. As mentioned in Section 1.4 and shown in Chapter 3, EMIC waves are expected to be generated in the left-hand mode by the electromagnetic proton cyclotron instability. While in the simple linear theory, EMIC waves propagating along the ambient magnetic field line are expected to be purely left-handed, i.e., $\varepsilon = -1$, this is not what is typically observed. Examples of the spread of ε of EMIC waves observed in the equatorial region of the magnetosphere can be found in the study of *Anderson et al.* [1992b], Figures 1, 6, 7, 8, and 9.

The summary of the observations of these intervals is given in Table 4.1. In this table, for each time interval, the date (day of year 1986), the middle values of UT, MLT, MLAT, L , and B_0 , the value of Dst (as an indication of the magnetic activity), the peak frequency of the observed waves, and the energy bands in which dips or peaks in j_{perp} were observed are given.

We found no correlations between EMIC waves and ‘lower energy’ (energy bands centered at 0.88, 2.06, 3.60, and 8.80 keV) proton differential fluxes either parallel or perpendicular to the ambient magnetic field. For ‘high energy’ (energy bands centered at 15.6, 36.0, 71.0, and 133.0 keV), we also found no correlations between proton parallel differential fluxes j_{para} and EMIC waves. This is despite the fact that EMIC waves are expected to scatter protons into the loss cone, as mentioned in Section 1.4. We think this is because j_{para} consists of protons with pitch angles between -30° and 30° , whereas the loss cone covers a much smaller pitch angle range.

The occurrences of strong peaks (dips) in j_{perp} during the same time intervals of EMIC wave existence can be attributed to the pitch angle scatterings of protons away from (toward) the local magnetic field line as a result of resonant interactions between those protons with the present EMIC waves. It should be noted that interaction with EMIC waves is not the only possible cause for the changes in proton perpendicular flux. For example, magnetic compressions are known to energize protons in the perpendicular direction [e.g., *Anderson and Hamilton, 1993; Arnoldy et al., 2005*]. In this investigation, however, we have found many EMIC wave periods together with increases or decreases in ambient magnetic field strength but with no changes in proton perpendicular flux.

Table 4.1 List of 20 time intervals during which correlations between EMIC waves and proton perpendicular differential fluxes were observed

Day	UT	MLT	MLAT(°)	L	f (Hz)	B_0 (nT)	Dst (nT)	Correlations (Peak/Dip in j_{perp} and centered energy, keV)
86037	14:15	8.56	15.42	7.47	1.06	124.3	-10	Peaks at 36 and 71
86037	22:48	14.75	6.84	7.03	0.54	94.46	-10	Peak at 133
86041	21:02	14.36	9.16	7.11	0.58	115.16	-130	Peaks at 36, 71 and 133
86045	14:16	10.49	13.89	7.51	0.57	95.61	-65	Peaks at 36, 71 and 133
86045 ^e	14:37	10.72	13.75	7.51	0.66	101.36	-65	Peaks at 36, 71 and 133
86048	21:32	16.87	7.246	6.64	0.2	109.40	-30	Peaks at 36, and 71
86051 ^e	12:24	10.48	11.25	7.38	0.7	107.73	-38	Dips at 36, 71, 133; Peak at 15.6
86054	12:30	11.18	8.65	7.28	0.8	93.63	-58	Dips at 71 and 133; Peak at 36
86054	14:23	12.50	8.20	7.26	0.49	91.87	-58	Peaks at 36, 71 and 133
86054	14:45	12.76	8.08	7.19	0.53	91.94	-58	Peaks at 36, 71 and 133
86054	19:44	17.09	4.90	6.46	0.28	95.34	-58	Dips at 71, 133; Peaks at 36, 15.6
86073*	6:31	10.87	-7.68	7.31	0.8	98.37	-50	Peaks at 36, 71 and 133
86073*	6:56	11.18	-7.83	7.28	0.74	99.66	-50	Peaks at 36, 71 and 133
86073* ^e	7:33	11.64	-8.07	7.22	0.58	105.17	-50	Dips at 36, 71 and 133
86077*	14:33	20.47	-13.66	5.9	0.16	177.72	-16	Dips at 36, 71 and 133
86080*	7:23	13.28	-13.18	6.98	0.92	149.83	-7	Peaks at 36, 71 and 133
86083 ^l	10:34	17.86	-15.6	6.15	0.16	175.52	-20	Dips at 36, 71 and 133
86086*	9:47	18.24	-14.77	6.04	0.23	171.45	-30	Peaks at 36, 71 and 133
86099	5:43	18.04	-6.7	5.78	0.22	128.66	-10	Dips at 71 and 133
86099	6:49	19.56	-4.20	5.65	0.22	147.52	-10	Dips at 71, 133; Peak at 36

*For days 073, 077, 080, 083, and 086, SCATHA proton differential flux data are available for the energy bands centered at 36, 71, and 133 keV only. The three intervals to be used as examples in this chapter are highlighted by the subscript ^{‘e’}. The interval at 10:34 UT, day 083, is the one with the wave ellipticities near 0, marked by the subscript ^{‘l’}.

4.4 Examples

4.4.1 Scattering of protons away from the local magnetic field

We consider an event in which protons are scattered away from \mathbf{B}_0 . From top to bottom of Figure 4.1, the first, second, third, and fourth panels show the plots of proton perpendicular differential fluxes (solid black lines) and proton parallel differential fluxes (dashed red lines), in the energy bands centered at 133.0, 71.0, 36.0, and 15.6 keV, versus universal time for two hours beginning at 13:00 UT, on day 045. The fifth shows the plot of magnetic field strength B_0 versus UT for the same time interval. The sixth and seventh show the dynamic displays of wave ellipticity and transverse power in the field-aligned coordinate system. The frequency-time (dynamic) displays of ellipticity include only ellipticity values where the wave transverse power exceeds a certain power threshold that is appropriate to the digitalization level of the instrument range, and a degree of polarization ≥ 0.7 . The dark horizontal bars at 1 Hz and 2 Hz on the wave power dynamic display and their corresponding counterparts on the wave ellipticity dynamic display are due to the satellite spin effects and are not real. The white solid line on the wave power dynamic display indicates the local He^+ gyrofrequency.

From the dynamic displays of ellipticity and transverse power, we see that during this 2-hour interval, EMIC waves occurred at 5 different UT intervals, lasting several

minutes. By matching them with the plots of proton differential fluxes versus UT also for this 2-hour interval (the first, second, third, and fourth panels from the top), we see that there are correlations between EMIC waves and j_{perp} in two intervals, one at 14:16 UT with a single peak in j_{perp} , marked by the left vertical line in Figure 4.1, and the other with a double peak in j_{perp} at 14:37 UT, marked by the right vertical line in Figure 4.1. These correlations occur in the energy bands centered at 36.0, 71.0, and 133.0 keV, but not at 15.6 keV. We see that the durations of the wave occurrences correspond well with those of the peaks in the observed j_{perp} .

There are some weak variations in proton perpendicular flux that occur with the strong EMIC emissions between 13:25-13:30, 14:45-14:50, and 14:55-15:00 UT. We did not classify these as correlations because for the former it is not clear that the time durations are the same, and the latter two lack the unambiguous rise of the event at 14:37 UT. The proton parallel fluxes are also plotted in Figure 4.1. They are small and do not show strong correlations with the observed EMIC waves. So they are also not classified as correlation events.

The correlation time interval that is centered at approximately 14:37 UT shows a double peak in j_{perp} , and the peak is stronger than that of the correlation interval at 14:16 UT. This may be due to the fact that the frequency bandwidth for the former is much broader than that for the latter.

We now consider in detail a two-minute wave event occurring at 14:36 UT, 10.72 MLT, $L=7.5$, MLAT=13.8°, day 045. The local magnetic field strength was $B_0=101$ nT (from the SCATHA Summary data). In Figure 4.2, the first, second, and third panels

show the plots of wave percent polarization, ellipticity, and powers versus frequency for the two minute; the fourth shows the plot of wave magnetic field amplitude $|\mathbf{B}_w|$ versus frequency for the same event. To generate the plots of wave percent polarization, ellipticity, and powers versus frequency for this two minute, we used the spectral analysis techniques described in Sections 2.3 and 2.4. To determine $|\mathbf{B}_w|$ we used the formula $|\mathbf{B}_w|=(P_{\text{tran}}\Delta f)^{1/2}$, where $\Delta f=0.017$ Hz is the frequency resolution; this formula is similar to that employed by *Anderson et al.* [1992a]. To eliminate the satellite spin effects at frequencies around 1 Hz and 2 Hz, we used the corresponding 2-min wave spectrum obtained in the GSM coordinate system. We found that P_{tran} spectra obtained in the GSM coordinate system showed no spin effects and had the same dependences of P_{tran} on frequency as those obtained in the FAC system, and the magnitudes of the two were different from one another by a nearly constant factor, whose value depends on the 2-min interval considered. Therefore, we obtained the values of P_{tran} in the FAC system at frequencies around 1 Hz and 2 Hz by using those in the GSM coordinate system for the same event and multiplying them by the approximate factor. From the third and second panels of Figure 4.2, we see that at frequencies with strong EMIC waves the transverse power is at least an order of magnitude larger than the parallel power and mainly $\epsilon < 0.0$; the waves were thus mainly left-hand polarized.

The change of the proton populations relating to the event shown in this example is illustrated in Figure 4.3. The upper and lower panels of this figure show the plots of the observed j_{perp} and j_{para} versus proton energy for one-minute interval at three different instants. The dashed lines show the dependences of the observed j_{perp} and j_{para} on proton

energy at the event occurrence instant (14:37 UT, day 045); the dotted lines show those at 14:31 UT, six minutes before the event occurs; and the dot-dashed lines show those at 14:43 UT, six minutes after the event. Comparing the observed j_{perp} and j_{para} at each instant, we see that at all three instants the j_{perp} are clearly greater than their counterpart j_{para} for high energies. Thus the three corresponding populations are anisotropic with $T_{\perp} > T_{\parallel}$. The significant increases in the observed j_{perp} in the energy bands centered at 36, 71, and 133 keV (see the upper panel of Figure 4.3) are clear. This, however, does not lead to as large a change in the counterpart j_{para} , as clearly seen in the lower panel of Figure 4.3.

The sudden increases in j_{perp} occurring at the same time as the existence of EMIC waves indicate that protons in the corresponding energy bands were pitch angle scattered away from the local magnetic field due to the interactions with these waves. Explanations for these scatterings will be given in Section 5.5.1, Chapter 5.

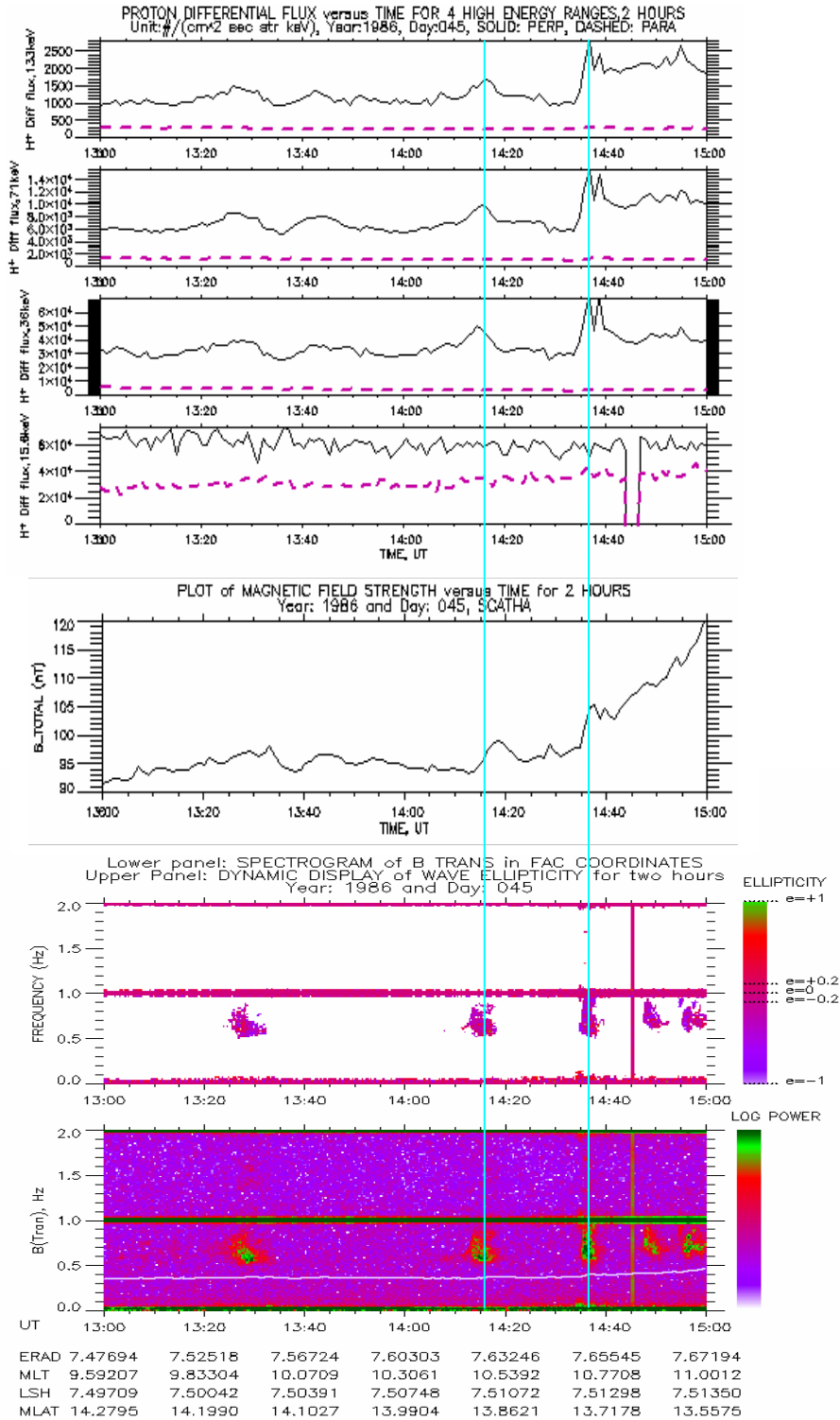


Figure 4.1 The first, second, third, and fourth panels from the top show the plots of j_{perp} (solid black lines) and j_{para} (dashed red lines), centered at 133.0, 71.0, 36.0, and 15.6 keV, versus UT for 2 hours beginning at 13:00 UT, day 045; the fifth shows the plot of B_0 versus UT; the sixth and the seventh show the dynamic displays of wave ellipticity and transverse power. The white solid line on the seventh panel indicates the local He^+ gyrofrequency.

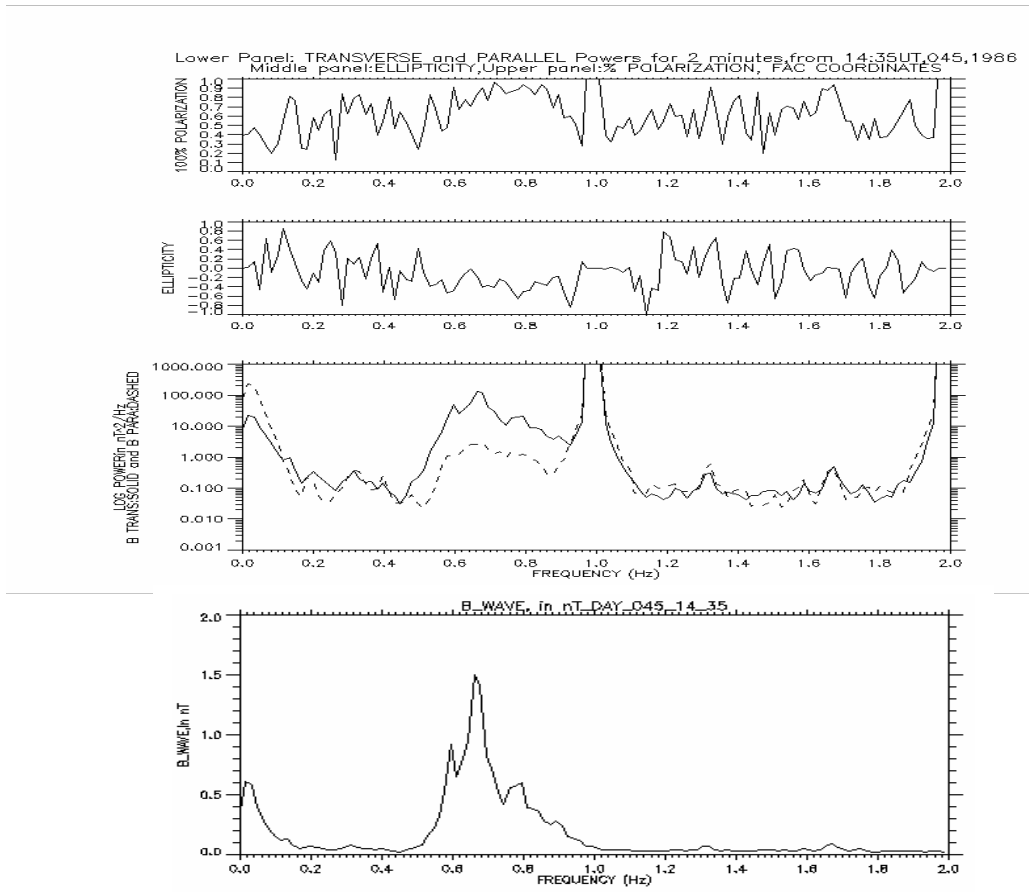


Figure 4.2 From top to bottom, the first, second, and third panels show the plots of wave percent polarization, ellipticity, and powers versus frequency for the 2-minute interval beginning at 14:35 UT, day 045; the fourth shows the plot of wave magnetic field amplitude versus frequency for this event.

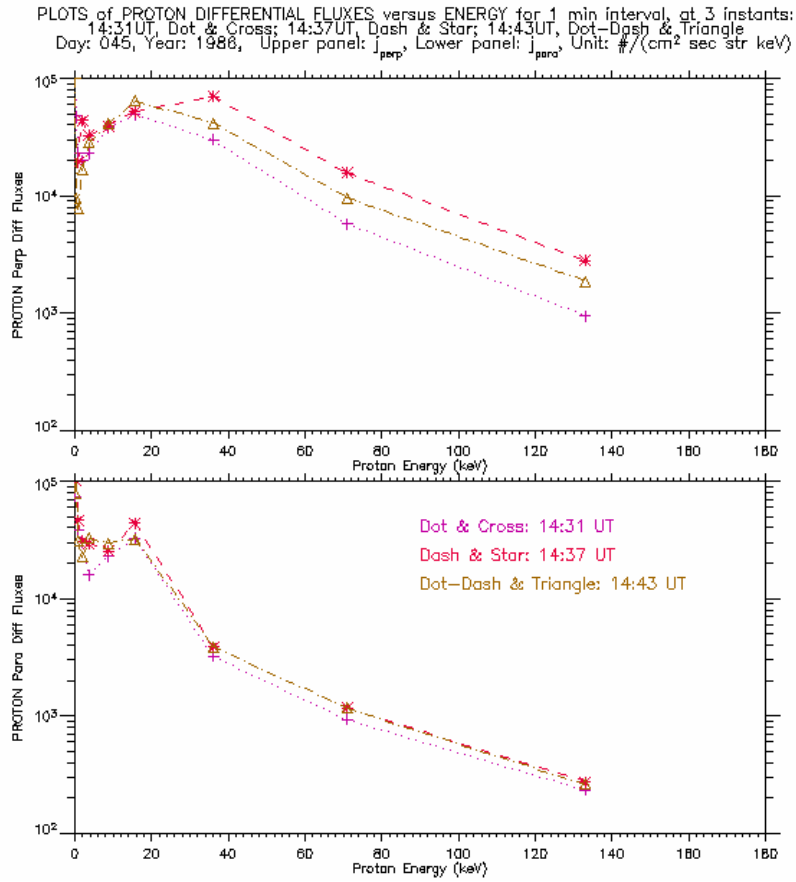


Figure 4.3 The upper and lower panels show the plots of the observed j_{perp} and j_{para} versus proton energy for one-minute interval at three different instants. The dashed lines are the plots at the event occurrence instant (14:37 UT, day 045); the dotted lines are those at 14:31 UT, six minutes before the event occurs; and the dot-dashed lines are those at 14:43 UT, six minutes after the event.

4.4.2 Scattering of protons toward the local magnetic field

We now consider an event in which protons are scattered toward \mathbf{B}_0 . Figure 4.4 has the same format as Figure 4.1 for two hours beginning at 06:00 UT, on day 073; except that there are no plots of proton differential fluxes in the energy band centered at 15.6 keV because no SCATHA data on j_{perp} and j_{para} are available in this energy band for this time.

From Figure 4.4 (the fifth and sixth panels from the top), we see that during this 2-hour interval EMIC waves occurred at 4 different time intervals, lasting several minutes. By matching them with the plots of proton differential fluxes versus UT also for this 2-hour interval (the first, second, and third panels from the top), we see that there are correlations between EMIC waves and proton perpendicular differential fluxes j_{perp} in three intervals at 06:32 UT, 06:56 UT, and 07:33 UT, marked by three corresponding vertical lines in this figure. The correlations at 06:32 UT and 06:56 UT are indicated by the sudden increases (peaks) in the observed j_{perp} , and the one at 07:33 UT by sudden decreases (dips) in the observed j_{perp} , in the energy bands centered at 36, 71, and 133 keV. We again see that the durations of the wave occurrence also correspond well with those of the peaks or dips in the observed j_{perp} .

There are weak EMIC emissions and fluctuations in j_{perp} between 7:10 and 7:18 UT. But these peaks and dips are typical of those seen throughout this two-hour period and are not classified as correlation events. There is also a time period near 6:40 UT in which the proton perpendicular fluxes are very low, but this is between two peaks and not during a period of strong EMIC waves. So it is not classified as a correlation event either.

The proton parallel fluxes are again much weaker than the perpendicular fluxes and show no significant variations so we do not include any of these as correlation events.

We focus on the correlation interval, marked by the rightmost vertical line in Figure 4.4, which occurred at 07:33 UT, 11.64 MLT, $L=7.2$, $MLAT=-8.07^\circ$. Figure 4.5 has the same format as Figure 4.2 for the 2-minute interval from 07:32 to 07:34 UT, day 073. The local magnetic field strength was $B_0=105$ nT. From the third and second panels of Figure 4.5, we again see that at frequencies with strong EMIC waves the transverse power is at least an order of magnitude larger than the parallel power and $\epsilon < 0.0$; the waves were thus left-hand polarized.

Because for this time interval the measurements of j_{perp} and j_{para} in the energy bands centered at 15.6, 8.80, 3.60, 2.06, and 0.88 keV are not included in the SACTHA data available to us, we do not produce plots similar to those in Figure 4.3 for the event shown in this example. We, however, also found that the sudden decreases in the observed j_{perp} in the 36, 71, and 133 keV bands do not lead to sudden increases in the counterpart j_{para} .

The sudden decreases in j_{perp} occurring at the same time as the existence of EMIC waves indicate that protons in the corresponding energy bands were pitch angle scattered toward the local magnetic field due to the interactions with these waves. Explanations for these scatterings will be given in Section 5.5.2, Chapter 5.

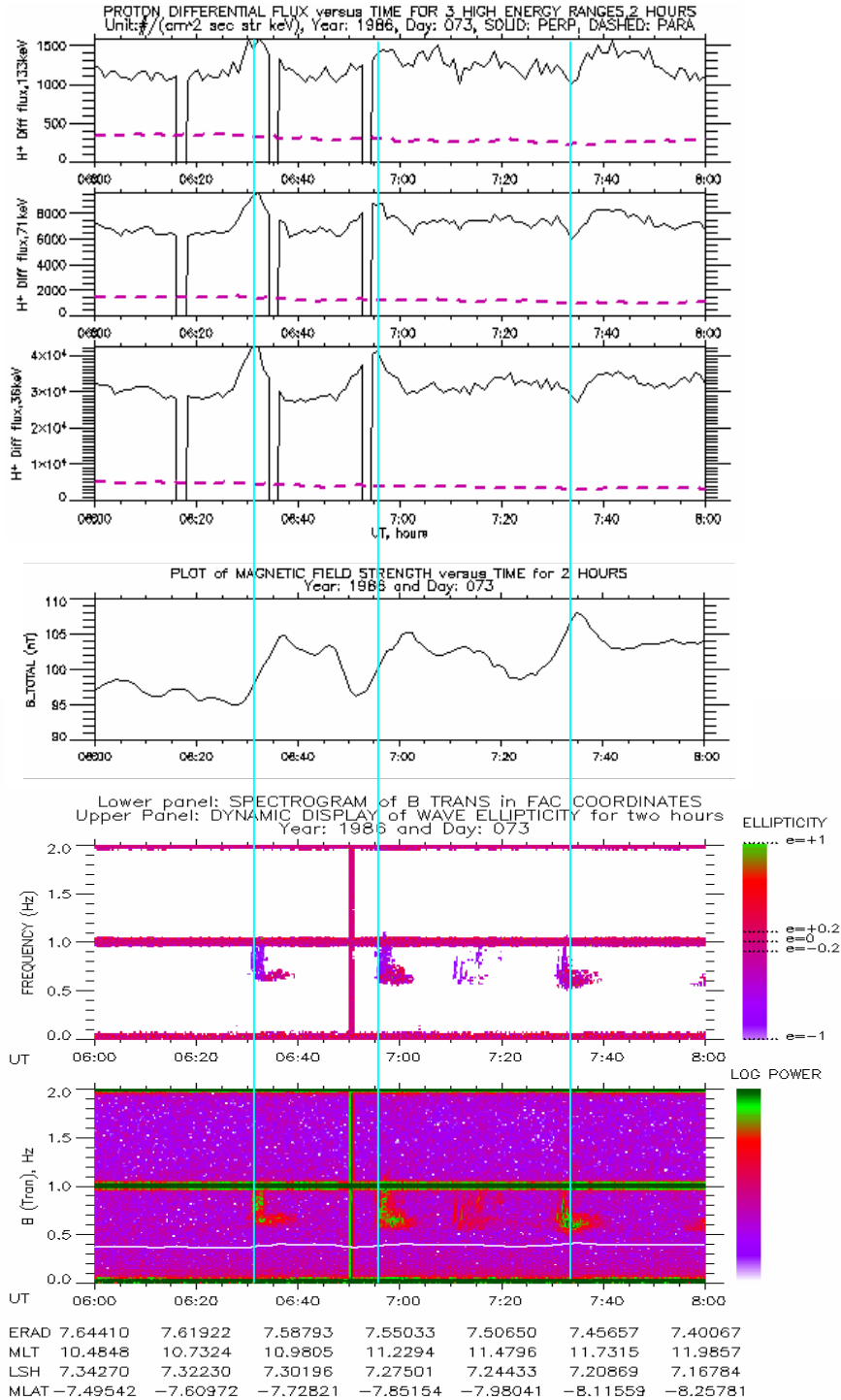


Figure 4.4 From top to bottom, the first, second, and third panels show the plots of j_{perp} (solid black lines) and j_{para} (dashed red lines), centered at 133, 71, and 36 keV, versus UT for 2 hours beginning at 06:00 UT, day 073; the fourth shows the plot of B_0 versus UT; the fifth and the sixth show the dynamic displays of wave ellipticity and transverse power.

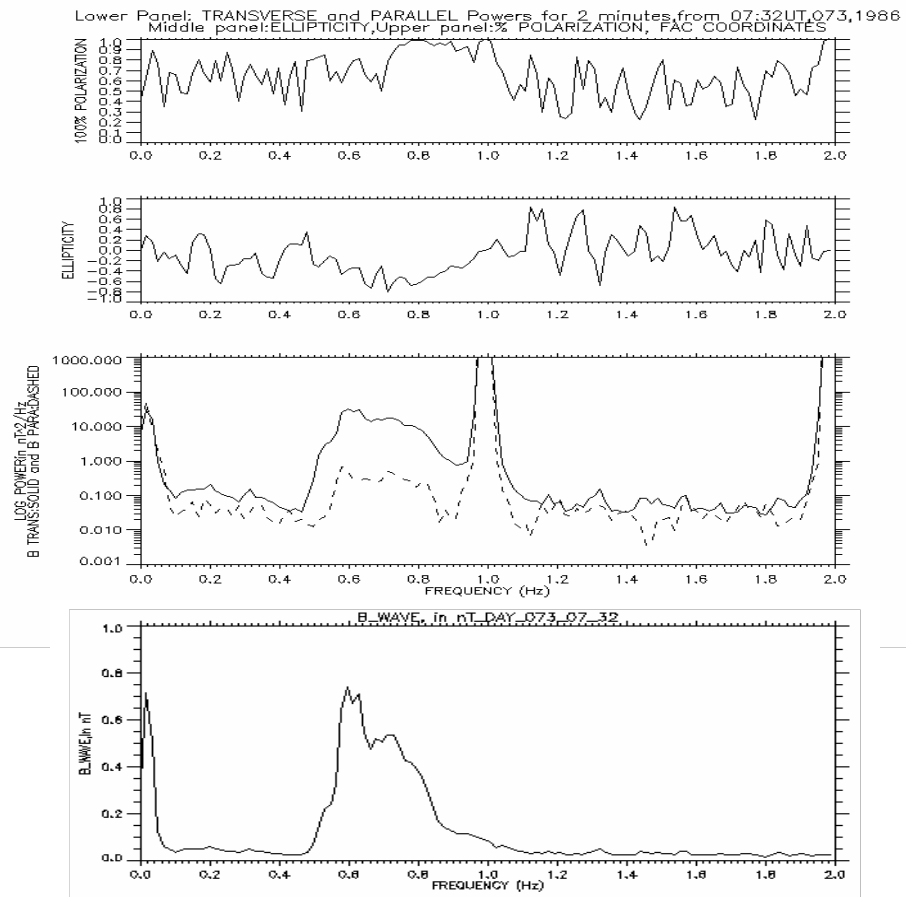


Figure 4.5 The same format as Figure 4.2 for the 2-minute interval from 07:32 UT, day 073.

4.4.3 Scattering of protons toward and away from the local magnetic field

We now consider an event in which a peak in one energy band and dips in other energies bands in j_{perp} were observed. Figure 4.6 has the same format as Figure 4.1 for two hours beginning at 11:00 UT, on day 051. From the sixth and seventh panels of this figure, we see that during this 2-hour interval EMIC waves occurred at 4 different time intervals, lasting several minutes. By matching them with the plots of proton differential fluxes versus UT also for this 2-hour interval (the first, second, third, and fourth panels from the top), we see that there are correlations between EMIC waves and proton perpendicular differential fluxes j_{perp} in one interval at 12:24 UT, marked by a vertical line in this figure. These correlations are indicated by sudden decreases (dips) in j_{perp} in the energy bands centered at 36.0, 71.0, and 133.0 keV and a sudden increase (peak) in j_{perp} in the energy band centered at 15.6 keV. We see that the duration of the wave occurrence corresponds well with those of the peak and dips in the observed j_{perp} .

There is a period of strong EMIC wave emission from 11:50 to 11:55 UT. But there are no significant changes in j_{perp} , so we do not classify this as a correlation event. The parallel fluxes are again smaller than the perpendicular fluxes. They do show variations but no unambiguous correlation with the EMIC waves.

We concentrate on the two-minute wave event occurring at 12:24 UT, 10.48 MLT, $L=7.4$, and $\text{MLAT}=11.25^\circ$ with $B_0=108$ nT, as shown in Figure 4.7. Figure 4.7 has the same format as Figure 2 for this two minute. From the third and second panels of this figure, we also see that at frequencies with strong EMIC waves the transverse power is at

least an order of magnitude larger than the parallel power and mainly $\varepsilon < 0.0$; the waves were thus mainly left-hand polarized.

The change of the proton populations relating to the event shown in this example is illustrated in Figure 4.8. Similarly to Figure 4.3, the dashed lines in both panels of Figure 4.8 show the dependences of the observed j_{perp} and j_{para} on proton energy at the event occurrence instant (12:24 UT, day 051); the dotted lines show those at 12:19 UT, five minutes before the event occurs; and the dot-dashed lines show those at 12:29 UT, five minutes after the event. Comparing the observed j_{perp} and j_{para} at each instant, we see again that at all three instants the j_{perp} are greater than the counterpart j_{para} for all energy bands. Thus the three corresponding populations are also anisotropic with $T_{\perp} > T_{\parallel}$. The presence of the EMIC waves at 12:24 UT clearly causes a significant increase in the observed j_{perp} in the energy band centered at 15.6 keV and significant decreases in the observed j_{perp} in the energy bands centered at 36, 73, and 133 keV (see the upper panel of Figure 4.8). The sudden increase/decreases in j_{perp} , however, do not lead to sudden decrease/increases in j_{para} , as clearly seen in the lower panel of Figure 4.8.

The sudden decreases and increase in j_{perp} occurring at the same time as the existence of EMIC waves indicate that protons in the corresponding energy bands were pitch angle scattered toward (for the bands centered at 36.0, 71.0, and 133.0 keV) and away from (for the band centered at 15.6 keV) the local magnetic field due to the interactions with these waves. Explanations for these scatterings will be given in Section 5.5.3, Chapter 5.

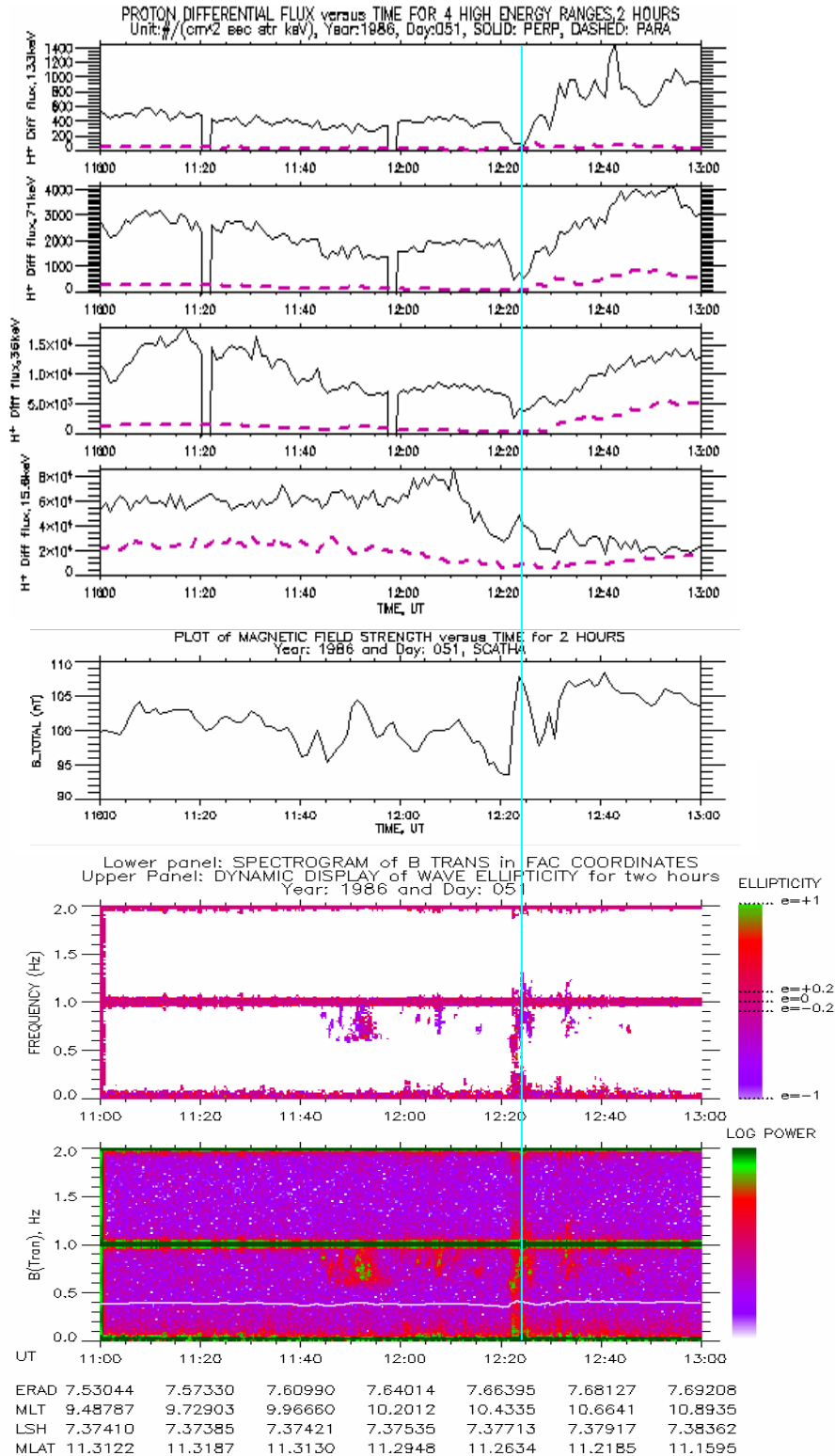


Figure 4.6 The same format as Figure 4.1 for two hours beginning at 11:00 UT, day 051.

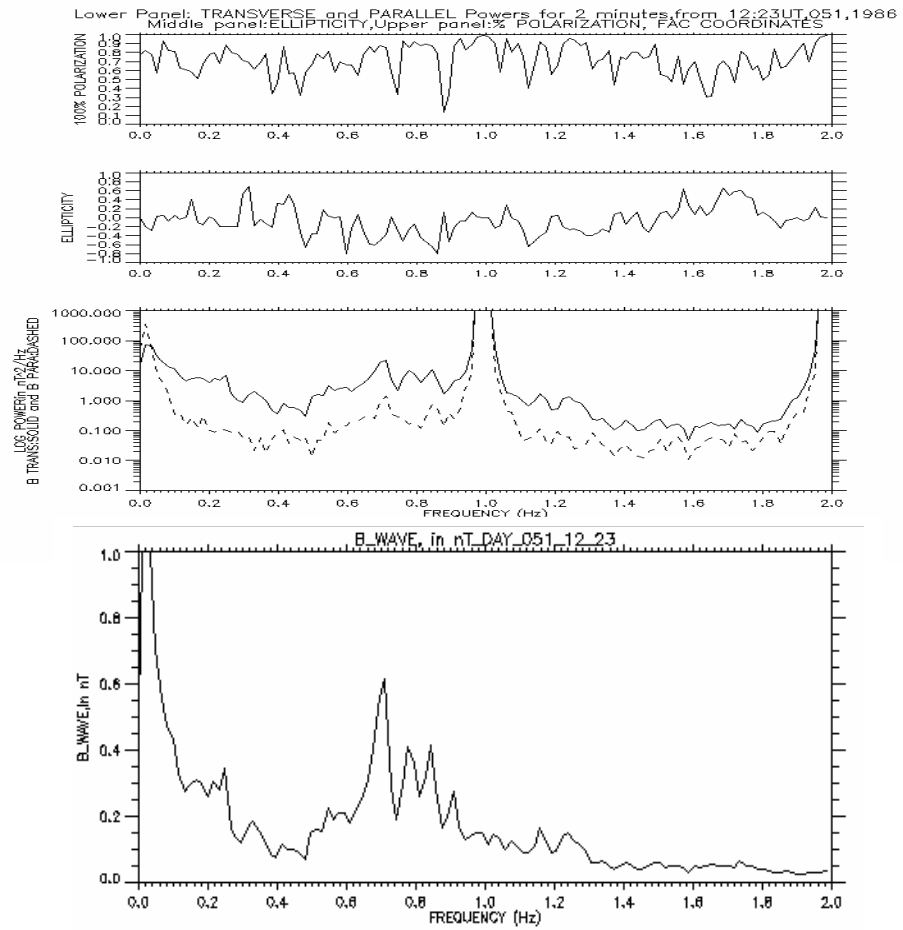


Figure 4.7 The same format as Figure 4.2 for the 2-minute interval from 12:23 UT, day 051.

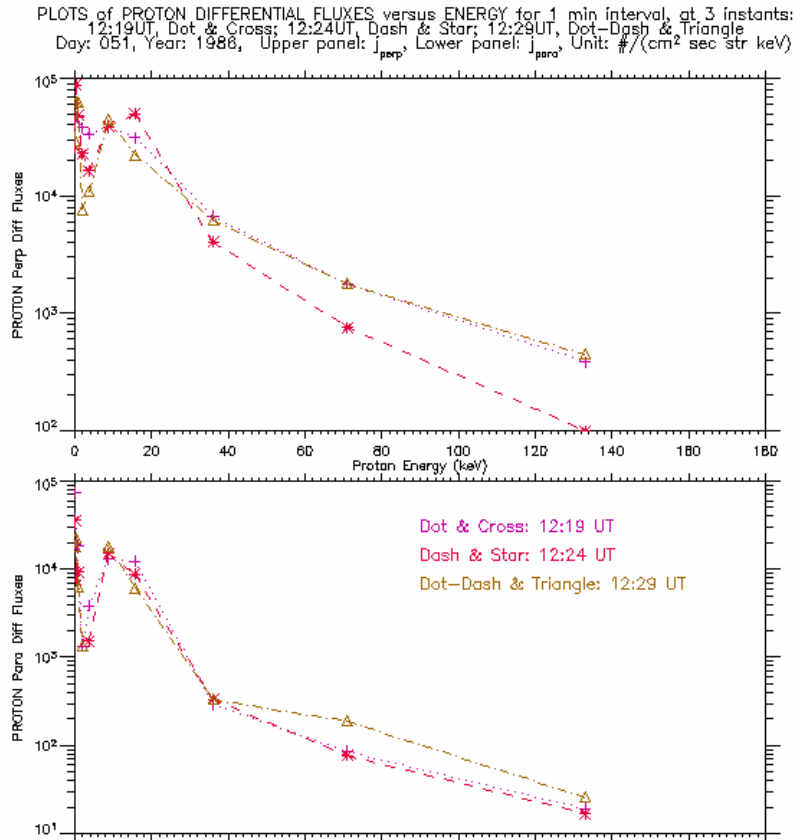


Figure 4.8 The upper and lower panels show the plots of the observed j_{perp} and j_{para} versus proton energy for one-minute interval at three different instants. The dashed lines are the plots at the event occurrence instant (12:24 UT, day 051); the dotted lines are those at 12:19 UT, five minutes before the event occurs; and the dot-dashed lines are those at 12:29 UT, five minutes after the event.

4.5 Summary

Using the SCATHA data and dynamic spectral techniques, we found that EMIC waves occurred intermittently on 37 out of 58 days considered and there were 20 time intervals showing correlations between EMIC waves and proton perpendicular differential fluxes. Each of these 20 intervals lasted only a few minutes. They were mainly near local noon and in the evening sector with L values from 5.6 to 7.5 and magnetic latitudes within 15 degrees of the equator. The wave frequencies fell in the range 0.16-1.06 Hz, which corresponds to 0.06-0.56 normalized to the local proton gyro-frequency. Although these intervals account for approximately 3.5% of the total time of wave observation, they indicate that EMIC waves indeed pitch angle scatter protons either toward or away from the local magnetic field. In the next chapter we will consider a mechanism for this scattering and give explanations for the examples given in this chapter.

CHAPTER 5
A THEORETICAL MODEL FOR SCATTERING
OF PROTONS BY EMIC WAVES

5.1 Introduction

As shown in Chapter 4, we have found that in a small percentage of the time intervals in which EMIC wave emissions were observed by SCATHA, there are correlations with the proton perpendicular differential fluxes j_{perp} . They indicate that EMIC waves indeed pitch angle scatter protons either toward or away from the local magnetic field, \mathbf{B}_0 . In this chapter we present a linear analysis of the interactions of protons with the observed spectrum of EMIC waves that suggests that it is reasonable to attribute the changes in j_{perp} to resonant interactions with the EMIC waves if the proton pitch angle distribution is non-gyrotropic or exhibits gyrophase bunching in these unusual cases. These interactions result in pitch angle scatterings of protons with respect to \mathbf{B}_0 .

5.2 Cyclotron resonance between EMIC wave and proton

Cyclotron (or gyro) resonance is the term used in a process in which the wave electric field vector of a circularly polarized wave and a particle both rotate about a magnetic field line at the same frequency and can exchange energy between one and the other. Consider a proton with a finite perpendicular velocity, spiraling along the local

ambient magnetic field \mathbf{B}_0 and an EMIC wave propagating parallel to \mathbf{B}_0 , but in the direction opposite to that of the proton. If the Doppler-shifted wave frequency is equal to the local proton gyrofrequency, the wave and proton are in cyclotron resonance. When this happens, the wave electric field vector \mathbf{E}_w and \mathbf{v}_\perp of the proton maintain a constant phase angle with respect to each other, allowing \mathbf{E}_w and \mathbf{B}_w , which is the wave magnetic field vector, to exert forces on the proton for a reasonable time interval, leading to energy transfer [e.g., *Brice*, 1964].

5.3 Theoretical model for scattering of protons by EMIC waves

For a proton to interact resonantly with an EMIC wave with angular frequency, ω , the following condition must be satisfied [e.g., *Kennel and Engelmann*, 1966]

$$\omega - k_{\parallel} v_{\parallel R} = m \Omega_p \quad (5.1)$$

where $m=0, \pm 1, \pm 2, \pm 3, \dots$, and $\Omega_p = qB_0/m_p$ is the proton cyclotron angular frequency, k_{\parallel} the component parallel to \mathbf{B}_0 of the wave vector \mathbf{k} , $v_{\parallel R}$ the component parallel to \mathbf{B}_0 of the resonant proton's velocity, q the proton electric charge, and m_p the proton mass. The values $m \neq 0$ give cyclotron harmonic resonances where the wave angular frequency in the particle's frame of reference is equal to some harmonic of the particle's cyclotron angular frequency. The value $m=1$ gives the principal harmonic resonance.

According to *Kennel and Petschek* [1966] and *Ginet and Albert* [1991], for the values of m in Equation (5.1) such that $|m| > 1$ the wave must propagate at an angle ($A \neq 0^\circ$)

with respect to \mathbf{B}_0 . Therefore, for EMIC waves propagating parallel to \mathbf{B}_0 and for the analysis presented in this chapter, the value $m=1$ is assumed. According to *Somov* [2000], the strongest interaction usually occurs when the Doppler-shifted wave frequency exactly matches the particle gyrofrequency. Substituting $m=1$ into Equation (5.1) leads to (for parallel propagation we set $k_{\parallel}=k$)

$$v_{\parallel R} = \frac{\omega - \Omega_p}{k} \quad (5.2)$$

For an EMIC wave with $0 < \omega < \Omega_p$, from Equation (5.2) we can see that the product, $k v_{\parallel R}$, must be negative, and thus the parallel velocity of the resonant proton must be opposite to the wave phase velocity [e.g., *Helliwell*, 1970]. From Equation (5.2) we easily see that if v_{\parallel} of the interacting proton changes, the current resonance condition is broken. For a strong interaction between the particle and the wave to continue, the particle must resonate with a different frequency in the emission spectrum, establishing a new resonance condition.

Since the observed EMIC waves are traveling at small angle with respect to \mathbf{B}_0 , we will treat the case of parallel propagation. Then the wave electric field vector \mathbf{E}_w is perpendicular to \mathbf{B}_0 and corotating with respect to the gyromotion of the proton that is also spiraling along \mathbf{B}_0 . The corotation angle or relative phase angle, θ_c , is defined as the angle between \mathbf{v}_{\perp} of the proton and \mathbf{E}_w such that $\theta_c = \cos^{-1}(\mathbf{v}_{\perp} \cdot \mathbf{E}_w / (v_{\perp} |\mathbf{E}_w|))$, where \mathbf{v}_{\perp} is the vector component perpendicular to \mathbf{B}_0 of the proton's velocity.

As mentioned earlier, for the energy transfer between the wave and the proton to be efficient, the particle and the wave must maintain the same phase relation for a sufficient period of time [e.g., *Hargreaves*, 1979], so that the proton in resonance sees the wave fields \mathbf{E}_w and \mathbf{B}_w as static ones. The wave electric force acting on the proton is $q\mathbf{E}_w$ and in the perpendicular direction. The wave magnetic force acting on the proton is $q(\mathbf{v}\times\mathbf{B}_w)=q(\mathbf{v}_{\parallel}\times\mathbf{B}_w)+q(\mathbf{v}_{\perp}\times\mathbf{B}_w)$. The sign ‘x’ here denotes the cross product of two vectors. We have used $\mathbf{v}=\mathbf{v}_{\parallel}+\mathbf{v}_{\perp}$.

Because \mathbf{E}_w and \mathbf{B}_w are both perpendicular to \mathbf{B}_0 , and the wave propagates along \mathbf{B}_0 , opposite to the spiraling proton (\mathbf{v}_{\parallel} and \mathbf{k} are antiparallel while the resonance condition holds), and the three vectors, \mathbf{E}_w , \mathbf{B}_w , and \mathbf{k} , make a right-handed system, we can see that $q(\mathbf{v}_{\parallel}\times\mathbf{B}_w)$ is always parallel to \mathbf{E}_w . As a result, the total force due to the wave acting on the proton in the perpendicular direction is $q(\mathbf{E}_w+\mathbf{v}_{\parallel}\times\mathbf{B}_w)$ and the equation of motion of the proton in the perpendicular direction is

$$m_p \frac{dv_{\perp}}{dt} = q|\mathbf{E}_w + \mathbf{v}_{\parallel}\times\mathbf{B}_w| \cos \theta_c \quad (5.3)$$

or

$$\frac{dv_{\perp}}{dt} = \frac{q}{m_p} (v_{\parallel} - v_{\text{phase}}) |\mathbf{B}_w| \cos \theta_c \quad (5.4)$$

where $|\mathbf{B}_w|$ is the amplitude of the wave magnetic field. We have used $|v_{\text{phase}}| = |\mathbf{E}_w|/|\mathbf{B}_w|$, where v_{phase} is the wave phase velocity.

The vector component $q(\mathbf{v}_\perp \times \mathbf{B}_w)$ acts on the proton in the parallel direction, leading to the equation of motion of the proton in this direction

$$\frac{dv_\parallel}{dt} = -\frac{q}{m_p} v_\perp |\mathbf{B}_w| \cos \theta_c \quad (5.5)$$

If we multiply both sides of Equation (5.4) by $v_\perp dt$ and both sides of Equation (5.5) by $(v_\parallel - v_{\text{phase}}) dt$ and then add the results together, we obtain

$$v_\perp dv_\perp + (v_\parallel - v_{\text{phase}}) dv_\parallel = 0 \quad (5.6)$$

Integrating both sides of Equation (5.6) leads to [Brice, 1964]

$$v_\perp^2 + (v_\parallel - v_{\text{phase}})^2 = \text{constant} \quad (5.7)$$

Multiplying both sides of Equation (5.7) by $m_p/2$, the left hand side becomes the proton energy in the rest frame of the wave. Thus in this frame the energy of the particle is constant so that if v_\parallel increases (decreases), v_\perp decreases (increases), and the particle pitch angle decreases (increases).

For an EMIC wave propagating parallel to \mathbf{B}_0 in a pure proton plasma, we have the following approximate dispersion relation [e.g., Lyons and Williams, 1984; Baumjohann and Treumann, 1996; Boyd and Sanderson, 2003]

$$\omega^2 = k^2 v_A^2 \left(1 - \frac{\omega}{\Omega_p}\right) \quad (5.8)$$

where $v_A = B_0 (\mu_0 m_p n)^{-1/2}$ is the local Alfvén velocity and n the local total electron number density. From Equation (5.8) we have

$$|k| = \frac{\omega}{v_A \left(1 - \frac{\omega}{\Omega_p}\right)^{1/2}} \quad (5.9)$$

Combining Equations (5.2) and (5.9) leads to

$$v_{\text{IR}} = v_A \left(\frac{\Omega_p}{\omega} - 1\right) \left(1 - \frac{\omega}{\Omega_p}\right)^{1/2} \quad (5.10)$$

and from Equation (5.9) and $|v_{\text{phase}}| = \omega / |k|$, we have

$$|v_{\text{phase}}| = v_A \left(1 - \frac{\omega}{\Omega_p}\right)^{1/2} \quad (5.11)$$

Now combining Equations (5.4), (5.10), and (5.11) yields

$$\frac{dv_{\perp}}{dt} = v_A \frac{q}{m_p} |\mathbf{B}_w| \left(\frac{\Omega_p}{\omega} \right) \left(1 - \frac{\omega}{\Omega_p} \right)^{1/2} \cos \theta_c \quad (5.12)$$

while the resonance condition holds. So that all the terms on the right hand side of Equation (5.12) are available from the SCATHA data except the Alfvén velocity. To estimate the Alfvén velocity v_A , we assume charge neutrality and use the empirical models, as described in Section 3.3.2, for the local cold electron number density n because values of n were not included in the SCATHA data.

5.4 Pitch angle scattering of protons by EMIC waves

Assuming a value of relative phase angle between the wave electric field and the gyro-motion of the proton and that the proton stays in resonance as its parallel velocity changes by interacting with the observed strength of the waves at new resonant frequencies, we now solve the equations of motion for the particle, i.e., Equations (5.5) and (5.12). We then obtain v_{\parallel} , v_{\perp} , α , and E of the proton as functions of time over the period during which the resonant interaction is maintained, i.e., t_{interact} . Here α is the proton pitch angle given by

$$\tan \alpha = \frac{v_{\perp}}{v_{\parallel}} \quad (5.13)$$

and E is the total energy of the interacting proton. Note that during the interacting period, Equation (5.10) is always met, meaning the proton and the wave are always in resonance.

While v_{\parallel} changes, the proton interacts resonantly with other waves with different frequencies in the spectrum, such that Equation (5.10) is satisfied.

We consider two cases. In the first case, for the relative phase angle θ_c is an acute angle such that $0 \leq |\theta_c| < \pi/2$ and $\cos \theta_c > 0$, solutions to Equations (5.5) and (5.12) show that v_{\parallel} decreases and v_{\perp} increases, i.e., α increases over time, and the particle is pitch angle scattered away from \mathbf{B}_0 . In this case the effect of perpendicular acceleration on the proton energy is greater than that of parallel deceleration so E also increases. Such a particle increases its pitch angle and energy so that it appears in one of the perpendicular differential flux bands observed by SCATHA. If more particles are scattered into a particular band than out of the band, a peak in j_{perp} will be observed in that band as a result of the resonant interactions of the protons with the EMIC waves.

In the second case, for the relative phase angle θ_c is an obtuse angle such that $\pi/2 < |\theta_c| \leq \pi$ and $\cos \theta_c < 0$, solutions to Equations (5.5) and (5.12) show that v_{\parallel} increases and v_{\perp} decreases, i.e., α decreases over time, and the particle is pitch angle scattered toward \mathbf{B}_0 . In this case the effect of perpendicular deceleration on the proton energy is greater than that of parallel acceleration so E also decreases. If more particles are scattered out of a particular band than into that band, a dip in the proton perpendicular differential flux in that band is observed.

In the interaction region, individual protons respond to the waves. Protons whose parallel velocities satisfy Equation (5.10) interact strongly with the waves. The waves can get energy from the protons leaving the proton distribution less anisotropic, and the j_{perp} decreases; or the protons can get energy from the waves, and the j_{perp} increases. For a

whole distribution of interacting protons in the Earth's radiation belts or ring current region, the two processes can occur simultaneously and compete with each other. One expects to observe correlations between EMIC wave occurrences and proton perpendicular differential fluxes only when the plasma conditions are favorable, i.e., when

a) a significant amount of protons in the interaction region interact resonantly with the EMIC waves, and

b) the number of resonant protons whose relative phase angles satisfy $0 \leq |\theta_c| < \pi/2$ is significantly different from that of resonant protons whose relative phase angles satisfy $\pi/2 < |\theta_c| \leq \pi$.

We thus see that the effects of resonant interactions depend very much on the values of gyrophase of the individual protons of the interacting population. If the gyrophases of the interacting protons are initially distributed in a random fashion, i.e., without any preferences in the azimuthal direction in the plane perpendicular to \mathbf{B}_0 , the values of the relative phase angles $|\theta_c|$ will be equally distributed between 0 and π , and the number of protons that are pitch angle scattered away from \mathbf{B}_0 will not be significantly different from that of protons that are pitch angle scattered toward \mathbf{B}_0 , and the net result will lead to no significant increases or decreases in j_{perp} . As mentioned in Chapter 4, the 20 time intervals of correlation account for only about 3.5% of the total time of wave observation and may be indicative of special conditions. It appears that the gyrophases of the interacting protons are initially so distributed that the number of protons with $|\theta_c| < \pi/2$ is significantly greater than that of those with $|\theta_c| > \pi/2$ in the case of observations of sudden increases or peaks in j_{perp} , and the number of protons with $|\theta_c| < \pi/2$ is significantly smaller

than that of those with $|\theta_c| > \pi/2$ in the case of observations of sudden decreases or dips in j_{perp} . In other words, the pitch angle distributions of interacting proton populations are non-gyrotropic or exhibit phase bunching.

5.5 Explanations for the examples in Chapter 4

5.5.1 Explanations for scattering of protons away from the local magnetic field

We now consider explicitly the example described in Section 4.4.1. We assume in this case that the interaction between the waves and proton is of cyclotron resonance. As described above, if resonant protons have a corotation angle near zero they will be accelerated in the perpendicular direction and their pitch angles will be increased. For there to be a net effect on the proton distribution, there must be more protons being accelerated than being decelerated in the perpendicular direction, i.e., the proton distribution must be non-gyrotropic or exhibit gyrophase bunching. For the strongest effect of this interaction we chose the corotation angle to be $\theta_c=0$ (\mathbf{E}_w and \mathbf{v}_\perp are parallel), and then using the observed $|\mathbf{B}_w|$ (the fourth panel from the top of Figure 4.2) and allowing the proton of interest to interact resonantly with the observed wave spectrum, we solved Equations (5.5) and (5.12) with different initial values of proton v_\perp , α , and E . The results for an interacting proton with the initial pitch angle $\alpha_0=40^\circ$ and parallel velocity $v_{\parallel 0}=1.8 \times 10^6$ m/s are shown in Figure 5.1. From this figure, we see that during the course of interaction v_{\parallel} of the proton decreased (the fourth panel from the top) and matched the resonance condition (Equation 5.10) with different frequencies of the wave spectrum (the fifth panel from the

top), and its v_{\perp} , α , and E all increased with time (the third, second, and first panels from the top). The proton pitch angle α changed from 40° to 83° , and E changed from 30 to 41 keV, staying in the SCATHA energy band centered at 36 keV (for this energy band $24 \leq E \leq 48$ keV) but moving into the pitch angle band included in j_{perp} . The effective time of interaction t_{interact} was about 25 seconds for covering the whole spectrum with frequency from 0.5 to 1.0 Hz (the fifth panel from the top), corresponding to the v_{IR} range from 1.8×10^6 to 0.4×10^6 m/s.

We considered other protons with the same $v_{\parallel 0}$ but different α_0 and let them interact resonantly with the waves in the same manner just described, and the results are shown in Figure 5.2. In Figure 5.2, from top to bottom, the first and second panels show the plots of proton energy and pitch angle versus interacting time for 15 different values of α_0 from 72° to 10° for this event; the third shows the plots of proton energy versus pitch angle for the same values of α_0 . The color code is the same for all three panels. Each color line corresponds to a value of α_0 and covers the whole spectrum of the waves.

We have 15 different values of α_0 , corresponding to 15 interacting protons, and the same value of $v_{\parallel 0} = 1.8 \times 10^6$ m/s that corresponds to the lower edge of the wave spectrum, $f_0 = 0.5$ Hz; $v_{\parallel 0}$ and f_0 satisfy Equation (5.10). After letting these 15 protons interact resonantly with the whole spectrum of the waves for suitable t_{interact} , their pitch angles and energies will increase by significant amounts, as explained above; thus these protons are pitch angle scattered away from \mathbf{B}_0 . As shown in Figure 5.2, depending on the value of α_0 , the energy of each proton will fall in a particular energy band centered either at 36 or

71 or 133 keV. When its α changes from below 80° to above 80° , that proton begins to contribute to the observed j_{perp} in the corresponding energy band.

From the first and second panels of Figure 5.2, we see that the scattering of protons away from the magnetic field occurred as α increased and the boundary value of $\alpha_{\text{boundary}}=80^\circ$ was crossed for the energy bands centered at 36, 71, and 133 keV. This is consistent with the observation of the peaks in j_{perp} in these 3 energy bands. We also see that for a proton interacting with the whole wave spectrum, a higher energy corresponds to a shorter t_{interact} ; t_{interact} ranges from about 45 seconds for a proton with energy less than 30 keV to less than 10 seconds for a proton with energy greater than 170 keV (for the energy band centered at 133 keV, $94 \leq E \leq 172$ keV).

It should be emphasized that it is not necessary that a proton have all successive values of v_{\parallel} in the $v_{\parallel\text{R}}$ range, which corresponds to the whole spectrum, during the course of interaction. In fact, with any initial value of v_{\parallel} that falls in that range, the proton can start interacting resonantly with the corresponding frequency in the spectrum such that Equation (5.10) is met, and its α and E will increase over time when a portion of the whole spectrum is covered; thus the proton is also pitch angle scattered away from \mathbf{B}_0 . If its α crosses α_{boundary} and its E falls in one of the three energy bands, the proton will contribute to the observed j_{perp} in that energy band. For a proton interacting with only a portion of the whole spectrum, t_{interact} is clearly shorter than that for one interacting with the whole spectrum. The nearer to 80° from below, the shorter t_{interact} required to have α above 80° . The observed significant increases in j_{perp} in these energy bands imply that the

plasma conditions were such that protons interacted resonantly with the EMIC waves for suitable times so that their pitch angles and energies increased so as to contribute to j_{perp} .

For the value $\theta_c=0$, corresponding to the strongest interaction effect, depending on the proton energy and the portion of the wave spectrum covered, the values of t_{interact} required for significant changes in proton pitch angles for different energy bands range from less than 50 seconds to less than 10 seconds. These values are shorter than the several minutes of the correlation event considered here. If we chose the value of θ_c such that $0 < |\theta_c| < \pi/2$, not corresponding to the strongest effect, the total time of interaction required would be higher but may still fall within the timescale of several minutes of the correlation event. For example, if we set $|\theta_c|$ equal to $\pi/4$ instead of 0, t_{interact} would be 1.4 times those obtained with the value of 0 and still be within the timescale of observation.

For protons in the energy band centered at 15.6 keV, the last lines, i.e., 15th Lines in the three panels of Figure 5.2 show that protons in this energy band must have a small pitch angle to satisfy the resonant condition. Therefore it takes more time for them to be scattered into the perpendicular direction. More importantly, the results show that many of the particles that might eventually have pitch angles above 70° would also have their energy increased to values high enough to remove them from the energy band centered at 15.6 keV (for the energy band centered at 36 keV, $24 \leq E \leq 48$ keV). Thus the fact that there is no observed peak in j_{perp} in this energy band for this event is consistent with the idea that the operating mechanism is the resonant interaction of the protons with the EMIC waves.

For protons in the energy bands centered at 71 and 133 keV, those observed in j_{para} have parallel velocities too high to be in resonance with the EMIC waves. Some protons in the band centered at 36 keV may be in resonance with the waves, but it is only a small fraction of those observed in j_{para} . Thus the fact that there are no significant changes in j_{para} in these energy bands is consistent with the calculations presented here.

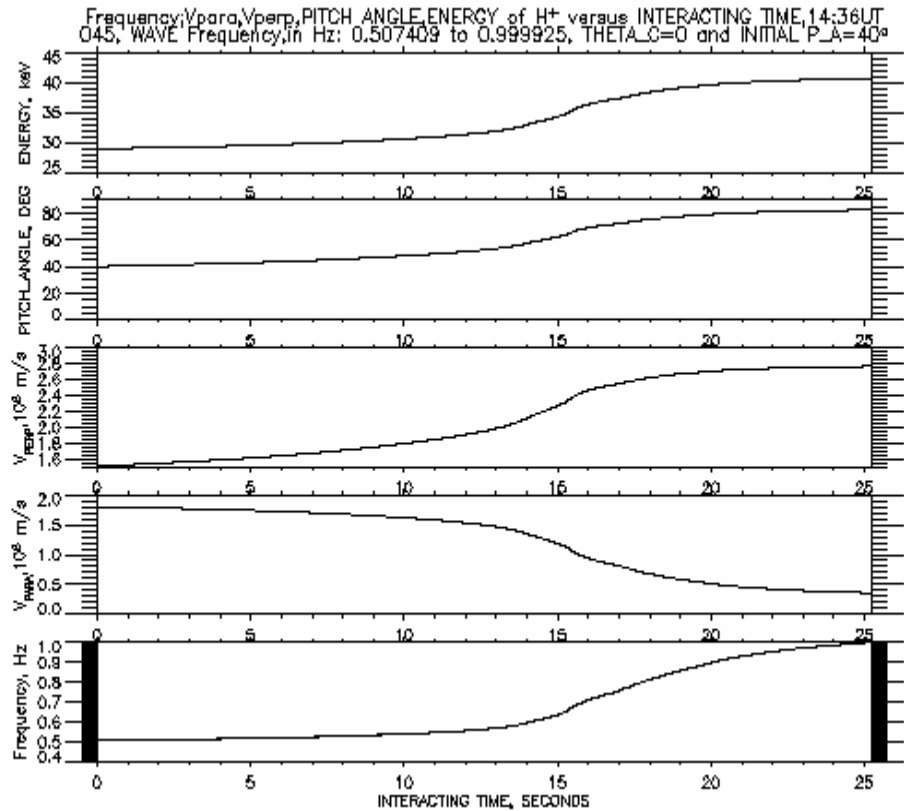


Figure 5.1 From top to bottom, the first, second, third, and fourth panels show the plots of proton energy, pitch angle, perpendicular velocity, and parallel velocity versus interacting time for the event at 14:36 UT, day 045, and the energy band centered at 36 keV; the fifth shows the plot of wave frequency versus interacting time. Initial pitch angle of the proton is 40°.

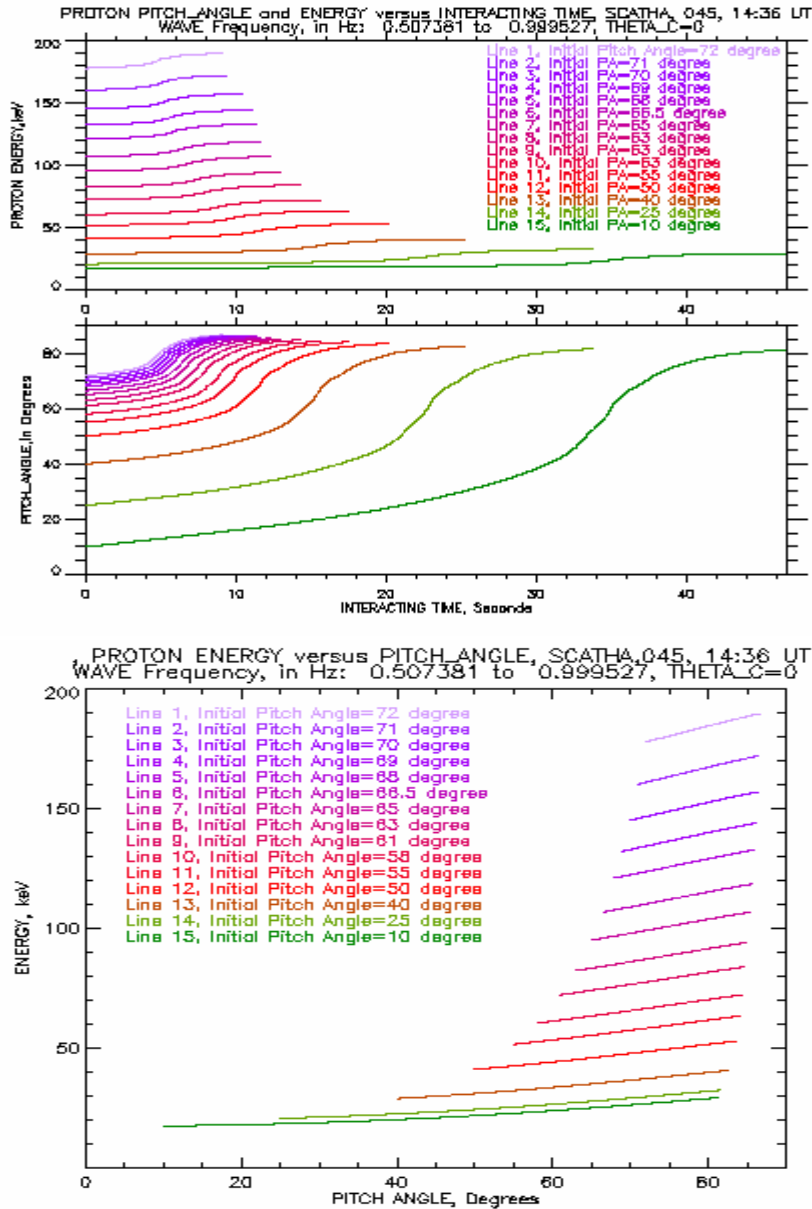


Figure 5.2 From top to bottom, the first and second panels show the plots of proton energy and pitch angle versus interacting time for 15 different values of initial pitch angle α_0 from 72° to 10° for the event at 14:36 UT, day 045; the third shows the plots of proton energy versus pitch angle for the same values of α_0 . The color code is the same for the three panels.

5.5.2 Explanations for scattering of protons toward the local magnetic field

We now consider explicitly the second example described in Section 4.4.2. We again assume that the interaction between the EMIC waves and protons is of cyclotron resonance. For the strongest effect of this interaction, we chose the corotation angle to be $|\theta_c|=\pi$ (\mathbf{E}_w and \mathbf{v}_\perp are antiparallel). Then using the observed $|\mathbf{B}_w|$ (the fourth panel from the top of Figure 4.5) and allowing the protons of interest to interact resonantly with the observed wave spectrum, we solved Equations (5.5) and (5.12) with different initial values of proton v_\perp , α , and E .

The results for 15 interacting protons with different initial pitch angles α_o from 86.0° to 80.1° and the same $v_{||o}=0.4 \times 10^6$ m/s, corresponding to the higher edge of the wave spectrum $f_o=0.98$ Hz, are shown in Figure 5.3; $v_{||o}$ and f_o satisfy Equation (5.10). In Figure 5.3, from top to bottom, the first and second panels show the plots of proton energy and pitch angle versus interacting time for different values of α_o for this event; the third shows the plots of proton energy versus pitch angle for the same values of α_o . Each color line corresponds to a value of α_o and covers the whole spectrum of the waves.

After letting these protons interact resonantly with the whole spectrum of the waves with frequency from 0.98 to 0.50 Hz, corresponding to the $v_{||R}$ range from 0.4×10^6 to 1.9×10^6 m/s, for suitable t_{interact} , their pitch angles and energies will decrease by significant amounts; thus these protons are pitch angle scattered toward \mathbf{B}_o . As shown in Figure 5.3, depending on the value of α_o , the energy of each proton will fall in a particular energy band centered either at 36 or 71 or 133 keV. When its α changes from above 80°

to below 80° , that proton no longer contributes to the observed j_{perp} in the corresponding energy band.

From the first and second panels of Figure 5.3, we see that the scattering of protons toward the magnetic field occurred as α decreased and the boundary value of $\alpha_{\text{boundary}}=80^\circ$ was crossed for protons in the energy bands centered at 36, 71, and 133 keV. This is consistent with the observation of the dips in j_{perp} in these 3 energy bands. We also see that for a proton interacting with the whole wave spectrum, a higher energy corresponds to a shorter t_{interact} ; t_{interact} ranges from less than 40 seconds for a proton with energy less than 30 keV to less than 10 seconds for a proton with energy greater than 170 keV. These values are again shorter than the timescale in which the proton perpendicular flux is correlated with the strength of the EMIC waves. This is consistent with the presumption that the observed dips in j_{perp} in these 3 energy bands are due to resonant interactions of protons with EMIC waves.

If we chose the value of θ_c such that $\pi/2 < |\theta_c| < \pi$, not corresponding to the strongest effect, the total time of interaction would be higher and may still fall within the timescale of several minutes of this correlation event. For example, if we set $|\theta_c|$ to be equal to $3\pi/4$ instead of π , t_{interact} would be 1.4 times those obtained with the value of π but still be within the timescale of observation.

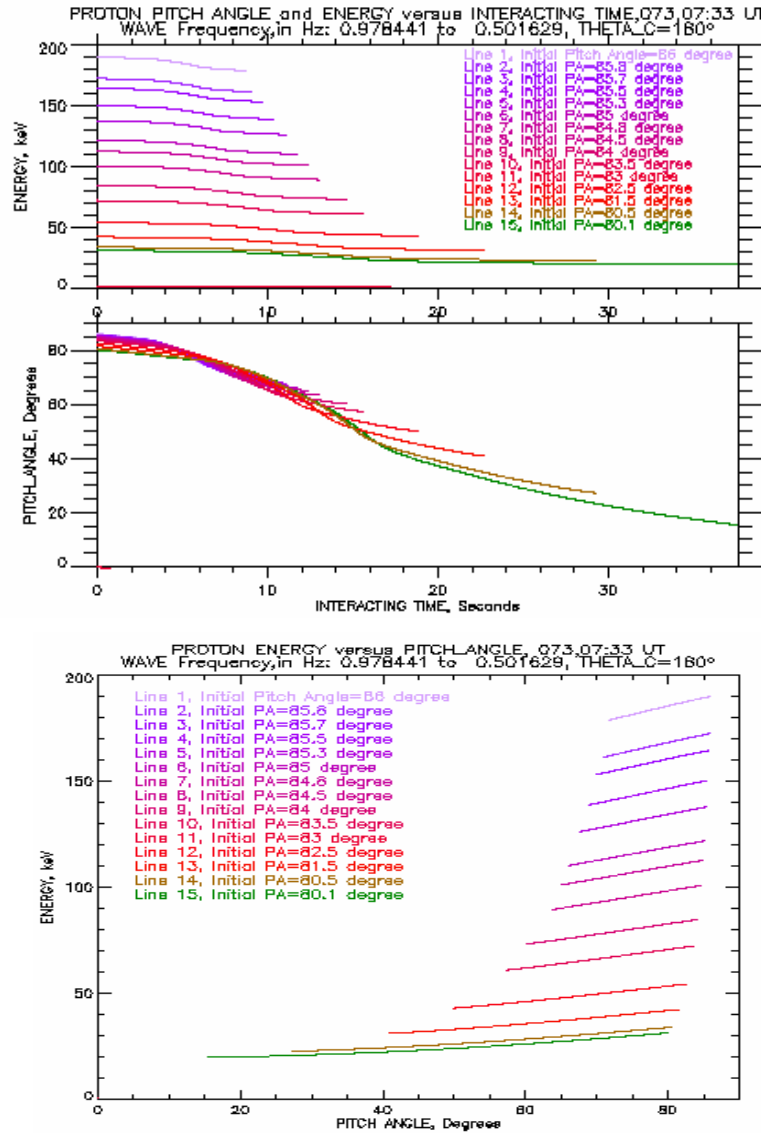


Figure 5.3 From top to bottom, the first and second panels show the plots of proton energy and pitch angle versus interacting time for 15 different values of initial pitch angle α_0 from 86° to 80.1° for the event at 07:33 UT, day 073; the third shows the plots of proton energy versus pitch angle for the same values of α_0 . The color code is the same for the three panels.

5.5.3 Explanations for scattering of protons toward and away from the local magnetic field

For the third correlation event presented in Section 4.4.3, there are dips in j_{perp} in the energy bands centered at 36, 71, and 133 keV, and a peak in j_{perp} in the energy band centered at 15.6 keV. The existence of these extremes may also be attributed to the pitch angle scatterings of protons by the present EMIC waves.

5.5.3.1 Scattering toward \mathbf{B}_0 in the bands centered at 36, 71, and 133 keV

For the dips in the energy bands centered at 36, 71, and 133 keV, we chose the corotation angle to be $|\theta_c|=\pi$ (\mathbf{E}_w and \mathbf{v}_\perp are antiparallel). Then using the observed $|\mathbf{B}_w|$ (the fourth panel from the top of Figure 4.7) and allowing the proton of interest to interact resonantly with the observed wave spectrum, we solved Equations (5.5) and (5.12) with different initial values of proton v_\perp , α , and E . The results for 11 interacting protons with different initial pitch angles α_0 from 88.22° to 86° and the same $v_{\parallel 0}=0.2 \times 10^6$ m/s, corresponding to the higher edge of the wave spectrum $f_0=1.25$ Hz, are shown in Figure 5.4. $v_{\parallel 0}$ and f_0 satisfy Equation (5.10). After letting these protons interact resonantly with the whole spectrum of the waves with frequency from 1.25 to 0.54 Hz, corresponding to the $v_{\parallel R}$ range from 0.2×10^6 to 1.9×10^6 m/s, for suitable t_{interact} , their pitch angles and energies will decrease by significant amounts; thus these protons are pitch angle scattered toward \mathbf{B}_0 . As shown in Figure 5.4, depending on the value of α_0 , the energy of each proton will fall in a particular energy band centered either at 36 or 71 or 133 keV. When its α

changes from above 80° to below 80° , that proton no longer contributes to the observed j_{perp} in the corresponding energy band.

From the first and second panels of Figure 5.4, we see that the scattering of protons toward the magnetic field occurred as α decreased and the boundary value of $\alpha_{\text{boundary}}=80^\circ$ was crossed for every energy band centered at 36 or 71 or 133 keV. This is again consistent with the observation of the dips in j_{perp} in these 3 energy bands. We also see that for a proton interacting with the whole wave spectrum, a higher energy corresponds to a shorter t_{interact} ; t_{interact} ranges from less than 52 seconds for a proton with energy less than 30 keV to less than 20 seconds for a proton with energy greater than 170 keV.

5.5.3.2 Scattering away from \mathbf{B}_0 in the band centered at 15.6 keV

For the peak in j_{perp} in the energy band centered at 15.6 keV, we chose the corotation angle to be $\theta_c=0$ (\mathbf{E}_w and \mathbf{v}_\perp are parallel). Then using the observed $|\mathbf{B}_w|$ (the fourth panel from the top of Figure 4.7) and allowing the proton of interest to interact resonantly with a portion of the wave spectrum with frequency from 0.62 to 0.93 Hz, we solved Equations (5.5) and (5.12) with initial values of proton v_\perp , α , and E . The results for 7 protons with different values of α_0 from 35° to 5° and the same value of $v_{\parallel 0}=1.5 \times 10^6$ m/s that corresponds to $f_0=0.62$ Hz, are shown in Figure 5.5. $v_{\parallel 0}$ and f_0 satisfy Equation (5.10). After letting these 7 protons interact resonantly with the waves with frequency in the range from 0.62 to 0.93 Hz, corresponding to the $v_{\parallel R}$ range from 1.5×10^6 to 0.6×10^6 m/s, for suitable t_{interact} , their pitch angles and energies will increase by significant amounts; thus these protons are pitch angle scattered away from \mathbf{B}_0 . As shown in Figure 5.5, the times

of interaction are less than 32 seconds, and when the pitch angles are above 70° , the energy of most particles remains in the 15.6 keV band. Thus the observation of the peak in this energy band is also in agreement with the calculations presented here.

For $|\theta_c|=0$, corresponding to the strongest interaction effect, again depending on the proton energy and the portion of the wave spectrum covered, the values of t_{interact} required for significant changes in proton pitch angle for this energy band are less than 32 seconds. These values are also shorter than the timescale of several minutes of the correlation event considered here. If we chose the value of θ_c such that $0 < |\theta_c| < \pi/2$, not corresponding to the strongest effect, the total time of interaction would be higher but still fall within the timescale of this correlation event.

The simple analysis presented here gives no explanations for why the correlation angle is 180 degrees at high energies and 0 degree at low energies. The observations, however, seem to require this unusual pitch angle distribution, and the calculations presented in this section show that under the proper conditions the existing EMIC waves could be responsible for the observed changes in proton perpendicular flux.

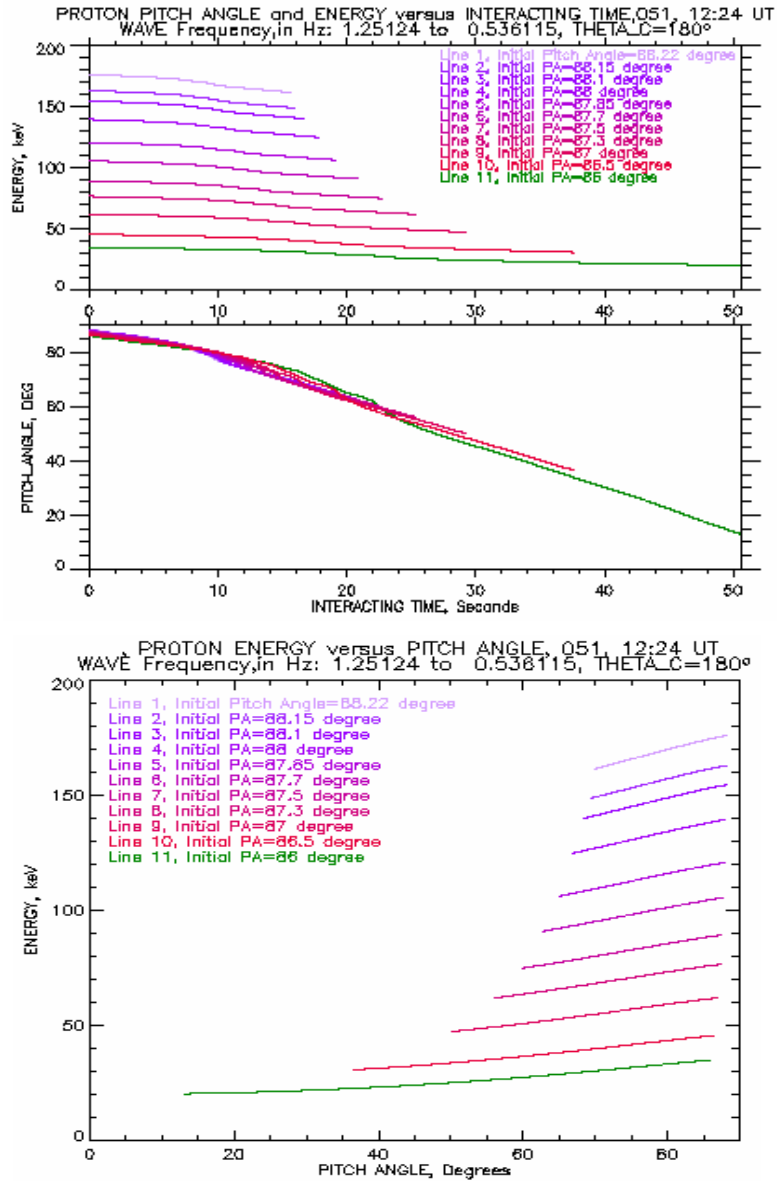


Figure 5.4 From top to bottom, the first and second panels show the plots of proton energy and pitch angle versus interacting time for 11 different values of initial pitch angle α_0 from 88.22° to 86° for the event at 12:24 UT, day 051; the third shows the plots of proton energy versus pitch angle for the same values of α_0 . The color code is the same for the three panels.

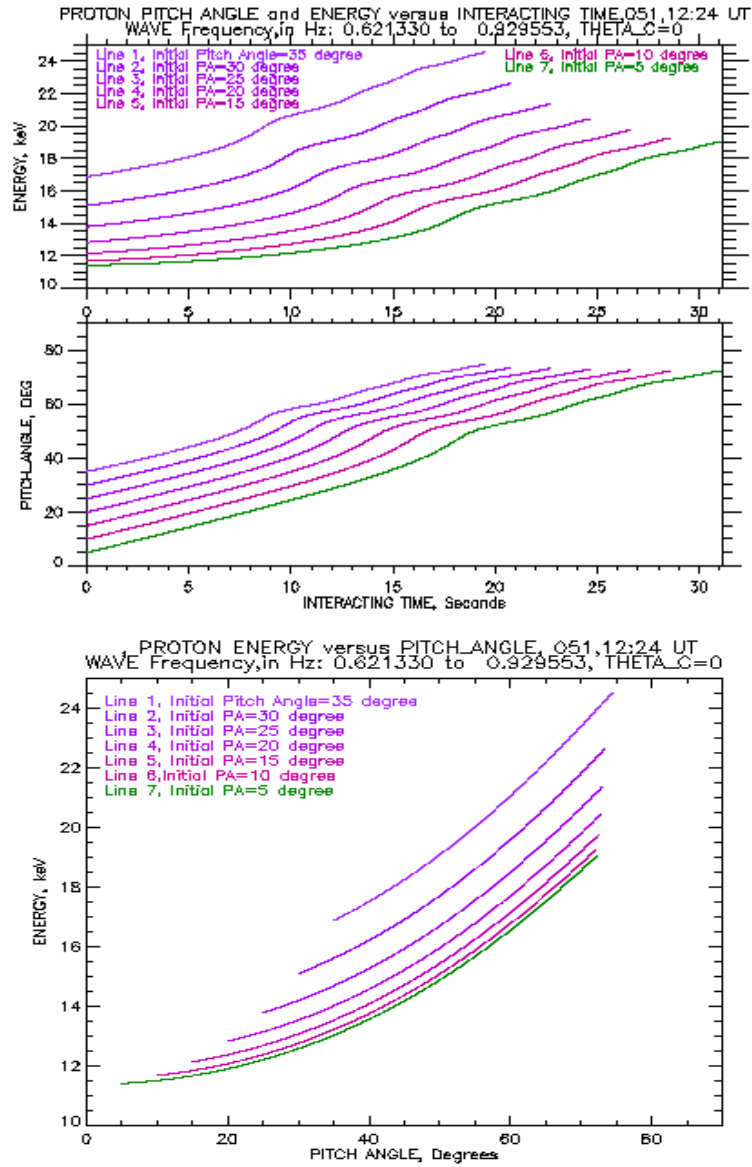


Figure 5.5 From top to bottom, the first and second panels show the plots of proton energy and pitch angle versus interacting time for 7 different values of initial pitch angle α_0 from 35° to 5° for the event at 12:24 UT, day 051; the third shows the plots of proton energy versus pitch angle for the same values of α_0 . The color code is the same for the three panels.

5.6 Discussions

To our knowledge there have not been in situ observations of correlations between EMIC waves and proton perpendicular differential fluxes in the magnetosphere. The theoretical studies of the role of energetic and anisotropic proton populations in generating EMIC waves in the magnetosphere found that EMIC waves get free energy from such populations and scatter protons toward the local magnetic field. This is supported by the observations of proton precipitations in the auroral or polar regions, as mentioned in Section 1.4. We for the first time report in situ observations of correlations between EMIC waves and proton perpendicular differential fluxes, possibly showing that protons are pitch angle scattered toward or away from \mathbf{B}_0 due to interactions with EMIC waves in the magnetosphere.

Resonant wave growth/amplification and particle scattering in general requires a nonlinear treatment. Wave energy and particle energy are conserved together; the waves gain energy at the expense of the interacting particles and vice versa. If we assume, however, that the wave amplitudes are sufficiently small, we can treat the wave growth/amplification and particle scattering separately. In this chapter we show that this treatment gives the results in agreement with the observed features.

Our approach is to allow individual protons to interact resonantly with the whole or a portion of the spectrum of EMIC waves and to assume a non-gyrotropy feature of the distributions of the interacting proton populations. Depending on the frequency spectrum of the waves and the initial value of v_{\parallel} of the interacting proton, its pitch angle and energy can change significantly owing to the resonant interaction with the present waves, and the proton is pitch angle scattered either away from or toward the local magnetic field. If the

value of α_{boundary} is crossed, the contributing status of the proton to the observed j_{perp} also changes. If the local plasma conditions are favorable, i.e., existing of non-gyrotropic proton distributions or gyrophase bunching, there are many protons that interact resonantly with the same waves in the same fashion and are then pitch angle scattered either away from or toward \mathbf{B}_0 , and the number of protons scattered away from \mathbf{B}_0 is significantly greater/smaller than that of protons scattered toward \mathbf{B}_0 , leading to a peak/dip in j_{perp} , as observed. For $|\theta_c|=0$ or π , that corresponds to the strongest effect of the resonant interactions, depending on the energies of the interacting protons, t_{interact} falls in the range from less than 10 seconds to less than 50 seconds, shorter than the timescales of several minutes of the observed correlations.

To show that the changes in proton perpendicular flux may be indeed caused by resonant interactions with the EMIC waves, we presented calculations of single protons interacting with the observed EMIC spectrum. Our approach is similar to that of *Gendrin* [1968] in allowing protons whose v_{\parallel} are changing to interact resonantly with different frequencies of electromagnetic waves, satisfying the resonance condition. The energies of the particles also change during the course of resonant interaction. *Gendrin* [1968], however, put emphasis on calculations of pitch angle and energy diffusion coefficients, assuming a diffusive process of wave particle interaction with durations of many hours. In our investigation, it was observed clearly that the timescales of the correlations were only a few minutes, and so the observed peaks/dips in j_{perp} may result from the deterministic pitch angle scatterings of protons with respect to \mathbf{B}_0 due to resonant interactions with EMIC waves, i.e., not from diffusive processes. For diffusive pitch angle scatterings of

protons by EMIC waves, the results of the studies by *Cornwall et al.* [1970], *Lyon and Thorne* [1972], *Jordanova et al.* [1997], and *Kozyra et al.* [1997] showed that it would take hours to have significant effects on the proton populations, as mentioned in Sect. 1.4.

Our calculations were based on the resonant interactions of single protons with selected phase angles with respect to the EMIC waves, while the observed j_{perp} were the result of the behavior of a full distribution of protons. In reality, the processes of scattering protons toward and away from \mathbf{B}_0 compete with each other. Only when the local plasma conditions favor one process over the other, does a strong correlation result in and a clear peak or dip in j_{perp} is generated. This implies that in the special cases reported here there were proton pitch angle distributions that were not only anisotropic but also non-gyrotropic.

We emphasize that if the observations are indeed indicative of non-gyrotropic proton distribution functions, they are not the norm. The suggestive events are only a small fraction of the observed EMIC emissions. This result is not totally unexpected. Non-gyrotropic distributions in the geosphere have been observed experimentally and predicted theoretically. The simulation study of *Hoshino and Teresawa* [1985] suggested that an electromagnetic ion beam instability can be a direct source of gyrophase bunching. *Pantellini et al.* [1994] used the linearized Vlasov theory and the Liouville mapping method to investigate the linear evolution of particle distribution functions in kinetic instabilities in a homogeneous collisionless plasma. For the electromagnetic ion cyclotron instability with parallel propagation, they found that the instability is driven by ions undergoing cyclotron resonance and that the ion velocity distributions are non-gyrotropic during the linear phase of the growth. The simulation study of *Gary et al.* [1996] showed

that the enhanced fluctuations from the electromagnetic proton cyclotron instability drive a hot proton distribution function that is initially non-gyrotropic toward the gyrotropic condition in the postsaturation phase. *Thomsen et al.* [1985] observed gyrophase bunched ions associated with nearly monochromatic, low frequency hydromagnetic waves in the upstream of the Earth's bow shock using data from ISEE-1 and -2. *Eastman et al.* [1981] also using data from ISEE-1 and -2 found correlations between enhanced broadband (100 Hz to ~10 kHz) emissions and non-gyrotropic distributions of energetic ions in the Earth's foreshock region. The existence of non-gyrotropic distribution of alpha particles and protons in the solar wind plasma and a close relation between the non-gyrotropy of the particle distributions and the large temperature anisotropies were also found by *As-tudillo et al.* [1996] at heliocentric distances near 1.3 AU, using data obtained in the experiment TAUS on the PHOBOS-2 mission to planet Mars. Thus the existence of non-gyrotropic distributions under unusual conditions is not unreasonable.

5.7 Conclusions

The main conclusions drawn from the investigation presented in Chapter 4 and Chapter 5 are as follows

- 1) Using SCATHA data, we found correlations between the EMIC wave occurrences and the observed proton perpendicular differential fluxes in 20 time intervals. These intervals were mainly near local noon and in the evening sector with L values from 5.6 to 7.5 and magnetic latitudes within 15 degrees of the equator, and accounted for only a small fraction, approximately 3.5%, of the total time of wave observation. The wave

frequencies fell in the range 0.16-1.06 Hz corresponding to 0.06-0.56 normalized to the local proton gyrofrequency. The waves observed in these time intervals had rather broad bands, allowing effective scatterings of protons.

2) Linear analysis of the resonant interaction of individual protons with the observed EMIC waves shows that it is reasonable to attribute the changes in proton perpendicular flux to the deterministic pitch angle scatterings of protons with respect to the local magnetic field, as a result of their interactions with the existing EMIC waves.

3) Based on cyclotron resonance and the parallel propagation of EMIC waves and the assumption of a non-gyrotropy feature of the pitch angle distributions of the interacting proton populations, the calculation results are consistent with the observations.

CHAPTER 6

SUMMARY AND CONCLUSIONS

The role of electromagnetic ion cyclotron waves in governing proton populations in the ring current and radiation belt regions is very important in understanding the dynamics of the magnetosphere. Magnetic field data obtained by SCATHA in the form of time series with the sampling interval of 0.25 second, corresponding to the Nyquist frequency of 2 Hz, are suitable for identifying and obtaining power spectra of EMIC waves in the equatorial region of the magnetosphere. To identify and obtain power spectra of EMIC waves from these data, we employed the fast Fourier transform and spectral analysis techniques. The fast Fourier transform is used because it is a very advanced and rapid technique for calculating wave power spectra and polarization parameters from the measured magnetic field time series.

First, the obtained wave power spectra were used to investigate the conditions under which the electromagnetic proton cyclotron instability acts as a generation mechanism for EMIC waves in the region. Based upon the event selection criteria, 520 were selected out of 1181 events identified from 59 days of SCATHA magnetic field data for this investigation. The results of the analysis of these 520 events can be summarized as follows

1) There are several findings that are consistent with those of previous studies and/or with theoretical expectations, including (a) the inverse correlation between proton temperature anisotropy and proton parallel beta and that the observed A_p are above the electromagnetic proton cyclotron instability thresholds, (b) that the observed waves actually get energy from energetic and anisotropic proton populations, and (c) that the peak normalized frequencies of the observed waves are less than 0.7 for the observed range of A_p .

2) The inverse correlation $A_p = S_p \beta_{\parallel p}^{\alpha_p}$ holds not only for all events considered but also for those in different local time sectors and L ranges. More interestingly, a similar relation between A_p and T_{\perp} , given by Equation $A_p = a T_{\perp}^b$, is also established. This relation again applies for all events and for those in different MLT sectors and L ranges. The coefficients of the two relations are found to depend on macroscopic factors such as MLT and L value, reflecting the degree of strength of external forces driving the energetic proton temperature anisotropy.

3) The longitudinal or MLT variations are outstanding. The events in the dawn sector have rather high A_p , mainly low $\beta_{\parallel p}$, rather low T_{\perp} , and X mainly between 0.2 and 0.6. Those in the noon sector have mainly high A_p , mainly low $\beta_{\parallel p}$, low T_{\perp} , and X concentrating in the range between 0.27 and 0.55. Those in the evening sector have lowest A_p , highest $\beta_{\parallel p}$, highest T_{\perp} , and X concentrating at $X < 0.22$. The events in the midnight sector occur with limited ranges of A_p , $\beta_{\parallel p}$, and T_{\perp} , and with X just between 0.27 and 0.40.

4) The radial variations are also notable. It is found that moving outward, or increasing L value, corresponds to increased A_p , in agreement with the drift shell splitting process, and also to lower β_{lp} and higher X .

Second, besides magnetic field data, the experiments on board SCATHA also provide proton spectra data, allowing us to study the relationship between EMIC waves and protons. From 58 days of magnetic field and proton spectra data, we found that there were 20 short time intervals showing correlations between EMIC waves and proton perpendicular differential fluxes. They indicate that under suitable conditions, EMIC waves indeed pitch angle scatter protons either toward or away from the local magnetic field \mathbf{B}_0 .

These observations required theoretical explanations. Therefore, we also established a model that is based on resonant interactions between EMIC waves and protons. In this model individual protons interact resonantly with the whole or a portion of the spectrum of the existing EMIC waves and are then pitch angle scattered with respect to \mathbf{B}_0 . Calculations based on this model are in agreement with the observations and suggest that the EMIC waves are producing the changes in proton distributions by pitch angle scattering protons with respect to the local ambient magnetic field. Depending on the frequency spectrum of the waves and the initial value of $v_{||}$ of the interacting proton, the proton pitch angle and energy can change significantly owing to resonant interactions with the present EMIC waves. If the local plasma conditions are favorable, i.e., existing of non-gyrotropic proton distributions, there are many protons that interact resonantly with the same waves and are then pitch angle scattered either away from or toward \mathbf{B}_0 , and the

number of protons scattered away from \mathbf{B}_0 is significantly greater/smaller than that of protons scattered toward \mathbf{B}_0 , leading to peaks/dips in j_{perp} , as observed.

In our investigation, it was observed clearly that the timescales of correlations were only a few minutes, and so the observed peaks/dips in j_{perp} may result from the deterministic pitch angle scatterings of protons with respect to \mathbf{B}_0 due to the resonant interactions with EMIC waves, not from diffusive processes.

The main results of this investigation are given below

1) Correlations between the EMIC wave occurrences and the observed proton perpendicular differential fluxes were found in 20 time intervals. These intervals were mainly near local noon and in the evening sector with L values from 5.6 to 7.5 and magnetic latitudes within 15 degrees of the equator, and accounted for approximately 3.5% of the total time of wave observation. The waves observed in these time intervals had rather broad bands, allowing effective scatterings of protons.

2) Linear analysis of the resonant interaction of individual protons with the observed EMIC waves shows that it is reasonable to attribute the changes in proton perpendicular flux to the pitch angle scatterings of protons with respect to the local magnetic field, as a result of the resonant interactions with the existing EMIC waves.

3) The calculation results, based on proton cyclotron resonance and the parallel propagation of EMIC waves and the assumption of a non-gyrotropy feature of the proton pitch angle distributions, are in agreement with the observations.

REFERENCES

- Albert, J. M. (2003), Evaluation of quasi-linear diffusion coefficients for EMIC waves in a multispecies plasma, *J. Geophys. Res.*, *108(A6)*, 1249, doi:10.1029/2002JA009792.
- Anderson, B. J., and S. A. Fuselier (1993), Magnetic pulsations from 0.2 to 4 Hz and associated plasma properties in the Earth's subsolar magnetosheath and plasma depletion layer, *J. Geophys. Res.*, *98*, 1461.
- Anderson, B. J., and D. C. Hamilton (1993), Electromagnetic Ion Cyclotron Waves Stimulated by Modest Magnetospheric Compressions, *J. Geophys. Res.*, *98*, 11369-11382.
- Anderson, B. J., K. Takahashi, R. E. Erlandson, and L. J. Zanetti (1990), Pc1 pulsations Observed by AMPTE/CCE in the Earth's outer magnetosphere, *Geophys. Res. Lett.*, *17*, 1853.
- Anderson, B. J., R. E. Erlandson, and L. J. Zanetti (1992a), A statistical study of Pc1-2 magnetic pulsations in the equatorial magnetosphere: 1. Equatorial occurrence distribution, *J. Geophys. Res.*, *97*, 3075.
- Anderson, B. J., R. E. Erlandson, and L. J. Zanetti (1992b), A statistical study of Pc1-2 magnetic pulsations in the equatorial magnetosphere: 2. Wave properties, *J. Geophys. Res.*, *97*, 3089.
- Anderson, B. J., S. A. Fuselier, S. P. Gary, and R. E. Denton (1994), Magnetic spectral

- signatures in the Earth's subsolar magnetosheath and plasma depletion layer, *J. Geophys. Res.*, *99*, 5877.
- Anderson, B. J., R. E. Denton, G. Ho, D. C. Hamilton, S. A. Fuselier, and R. J. Strangeway (1996), Observational test of local proton cyclotron instability in the Earth's magnetosphere, *J. Geophys. Res.*, *101*, 21527-21543.
- Arnoldy, R. L., M. J. Engebretson, R. E. Denton, J. L. Posch, M. R. Lessard, N. C. Maynard, D. M. Ober, C. J. Farrugia, C. T. Russell, J. D. Scudder, R. B. Torbert, S.-H. Chen, and T. E. Moore (2005), Pc 1 waves and associated unstable distributions of magnetospheric protons observed during a solar wind pressure pulse, *J. Geophys. Res.*, *110*, A07229, doi:10.1029/2005JA011041.
- Astudillo, H. F., S. Livi, E. Marsch, and H. Rosenbauer (1996), Evidence for nongyrotropic alpha particle and proton distribution functions: TAUS solar wind measurements *J. Geophys. Res.*, *101*, 24423-24432.
- Axford, W. I. (1964), Viscous interaction between the solar wind and the Earth's magnetosphere, *Planet. Space Sci.*, *12*, 45.
- Axford, W.I., and C. O. Hines (1961), A unifying theory of high-latitude geophysical phenomena and geomagnetic storms, *Can. J. Phys.*, *39*, 1433.
- Baumjohann, W., and R. A. Treumann (1996), Basic Space Plasma Physics, *Imperial College Press*, p. 288.
- Bossen, M., R. L. McPherron, and C. T. Russell (1976), A statistical study of Pc1 magnetic pulsations at synchronous orbit, *J. Geophys. Res.*, *81*, 6083.
- Boyd, T. J. M., and J. J. Sanderson (2003), The Physics of Plasmas, *Cambridge University Press*, p. 201.

- Brice, N. (1964), Fundamentals of Very Low Frequency Emission and Generating Mechanism, *J. Geophys. Res.*, *69*, 4515.
- Buckley, R., Some notes on practical digital power spectral, auto- and cross correlation analysis using the fast Fourier transform (1971), *Department of Physics, The University of Adelaide, Australia*, 1971.
- Carpenter, D. L., A. J. Smith, B. L. Giles, C. R. Chappell, P. M. E. Decreau, R. R. Anderson, A. M. Persoon, A. J. Smith, Y. Corcuff, and P. Canu (1993), Plasmasphere dynamics in the duskside bulge region: A new look at an old topic, *J. Geophys. Res.*, *98*, 19243.
- Chappell, C. R. (1974), Detached plasma Regions in the magnetosphere, *J. Geophys. Res.*, *79*, 1861.
- Chaston, C. C., Y. D. Hu, and B. J. Fraser (2000), Quasi-linear ion cyclotron heating in the near-Earth magnetotail, *J. Geophys. Res.*, *105(A3)*, 5507-5516.
- Cooley, J. W., and J. W. Tukey (1965), An algorithm for the machine calculation of complex Fourier series, *Math. Computation*, *19*, 297.
- Cooley, J. W., P. A. W. Lewis, and P. D. Welch (1969), The fast Fourier transform and its applications, *IEEE Trans. Ed.*, *12*, 27.
- Cornwall, J. M. (1965), Cyclotron instabilities and electromagnetic emissions in the ultra-low frequency and very-low frequency ranges, *J. Geophys. Res.*, *70*, 61.
- Cornwall, J. M., F. V. Coroniti, and R. M. Thorne (1971), Unified theory of SAR arc formation at the plasmopause, *J. Geophys. Res.*, *76*, 4428.
- Cornwall, J. M., F. V. Coroniti, and R.M. Thorne (1970), Turbulent loss of ring current protons, *J. Geophys. Res.*, *75*, 4699.

- Craven, P. D., R. C. Olsen, J. Fennell, D. Croley, and T. Aggson (1985), Potential Modulation on the SCATHA Spacecraft, *J. Spacecraft, Vol. 24, No. 2*, 150-157.
- Criswell, D. R. (1969), Pc1 micropulsation activity and magnetospheric application of 0.2 to 5.0 Hz hydromagnetic waves, *J. Geophys. Res.*, *74*, 205.
- Decreau, P. M. E., C. Beghin, and M. Parrot (1982), Global characteristics of the cold plasma in the equatorial plasmopause region as ducted from the GEOS-1 mutual impedance probe, *J. Geophys. Res.*, *87*, 695.
- Denton, R. E., J. Goldstein, and J. D. Menietti (2002), Field line dependence of magnetospheric electron density, *Geophys. Res. Lett.*, *29*, No 24, 58.
- Dungey, J. W. (1961), Interplanetary magnetic field and the auroral zones, *Phys. Rev. Lett.*, *6*, 47.
- Eastman, T. E., R. R. Anderson, and L. A. Frank (1981), Upstream Particles Observed in the Earth's Foreshock Region, *J. Geophys. Res.*, *86*, 4379-4395.
- Erlandson, R. E., L. J. Zanetti, T. A. Poterma, L. P. Block, and G. Homgren (1990), Viking magnetic and electric field observation of Pc1 waves and high latitudes, *J. Geophys. Res.*, *95*, 5941.
- Erlandson, R. E., and A. J. Ukhorskiy (2001), Observations of electromagnetic ion cyclotron waves during geomagnetic storms: Wave occurrence and pitch angle scattering, *J. Geophys. Res.*, *106(A3)*, 3883-3995.
- Fennell, J. F. (1982), Description of P78-2 (SCATHA) satellite and experiment, pages 68-81, in *The IMS Source book, Guide to the International Magnetospheric Study data Analysis*, edited by C. T. Russell and D. J. Southwood, American Geophysical Union, Wash. DC.

- Fennell, J. F., G. M. Boyd, M. T. Redding, and M. C. McNab (1997), Data Recovery from SCATHA satellite, Prepared for European Space Research and Technology Centre, Noordwijk, The Netherlands, Contract No. 11006/94/NL/CC and National Aeronautics and Space Administration, Washington, DC 20546, Grant No. NAGW-4141, Space and Environment Technology Center, the Aerospace Corporation.
- Fowler, R. A., B. J. Kotick, and R. D. Elliott (1967), Polarization analysis of natural and artificially induced geomagnetic pulsations, *J. Geophys. Res.*, *72*, 2871.
- Fraser, B. J. (1968), Temporal variation in Pc1 geomagnetic micropulsations, *Planet. Space Sci.*, *16*, 111.
- Fraser, B. J. (1985), Observations of ion cyclotron waves near synchronous orbit and on the ground, *Space Sci. Rev.*, *42*, 357.
- Fraser, B. J., J. C. Samson, Y. D. Hu, R. L. McPherron, and C. T. Russell (1992), Electromagnetic ion cyclotron waves observed near the oxygen cyclotron frequency by ISEE 1 and 2, *J. Geophys. Res.*, *97*, 3063.
- Fraser, B. J., and T. S. Nguyen (2001), Is the Plasmapause a Preferred Source Region of Electromagnetic Ion Cyclotron Waves in the Magnetosphere, *Journal of Atmospheric and Solar-Terrestrial Physics*, *63*, 1225.
- Fraser, B. J., H. J. Singer, W. J. Hughes, J. R. Wygant, R. R. Anderson, and Y. D. Hu (1996), CRRES Poynting vector observation of electromagnetic ion cyclotron waves near the plasmapause, *J. Geophys. Res.*, *101*, 15331.
- Frey, H. U., G. Haerendel, S. B. Mendel, W. T. Forrester, T. J. Immel, and N. Østgaard (2004), Subauroral morning proton spots (SAMPS) as a result of plasmapause-ring-current interaction, *J. Geophys. Res.*, *109*, A10305, doi:10.1029/2004JA010516,

- Fuselier, S. A., S. P. Gary, M. F. Thomsen, E. S. Claflin, B. Hubert, B. R. Sandel, and T. Immel (2004), Generation of transient dayside subauroral proton precipitation, *J. Geophys. Res.*, *109*, A12227, doi:10.1029/2004JA010393.
- Gary, S. P., M. D. Montgomery, D. W. Feldman, and D. W. Forslund (1976), Proton temperature anisotropy instability in the solar wind, *J. Geophys. Res.*, *81*, 1241.
- Gary, S. P. (1993), Theory of space plasma microinstabilities, Cambridge Atmospheric and Space Science Series, p. 128, *Cambridge University Press*.
- Gary, S. P., and M. A. Lee (1994), The ion cyclotron instability and the inverse beta correlation between proton anisotropy and proton beta, *J. Geophys. Res.*, *99*, 11297.
- Gary, S. P., M. E. McKean, D. Winske, B. J. Anderson, R. E. Denton, and S. A. Fuselier (1994a), Proton cyclotron anisotropy and the anisotropy/beta inverse correlation, *J. Geophys. Res.*, *99*, 5903.
- Gary, S. P., M. B. Moldwin, M. F. Thomsen, D. Winske, and D. J. McComas (1994b), Hot proton anisotropies and cool proton temperatures in the magnetosphere, *J. Geophys. Res.*, *99*, 23603.
- Gary, S. P., V. M. Vazquez, and D. Winske (1996), Electromagnetic ion cyclotron instability: Proton velocity distributions, *J. Geophys. Res.*, *101*, 13327-13333.
- Gendrin, R. (1968), Pitch Angle Diffusion of Low Energy Protons due to Gyroresonant Interaction with Hydromagnetic Waves, *J. of Atmos. and Terr. Physics*, *30*, 1313-1330.
- Gendrin, R., S. Lacourly, A. Roux, J. Solomon, F. Z. Feigin, M. V. Gokhberg, V. A. Troitskaya, and V. L. Yakimenko (1971), Wave packet propagation in an amplifying medium and its application to the dispersion characteristics and to the generation

- mechanisms of Pc1 events, *Planet. Space Sci.*, 19, 165.
- Gendrin, R., and A. Roux (1980), Energization of Helium Ions by Proton-Induced Hydromagnetic Waves, *J. Geophys. Res.*, 85, 4577-4586.
- Ginet, G. P., and J. M. Albert (1991), Test particle motion in the cyclotron resonance regime, *Phys. Fluids B*, 3(11), 2994.
- Gomberoff, L., G. Gnani, and F. T. Gratton (1995), Parametric decays of electromagnetic ion cyclotron waves in a H^+ - He^+ - O^+ magnetospheric plasma, *J. Geophys. Res.*, 10, 17220-17229.
- Gomberoff, L., and R. Neira (1983), Convective growth rate of ion cyclotron waves in a H^+ - He^+ and H^+ - He^+ - O^+ plasma, *J. Geophys. Res.*, 88, 2170.
- Gubbins, D. (2004), Time Series Analysis and Inverse Theory for Geophysicists, published by the Press Syndicate of the University of Cambridge, *Cambridge University Press*.
- Guglielmi, A. V., K. Hayashi, R. Lundin, and A. Potapov (1999), Ponderomotive impacts in the equatorial zone of the magnetosphere, *Earth Planet Space*, 51, 1297-1308.
- Hargreaves, J. K. (1979), The Upper Atmosphere and Solar-Terrestrial Relation: An Introduction to the Aerospace Environment, Chapter 9: Waves in the Magnetosphere, *Van Nostrand Reinhold Co., Ltd.*
- Helliwell, R. A. (1970), Particles and Fields in the Magnetosphere: Intensity of Discrete VLF Emissions, P. 292, Vol. 17, Astrophysics and Space Science Library (edited by B. M. McCormac), *D. Reidel Publishing Company, Dordrecht-Holland*.
- Horne, R. B., and R. M. Thorne (1990), Ion Cyclotron Absorption at the Second Harmonic of the Oxygen Gyrofrequency, *Geophys. Res. Lett.*, 17, 2225-2228.

- Horwitz J. L., and T. E. Moore (2000), Core Plasmas in Space Weather, *IEEE Transactions on Plasma Science*, vol. 28, No. 6, p. 1840-1853.
- Hoshino, M., and T. Terasawa (1985), Numerical Study of the Upstream Wave Excitation Mechanism, 1. Nonlinear Phase Bunching of Beam Ions (1985), *J. Geophys. Res.*, 90, 57-64.
- Hundhausen, A. J. (1995), The solar wind, in Introduction to space physics, ed. by M. G. Kivelson and C. T. Russell, *Cambridge University Press, New York*.
- Ishida, J., S. Kokubun, and R. L. McPherron (1987), Substorm effects on spectral structures of Pc1 waves at synchronous orbit, *J. Geophys. Res.*, 92, 143.
- Jordanova, V. K., C. J. Farrugia, R. M. Thorne, G. V. Khazanov, G. D. Reeves, and M. F. Thomsen (2001), Model of the ring current proton precipitation by electromagnetic ion cyclotron waves during the May 14-16, 1997, storm, *J. Geophys. Res.*, 106, 7.
- Jordanova, V. K., J. U. Koryza, A. F. Nagy, and G. V. Khazanov (1997), Kinetic model of the ring current-atmosphere interactions, *J. Geophys. Res.*, 102, 14279.
- Kanasewich, E. R. (1973), Time sequence analysis in geophysics, *Uni. Alberta Press, Edmonton*.
- Kaye, S. M., and M. G. Kivelson (1979), Observations of Pc1-2 waves in the outer magnetosphere, *J. Geophys. Res.*, 84, 4267.
- Kennel C. F., and F. Engelmann (1966), Velocity Space Diffusion from Weak Plasma Turbulence in a Magnetic Field, *Phys. Fluids*, 9, 2377.
- Kennel, C. F., and H. E. Petschek (1966), Limit on stably trapped particle fluxes, *J. Geophys. Res.*, 71, 1.
- Khazanov, G. V., K. V. Gamayunov, and V. K. Jordanova (2003), Self-consistent model

- of magnetospheric ring current and electromagnetic ion cyclotron waves: The 2-7 May 1998 storm, *J. Geophys. Res.*, *108(A12)*, 1419.
- Kintner, P. M., and D. A. Gurnett (1977), Observations of ion cyclotron waves within the plasmasphere by Hawkeye 1, *J. Geophys. Res.*, *82*, 2314.
- Kodera, K., R. Gendrin, and C. de Villedary (1977), Complex representation of a polarized signal and its application to the analysis of ULF waves, *J. Geophys. Res.*, *82*, 1245.
- Kozyra, J. U., T. E. Cravens, A. F. Nagy, E. G. Fontheim, and R. S. B. Ong (1984), Effects of energetic heavy ions on electromagnetic ion cyclotron wave generation in the plasmopause region, *J. Geophys. Res.*, *99*, 2217-2233.
- Kozyra, J. U., V. K. Jordanova, R. B. Horne, and R. M. Thorne (1997), Modeling of the Contribution of Electromagnetic Ion Cyclotron (EMIC) Waves to Stormtime Ring Current Erosion, in *Magnetic Storms, Geophysical Monograph 98*, 187-202.
- LaBelle, J., and R. A. Treumann (1992), Poynting vector measurement of electromagnetic ion cyclotron waves in the plasmasphere, *J. Geophys. Res.*, *97*, 13789.
- Liemohn, H. B., J. F. Kenney, and H. B. Knafllich (1967), Proton densities in the magnetosphere from pearl dispersion measurement, *Earth Planet. Sci. Lett.*, *2*, 360.
- Lorentzen, K. R., M. P. McCarthy, G. K. Parks, J. E. Foat, R. M. Milan, D. M. Smith, and R. P. Lin (2000), Precipitation of relativistic Electrons by Interaction with electromagnetic ion cyclotron waves, *J. Geophys. Res.*, *105(A3)*, 5381-5389.
- Lyons, L. R., and D. J. Williams (1984), *Quantitative aspects of Magnetospheric Physics*, *D. Reidel*, Dordrecht, Holland.

- Lyons, L. R., and R. M. Thorne (1972), Parasitic pitch angle diffusion of radiation belt particles by ion cyclotron waves, *J. Geophys. Res.*, *77*, 5608-5616.
- Mauk, B. H. (1982), Helium resonance and dispersion effects on geostationary Alfvén/ion cyclotron waves, *J. Geophys. Res.*, *87*, 9107.
- Mauk, B. H., and R. L. McPherron (1980), An experimental test of the electromagnetic ion cyclotron instability within the Earth's magnetosphere, *Phys. Fluid*, *23*, 2111.
- McPherron, R. L., C. T. Russell, and P. J. Coleman, Jr. (1972), Fluctuating magnetic fields in the magnetosphere, II, ULF waves, *Space Sci. Rev.*, *13*, 411.
- Means, J. D. (1972), Use of the three-dimensional covariance matrix in analyzing the polarization properties of plane waves, *J. Geophys. Res.*, *77*, 5551.
- Meredith, N. P., R. M. Thorne, R. B. Horne, D. Summers, B. J. Fraser, and R. R. Anderson, Statistical analysis of relativistic electron energies of cyclotron resonance with EMIC waves observed on CRRES, *J. Geophys. Res.*, *108*, pp. SMP 17-1, doi:10.1029/2002JA009700.
- Moldwin, M. B., M. F. Thomsen, S. J. Bame, D. J. McComas, L. A. Weiss, G. D. Reeves, and R. D. Belian (1996), The appearance of plasmaspheric plasma in the outer magnetosphere in association with substorm growth phase, *Geophys. Res. Lett.*, *23*, No. 8, 801-804.
- Moldwin, M. B., B. R. Sandel, M. F. Thompson, and R. C. Elphic (2003), Quantifying global plasmaspheric images with in situ observations, *Space Science Reviews*, *109*, 47-61.
- Moukikis C. G., L. M. Kistler, W. Baumjohann, E. J. Lund, A. Korth, B. Klecker, M. A. Popecki, J. A. Sauvaud, H. Rème, A. M. Di Lellis, M. McCarthy, and C.W. Carlson

- (2002), Equator-S observations of He⁺ Energization by EMIC waves in the dawnside equatorial magnetosphere, *Geophys. Res. Lett.*, *29*, 1432.
- Olsen, R. C., and C. W. Norwood (1992), SPACE-GENERATED IONS, *J. Geophys. Res.*, *96*, 15951-15962.
- Otnes, R. K., and L. Enochson (1972), Digital time series analysis, *John Wiley & Sons, New York*.
- Pantellini, F. G. E., D. Burgess, and S. J. Schwartz (1994), Phase space evolution in linear instabilities (1994), *Phys. Plasmas*, *1*, 3784-3791.
- Perraut, S. (1982), Wave-particle interactions in the ULF range: GEOS-1 and -2 results, *Planet Space Sci.*, *30*, 1219.
- Perraut, S., R. Gendrin, P. Robert, A. Roux, and C. De Villedary (1978), Ultra-low frequency waves observed with magnetic and electric sensors on GEOS-1, *Space Sci. Rev.*, *22*, 347.
- Popecki, M., R. Arnoldy, M. J. Engebretson, and L. J. Cahill, Jr. (1993), High-latitude ground observations of Pc1/2 micropulsations, *J. Geophys. Res.*, *98*, 21481.
- Rankin, D. and R. Kurtz (1970), Statistical study of micropulsation polarization, *J. Geophys. Res.*, *75*, 5444.
- Sansomov, A. A., M. I. Pudovkin, S. P. Gary, and D. Hubert (2001), Anisotropic MHD model of the dayside magnetosheath downstream of the oblique bow shock, *J. Geophys. Res.*, *106*, 21689-21699.
- Sansomov, A. A., O. Alexandrova, C. Lacombe, M. Maksimovic, and S. P. Gary (2006), Proton temperature anisotropy in the magnetosheath: comparison of 3-D MHD modelling with Cluster data, submitted to *Ann. Geophys.*

- Sheeley, B. W., M. B. Moldwin, and H. K. Rassoul (2001), An empirical plasmasphere and trough density model: CRRES observations, *J. Geophys. Res.*, *106*, NO. A11, 25631.
- Sibeck, D. G., R. W. McEntire, A. T. Y. Lui, R. E. Lopez, and S. M. Krimigis (1987), Magnetic field drift shell splitting: Cause of unusual dayside particle pitch angle distributions during storms and substorms, *J. Geophys. Res.*, *92*, 13485.
- Somov, V. Boris (2000), Cosmic Plasma Physics, P. 122, Vol. 251, *Astrophysics and Space Science Library*, Kluwer Academic Publishers.
- Spasojevic, M., H. U. Frey, M. F. Thomsen, S. A. Fuselier, S. P. Gary, B. R. Sandel, and U. S. Inan (2004), The link between a detached subauroral proton arc and a plasmaspheric plume, *Geophys. Res. Lett.*, *31*, L04803, doi:10.1029/2003GL018389.
- Spence, H. E., A. M. Jorgensen, W. J. Hughes, J. F. Fennell, and J. L. Roeder(1997), Towards Inner Magnetosphere Particle and Field Models, *Adv. Space Res.*, Vol. 20, No. 3, 427-430, Published by Elsevier Ltd, Pergamon.
- Stern, D. P., and N. F. Ness (1982), Planetary Magnetospheres, *Ann. Rev. Astro. Astrophys.*, *20*, 139-161.
- Stevens, J. R., and A. L. Vampola (1978), Description of the space test program P78-2 spacecraft and payloads, Air Force Space and Missile Systems Organization (now Space Division), report SAMSO TR-78-24.
- Summers, D., and R. B. Thorne (2003), Relativistic electron pitch-angle scattering by electromagnetic ion cyclotron waves during geomagnetic storms, *J. Geophys. Res.*, *108*(A14), 1143.
- Summers, D., R. B. Thorne, and F. Xiao (1998), Relativistic theory of wave-particle

- resonant diffusion with application to electron acceleration in the magnetosphere, *J. Geophys. Res.*, *103*, 20487.
- Swanson, D. G. (2003), Plasma waves (Second edition), Institute of Physics, Series in Plasma Physics, *Taylor and Francis Publisher*.
- Thomsen, M. F., J. T. Gosling, and S. J. Bame (1985), Gyrating Ions and Large-Amplitude Monochromatic MHD Waves Upstream of the Earth's Bow Shock, *J. Geophys. Res.*, *90*, 267-273.
- Thorne, R. M., and C. F. Kennel (1971), Relativistic Electron Precipitation During Magnetic Storms Main Phase, *J. Geophys. Res.*, *76*, 4446-4453.
- Thorne, R. M., and R. B. Horne (1992), The Contribution of Ion-Cyclotron Waves to Electron Heating and SAR-Arc Excitation near the Storm-time Plasmapause, *Geophys. Res. Lett.*, *19*, 417-420.
- Thorne, R. M., and R. B. Horne (1993), Cyclotron absorption of ion-cyclotron waves at bi-ion frequency, *Geophys. Res. Lett.*, *20*, 317-320.
- Thorne, R. M., and R. B. Horne (1994), Energy transfer between energetic ring current H^+ and O^+ by electromagnetic ion cyclotron waves, *J. Geophys. Res.*, *99*, 17,275-17,282.
- Thorne, R. M., and R. B. Horne (1997), Modulation of electromagnetic ion cyclotron instability due to interaction with ring current O^+ during magnetic storms, *J. Geophys. Res.*, *102*, 14,155-14,163.
- Vacaresse, A., D. Boscher, and S. Bourdarie (1999), Modelling the high-energy proton belt, *J. Geophys. Res.*, *104*, 28,601-28,613.
- Walt, M. (1994), Introduction to Geomagnetically Trapped Radiation, in Cambridge

atmospheric and space science series, *Cambridge University Press*.

Watanabe, T. (1966), Quasi-linear theory of transverse plasma instabilities with applications to hydromagnetic emissions from the magnetosphere, *Can. J. Phys.*, *44*, 815.

Wolf, R. A. (1995), Magnetospheric configuration, in *Introduction to Space Physics*, ed. by M.G. Kivelson and C. T. Russell, *Cambridge University Press, New York*.

Yahnina, T. A., A. G. Yahnin, J. Kangas, and J. Manninen (2000), Proton precipitation related to Pc1 pulsations, *Geophys. Res. Lett.*, *27*, 3575-3578.

Young, D. T., S. Perraut, A. Roux, C. de Villedary, R. Gendrin, A. Korth, G. Kremser, and D. Jones (1981), Wave-particle interactions near Ω_{He^+} observed on GEOS 1 and 2, 1. Propagation of ion cyclotron waves in He⁺-rich plasma, *J. Geophys. Res.*, *86*, 6755.

APPENDIX

AMPTE/CCE and AMPTE/IRM: AMPTE stands for Active Magnetospheric Particle Tracer Explorers. The AMPTE program was a three-nation, three-satellite mission to study the sources, transport, and acceleration of energetic magnetospheric ions, and to investigate the interactions between clouds of cool, dense, artificially injected plasma and the hot, magnetized, rapidly flowing natural plasmas of the magnetosphere and solar wind. The three AMPTE satellites are the NASA Charge Composition Explorer (CCE), the Federal Republic of Germany's Ion Release Module (IRM), and the United Kingdom Satellite (UKS). All three were launched together on August 16, 1984 into near-equatorial elliptical orbits and contained extensive instrumentation. The CCE and IRM satellites provided the complete data set on energetic ion spectra, composition, and charge state throughout the near-earth magnetosphere.

ATS-1 and ATS-6: These two satellites were part of the Applications Technology Satellite (ATS) program. The ATS series was a set of 6 NASA satellites created to explore and test new technologies and techniques for communications and meteorological and navigation satellites. The areas investigated during the program included spin stabilization, gravity gradient stabilization, complex synchronous orbit maneuvers, a number of communications experiments, and the geostationary orbit environment. The ATS flights also

collected and transmitted meteorological data, and functioned at times as communications satellites. ATS-1 was launched on December 07, 1966, and its mission lasted 18 years. ATS-6 was launched on May 30, 1974, and its mission lasted 5 years.

Cluster: The Cluster II mission is an European Space Agency (ESA) unmanned space mission devoted to studying the Earth's magnetosphere, using four identical spacecraft flying in a tetrahedral formation. Their spacing can vary between 200 km and 18000 km. The four spacecraft give three-dimensional views of the near-Earth particle, field, and plasma environments. The four were put into a polar orbit with a perigee of 19000 km, an apogee of 119000 km, an inclination of 98.6° , and a period of 57 hours. The first two, named Salsa and Samba, were launched on July 16, 2000; the second two, named Tango and Rumba, were launched on August 20, 2000. Each satellite carries a set of 11 instruments that measure electric and magnetic fields, electrons, protons, ions, and plasma waves. The Cluster mission is currently investigating small-scale structures (in 3 D) of the Earth's plasma environment, such as those involved in the interaction between the solar wind and the magnetospheric plasma, in global magnetotail dynamics, in cross-tail currents, and in the formation and dynamics of the neutral line and of plasmoids. This mission makes it possible, for the first time, to distinguish spatial and temporal variations of magnetospheric phenomena. The mission is set to end in December 2009.

CRRES: The Combined Release and Radiation Effects Satellite (CRRES) was launched on July 25, 1990 into a geosynchronous transfer orbit, with a perigee of 350 km and an apogee of $6.3 R_E$. The satellite's orbit period was 9 hours 52 minutes. Due to its orbital

inclination of 18.2° , the satellite covered the magnetic latitude range from -30° to 30° . The local time at apogee was 08 MLT at launch and decreased at a rate of 1.3 hours per month to about 14 MLT when the spacecraft ceased its operation on October 21, 1991. The main objectives of the CRRES mission included studies of the natural radiation belt environment and its effects on a variety of microelectric components, studies of new static and dynamic models, descriptions of processes in the radiation belts, performance of active chemical release experiments in the ionosphere and magnetosphere, and low-latitude studies of ionospheric irregularities.

DE-1: DE stands for Dynamics Explorer. The DE-1 satellite was launched on August 3, 1981 into an elliptical polar orbit, with a perigee of 675 km, an apogee of 24875 km, and an inclination of 90° . Its orbit period was about 7.5 hours. The satellite carried an auroral imager and detectors designed primarily for field and particle measurements. DE-1 ceased its operation in March 1991.

***Dst* Index:** The *Dst* or disturbance storm time index is a measure of geomagnetic activity and used to assess the severity of geomagnetic storms. It is expressed in nanoteslas and is based on the average value of the horizontal component of the Earth's magnetic field obtained hourly at four near-equatorial geomagnetic observatories. Negative *Dst* values indicate that a magnetic storm is in progress; the more negative *Dst* the more intense the magnetic storm. The negative deflections in the *Dst* index are caused by the storm time ring current that flows around the Earth from east to west in the equatorial plane. The use of the *Dst* as an index of storm strength is possible because the strength of the surface

magnetic field at low latitudes is inversely proportional to the energy content of the ring current, which increases during geomagnetic storms.

GEOS-1 and GEOS-2: GEOS-1 and GEOS-2, two identical satellites of the European Space Agency (ESA), were devoted to the study of the Earth's magnetosphere. The two played the roles of reference spacecraft for the International Magnetospheric Study (IMS) and carried out correlative measurements with extensive ground-based networks in Scandinavia. The instruments on board the two were to measure DC and AC electric and magnetic fields; gradient of the magnetic field; thermal and suprathermal plasma parallel and perpendicular to the magnetic field; energy spectra, angular distribution, and composition of positive ions; and angular distribution and energy spectra of energetic electrons and protons. GEOS-1 was launched on April 20, 1977, and initially aimed to be a geosynchronous satellite, but ended up in the wrong orbit. As a result, it had a perigee of 2767 km, an apogee of 38389 km, an inclination of 26.8° , and an orbit period of 734 minutes. GEOS-2 was launched on July 14, 1978 into a truly geostationary orbit with a perigee of 36020 km, an apogee of 36061 km, an inclination of 11.8° , and a period of 1449 minutes.

GSM coordinate system: GSM stands for Geocentric Solar Magnetospheric. This coordinate system is Earth centered and has its x-axis pointing from the Earth toward the Sun. The positive z-axis is perpendicular to the x-axis and parallel to the projection of the negative moment of the Earth's magnetic field on a plane perpendicular to the x-axis. Thus the magnetic dipole axis lies within the xz plane. The y-axis is directed toward the dusk to produce a right-handed orthogonal coordinate system.

IMAGE: IMAGE stands for Imager for Magnetopause to Aurora Global Exploration. The IMAGE spacecraft was launched on March 25, 2000 into an elliptical polar orbit, with an apogee altitude of 45922 km and a perigee altitude of 1000 km. It has a nominal spin period of 2 minutes, and its spin axis is perpendicular to the orbital plane. IMAGE was the first satellite devoted to imaging the Earth's magnetosphere. IMAGE used neutral atom, ultraviolet, and radio imaging techniques to obtain the first comprehensive global images of the plasma populations in the inner magnetosphere, enabling space scientists to observe the large-scale dynamics of the magnetosphere and the interactions among its constituent plasma populations. On December 18, 2005, after 5.8 years of successful operations, IMAGE's telemetry signals were not received during a routine pass. Currently, IMAGE has not responded to commands. Although the IMAGE mission was designed as a two-year one, it has exceeded all its scientific goals and produced many stunning images of the previously invisible region of space in the inner magnetosphere.

ISEE: ISEE stands for International Sun-Earth Explorers. The ISEE program consisted of three spacecraft, ISEE-1, ISEE-2, and ISEE-3. ISEE-1 and ISEE-2 were launched on October 22, 1977 into almost coincident orbits around the Earth with periods of approximately 57 hours and inclinations of 23°, and their time separation in this orbit could be altered by maneuvering ISEE-2. These two spacecraft, separated by a variable distance and with similar instrument complements, were able to break the space-time ambiguity inevitably associated with measurements by a single spacecraft on thin boundaries that may be in motion, such as the bow shock and the magnetopause. The scientific objective of the ISEE mission was to study magnetosphere and its relation to solar activities. With

an apogee of $23 R_E$, ISEE-1 and ISEE-2 penetrated into the interplanetary medium for up to $3/4$ of their periods depending upon the time of year. The ISEE-1 and ISEE-2 spacecraft reentered the Earth's atmosphere in September 1987 after covering 1517 orbits.

***L* value:** When considering the radiation belts, it is often useful to use the *B-L* coordinate system. The *L* value of a particular point in the magnetosphere is just the distance in R_E from the Earth's center to the position at which the field line through that point crosses the equatorial plane.

OGO-5: OGO stands for Orbiting Geophysical Observatories. A series of six Orbiting Geophysical Observatories were put into orbit by NASA between 1964 and 1969. They were designed to study the Earth's atmosphere and magnetosphere, and the space between the Earth and the Moon. The fifth, OGO-5, was launched on March 4, 1968 into a highly elliptical orbit, with a perigee of 272 km and an apogee of 148228 km, and was primarily devoted to the Earth observations. Its orbital inclination was 31.1° , and the satellite took 3796 minutes to complete one orbit. The operation of OGO-5 terminated on July 14, 1972.

PHOBOS: PHOBOS was an international project that was devoted to the investigations of Mars and its satellites. The objectives of the PHOBOS mission were to conduct studies of the interplanetary environment, perform observations of the Sun, characterize the plasma environment in the Martian vicinity, and study the surface and atmosphere of Mars, and the surface composition of the Martian satellite Phobos. The project included two unmanned interplanetary probes, PHOBOS-1 and PHOBOS-2. PHOBOS-1 was launched on July 07, 1988, and PHOBOS-2 on July 12, 1988. PHOBOS-2 operated

nominally throughout its cruise and Mars orbital insertion phases, obtaining data on the Sun, interplanetary medium, Mars, and Phobos. Contact with PHOBOS-2 was lost shortly before the final phase of the mission, during which the spacecraft was to approach within 50 meters of Phobos' surface and release two landers, one a mobile hopper and the other a stationary platform. The mission of PHOBOS-2 ended on March 27, 1989, when the spacecraft signals failed to be successfully reacquired. A malfunction of the on board computer was the cause of the failure of PHOBOS-2. On board PHOBOS-2, the TAUS experiment was conducted to collect plasma data. The TAUS instrument was a mass-resolving ion spectrometer that, with its hemispherical electrostatic and electrostatic-magnetic analyzers, provided separate measurements of three-dimensional velocity distributions for protons and alphas.

Viking: Sweden's first satellite, Viking, was launched on February 22, 1986, and placed into a final 817 km-13,530 km polar orbit with an inclination of 98.6° and a period of 261.2 minutes, where it conducted scientific observations of complex plasma processes in the magnetosphere and ionosphere of the Earth. The experiments on board the satellite were designed to measure electric fields, magnetic fields, charged particles, waves, and auroral images. The satellite ceased its operations on May 12, 1987.